

# DREDGED MATERIAL RESEARCH PROGRAM



TECHNICAL REPORT D-77-12

## MATHEMATICAL MODEL OF ESTUARIAL SEDIMENT TRANSPORT

by

Ranjan Ariathurai, Robert C. MacArthur, Ray B. Krone

Department of Civil Engineering  
University of California, Davis  
Davis, Calif. 95616

October 1977

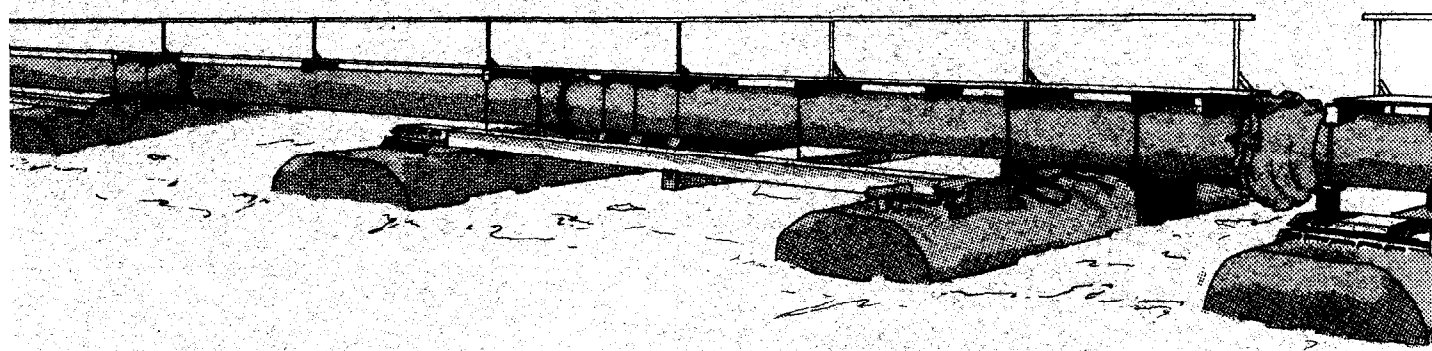
Final Report

Approved For Public Release; Distribution Unlimited

Prepared for Office, Chief of Engineers, U. S. Army  
Washington, D. C. 20314

Under Contract No. DACW39-75-C-0080  
(DMRP Work Unit No. IB05)

Monitored by Environmental Effects Laboratory  
U. S. Army Engineer Waterways Experiment Station  
P. O. Box 631, Vicksburg, Miss. 39180



**Destroy this report when no longer needed. Do not return  
it to the originator.**



DEPARTMENT OF THE ARMY  
WATERWAYS EXPERIMENT STATION, CORPS OF ENGINEERS  
P. O. BOX 631  
VICKSBURG, MISSISSIPPI 39180

IN REPLY REFER TO: WESYV

31 October 1977

SUBJECT: Transmittal of Technical Report D-77-12

TO: All Report Recipients

1. The technical report transmitted herewith represents the results of an investigation to develop a model for predicting estuarine sediment transport by simulation of erosion, transport, and deposition of suspended sediments. This study is one of the major efforts to be accomplished under Task 1B (Movements of Dredged Material) of the Corps of Engineers' Dredged Material Research Program (DMRP). Task 1B is part of the Environmental Impacts and Criteria Development Project of the DMRP.
2. An important aspect of open-water disposal of dredged material, and one that is necessary to predict and understand, is the long-term stability or the movement of the emplaced material. This is an integral part of the dredging project planning because of the environmental implications and potential for influencing the dredging and disposal requirements. The complexity of an estuarine hydrodynamic regime and the variability of cohesive sediment properties require a detailed understanding of the interactive processes effecting sediment transport. Extrapolation of data from one estuarine disposal site is not a viable mechanism for adequately predicting the final deposition of dredged material at another estuarine site with different physical and sedimentological properties. Mathematically simulating these processes will be a significant aid in prediction of the post-depositional fate of dredged material in open-water estuarine environments.
3. This report describes a two-dimensional finite element model developed during the study and the initial verification results from an actual field investigation. The model (Sediment II) is a modification to the vertical from a horizontal model (Sediment I) developed by Dr. Ranjan Ariathurai. The model using previous experimentally derived expressions for the rates and conditions of erosion and deposition allows for continuing aggregation by specifying the settling velocities of flocculation particles in each element at each time. The bed is formed of a number of sediment layers with changing physical properties as the overburden changes; a bed profile as well as a suspended sediment concentration is provided at each time step. Initial field evaluations were made with data collected from the Savannah Estuary, Georgia.

WESYV

31 October 1977

SUBJECT: Transmittal of Technical Report D-77-12

4. It is essential to understand that this model is at the forefront of the state-of-the-art in cohesive sediment transport modeling and has been subjected to very limited testing and evaluation. The model is considered to be conceptually sound, but significant additional testing and field verification are needed to establish its prediction capability and provide the proper guidance for its use. An in-house effort (Work Unit 1B10) with the Waterways Experiment Station (WES) Hydraulics Laboratory has been established to further evaluate and develop the model.

5. This model will be a useful tool in the impact evaluation of major aquatic disposal operations and in evaluating sediment transport and deposition resulting from major dredging and deepening projects. Model input requirements are rather complex and will necessitate prior planning to ensure that the comprehensive data are collected properly. It is also anticipated that this model will be used in conjunction with physical models at WES for expansion of the model's applicability in fine-grained sediment transport prediction.



JOHN L. CANNON  
Colonel, Corps of Engineers  
Commander and Director



20. ABSTRACT (Continued).

Expressions used for the rates and conditions under which erosion and deposition occur are from previous experimental studies. Continuing aggregation is accounted for by specifying the settling velocity of the flocs in each element at each time step. The bed is considered to be formed of a number of layers of sediment whose physical properties change with overburden pressure. The model provides suspended sediment concentrations and bed profile at each time step.

Numerical stability and convergence tests were conducted by comparing simulated results with analytic solutions and actual measurements. The original model, SEDIMENT I, was verified by comparison with measurements in a recirculating flume. The modified model, SEDIMENT II, developed for this project was verified by comparison with field measurements in the Savannah Estuary, Georgia.

## PREFACE

The work described in this report was performed under Contract No. DACW39-75-C-0080 entitled "Development of a Two-Dimensional Sediment Transport Model," dated January 1975, between the U.S. Army Engineer Waterways Experiment Station (WES), Vicksburg, Mississippi, and the University of California at Davis (UCD), Davis, California. The research was sponsored by the Office, Chief of Engineers (DAEN-CWO-M) under the civil works research program, Dredged Material Research Program (DMRP).

This report describes the development of a two-dimensional finite element sediment transport model (SEDIMENT II) and verification of the model by comparison with actual field data. Appendices to the report include user's manuals for the model, finite element grid generation, and contour plotting using shape functions. The model described herein is a modification of a model (SEDIMENT I) developed by Dr. Ranjan Ariathurai for his doctoral dissertation. The transport processes and sediment properties are based on a combination of previous studies that were supported by the U.S. Army Engineer District, San Francisco; the Committee on Tidal Hydraulics, U.S. Army Corps of Engineers; the National Science Foundation; and the University of California.

The principal investigator for the study was Dr. Ray B. Krone; Dr. Ranjan Ariathurai, Project Engineer, assisted by Messrs. Andrew V. Maller and Robert C. MacArthur performed the study and prepared the report. Drs. Leonard R. Herrmann and Bruce E. Larock provided technical advice. The hydrodynamic modeling for the Savannah simulation was conducted by Mr. William R. Norton, Resource Management Associates, Lafayette, California, under a subcontract. The authors of the appendices, which were edited by Dr. Ariathurai and Mr. MacArthur, are: Appendix A - Dr. Ranjan Ariathurai, Appendix B - Mr. William R. Norton, Appendix C - Dr. Leonard R. Herrmann and Mr. Andrew V. Maller, Appendix D - Dr. Ranjan Ariathurai and Mr. Andrew V. Maller, and Appendix E - Dr. Ranjan Ariathurai.

The contract was managed by Mr. Barry W. Holliday as part of the DMRP Environmental Impacts and Criteria Development Project (Dr. Robert M. Engler, Project Manager) under the general supervision of Dr. John Harrison, Chief, WES Environmental Effects Laboratory.

COL G. H. Hilt, CE, and COL J. L. Cannon, CE, were Directors of WES during the conduct of this study and preparation of this report. Mr. F. R. Brown was Technical Director.

TABLE OF CONTENTS

<u>Section</u>	<u>Page</u>
PREFACE	i
LIST OF FIGURES	vi
LIST OF TABLES	viii
CONVERSION FACTORS, CUSTOMARY TO SI UNITS OF MEASUREMENT	ix
PART I. INTRODUCTION	1
Estuarial Water and Sediment Circulation	1
Effects on Aquatic Biota	2
Previous Models	3
Purpose and Scope of This Study	4
PART II. PROPERTIES OF COHESIVE SEDIMENTS	5
Cohesion	5
Aggregation	8
Settling Velocity	10
Effect of concentration	12
Effect of salinity	14
Effect of depth	15
PART III. TRANSPORT PROCESSES	16
Erosion	16
Deposition	18
Mass Balance	20
Two-Dimensional Transport Equation	22
PART IV. NUMERICAL SOLUTION BY THE FINITE ELEMENT METHOD	25
Application of the Finite Element Method	26
Galerkin weighted residual method	26
Transformation of the diffusion terms	28
Transient Problem	31
The Bed	32
PART V. STABILITY AND CONVERGENCE OF NUMERICAL SCHEME	34
Test Problems	34
Steady state one-dimensional convection-diffusion	34
Laplace equation	35
One-dimensional transient heat conduction	36

TABLE OF CONTENTS (Continued)

<u>Section</u>	<u>Page</u>
Heat conduction with radiation	36
Transient convection-diffusion	37
Convergence Characteristics	38
Stability	41
Consistency	42
Solution to Transient Convection-Diffusion Problem	43
Summary	44
PART VI. SIMULATION OF SEDIMENT TRANSPORT IN THE SAVANNAH ESTUARY	48
Sediment Transport in the Savannah Estuary	48
Description of Field Measurements	50
Required Input for Transport Model	51
Diffusion coefficients	52
Assumed sediment and bed properties	53
Simulation Results	54
PART VII. CONCLUSIONS AND RECOMMENDATIONS	66
Conclusions	66
General	66
Specific	66
Recommendations	67
REFERENCES	68
APPENDIX A: FINITE ELEMENT DERIVATIONS	A-1
The Element and Shape Functions	A-1
Derivatives of Functions	A-3
Coefficient Matrices	A-5
Contour Integral of Flux	A-7
Computation of Net Mass Flux to the Bed	A-9
APPENDIX B: FLOW SIMULATION	B-1
Technical Approach	B-1
Momentum equations	B-2
Continuity equation	B-2
Convection-diffusion equation for density	B-2

TABLE OF CONTENTS (Continued)

<u>Section</u>	<u>Page</u>
Model Application	B-3
Introduction	B-3
Physical description of the Savannah Estuary	B-4
Water balance	B-7
Model calibration	B-12
Model results	B-12
Discussion	B-12
APPENDIX C: FINITE ELEMENT GRID GENERATOR	C-1
Theory	C-1
Generalized equations	C-1
Laplacian scheme	C-3
Isoparametric scheme	C-5
Illustrative examples	C-7
Data Preparation	C-7
User's Manual	C-18
Example Problems	C-21
Example problem #1	C-21
Example problem #2	C-24
APPENDIX D: CONTOUR PLOTTING USING SHAPE FUNCTIONS	D-1
Interpolating Using Shape Functions	D-1
Data Preparation	D-4
User's Manual	D-7
General Comments	D-11
APPENDIX E: USER'S MANUAL FOR SEDIMENT II	E-1
Data Preparation	E-1
Input	E-1
User's Manual for Sediment II (Vertical Model)	E-3
User's Manual for Sediment II (Horizontal Model)	E-6
APPENDIX F: NOTATION	F-1

## LIST OF FIGURES

<u>No.</u>		<u>Page</u>
5.1	Order of Convergence of Solution to the 1-D Convection Diffusion Equation	39
5.2	Order of Convergence of Solution to Laplace Equation	39
5.3	Order of Convergence of Solution to Heat Conduction Equation	40
5.4	Order of Convergence of Solution to Heat Conduction Problem With Radiation	40
5.5	Spatial Convergence for $\Delta t = 0.05$	43
5.6	Influence of Peclet Number on Accuracy	45
5.7	Effect of Reducing Time Step Size, $N_{Pe} = 1000$	45
5.8	Effect of Reducing Time Step Size, $N_{Pe} = 10$	46
5.9	Effect of Changing $\theta$ Value, $N_{Pe} = 1000$	46
6.1	Locations of Water Measurement and Shoal Sampling Stations	49
6.2	Transport and Shoaling Processes in the Study Area	50
6.3	Half-Hourly Suspended Sediment Concentrations at Sta. 125+500, During Spring Tide	55
6.4	Suspended Sediment Concentrations at Station 125 + 500, Spring Tide	60
6.5	Simulated Average Shoal Thickness, Spring Tide	63
A.1	Element With Local Coordinate System	A-1
B.1	Locations of Water Measurement and Shoal Sampling Stations	B-5
B.2	Midtide Cross Sections at the Sampling Stations	B-6
B.3	Finite Element Network Used for Flow Simulation in the Savannah Estuary Between Stations 109+667 and 130+500	B-8
B.4	Comparison Between Simulated and Observed Velocities at Station 125 + 500 in the Savannah Estuary	B-14
C.1	Neighborhood of Node "i" Non-Rectangular Grid	C-2
C.2	Number of Iterations Required for Convergence as a Function of w	C-4
C.3	Neighborhood of Node "i"	C-4
C.4	Isoparametric Transformation of Neighborhood of Node "i"	C-6
C.5	Example to Illustrate Effect of Boundary Node Spacing	C-8

LIST OF FIGURES (Continued)

<u>No.</u>		<u>Page</u>
C.6	Example to Illustrate Effect of Boundary Convergence	C-9
C.7	Sample Grid	C-10
C.8	Node Points Lying on a Straight Line	C-13
C.9a	Grid Sketch, Example Problem #1, $N_{\max} = 16$	C-22
C.9b	Grid Sketch, Example Problem #1, $N_{\max} = 22$	C-22
C.10	Data Input, Example Problem #1	C-23
C.11	Plotted Output for the Example Problem #1	C-25
C.12	Example Problem #2, Grid Sketch	C-26
C.13	Data Input, Example Problem #2	C-27
C.14	Plotted Output for the Example Problem #2	C-29
D.1	Approximation to Function Within the Element	D-3
D.2	Element With Contours Using Shape Function and Linear Approximation	D-3
D.3	Ambiguous Cases	D-4
D.4	Example Contour Plot of Depth Soundings	D-5
D.5	Example Contour Plot of Potential Flow	D-6

LIST OF TABLES

<u>No.</u>		<u>Page</u>
2.1	Critical Cation Concentrations and Corresponding Salinity for Potential Aggregation in Seawater (Ref. 1)	7
2.2	Properties of Sediment Aggregates	11
2.3	Settling Velocity Parameters for Sea Water	14
5.1	Convergence Characteristics of Solution	41
6.1	Aggregate Settling Velocities	51
6.2	Average Values of Vertical Eddy Diffusivity Used for Spring Tide Simulation	53
6.3	Bed Layer Properties	54
A.1	Quadratic Shape Functions	A-2
A.2	Derivatives of Shape Functions	A-4
B.1	Net Flows and Rate of Change of Volume Between Stations 109+668 and 130+500 in the Savannah Estuary, Sept. 24-25, 1968	B-9
B.2	Velocity Correction Factors for an Exact Water Balance, Savannah Estuary, Sept. 24-25, 1968	B-11

CONVERSION FACTORS, CUSTOMARY TO SI UNITS OF MEASUREMENT

The mathematical model described in this report works in SI units. However, derivations and measurements are presented in the text in customary units, which can be converted to SI units as follows:

<u>Multiply</u>	<u>By</u>	<u>To Obtain</u>
inch	2.540* - 02	meter
foot	3.048* - 01	meter
micron	1.000* - 06	meter
angstrom	1.000* - 10	meter
foot/second	3.048* - 01	meter/second
centimeter/second	1.000* - 02	meter/second
pound/cubic foot	1.602* + 01	kilogram/cubic meter
gram/cubic centimeter	1.000* + 03	kilogram/cubic meter
gram/liter	1.000* + 00	kilogram/cubic meter
cubic foot/second	2.832* - 02	cubic meter/second
square foot/second	9.290* - 02	square meter/second
dyne	1.000* - 05	newton
dyne/square centimeter	1.000* - 01	newton/square meter

PART I. INTRODUCTION

Estuarial Water and Sediment Circulation

1. The design and maintenance of navigation facilities and the management of estuarial water quality are made difficult by the complexity of estuarial water and sediment circulations. Effects of deepening navigable waterways, of changing shoreline configurations, or of discharging dredged material in open waters need to be evaluated or predicted for maintenance cost and for water-quality management considerations. An accurate predictive model of estuarial sediment transport would be very useful for planning and designing optimum development of estuaries.

2. Estuaries are zones of transition from unidirectional, time-varying, freshwater flows of land drainage to a tidal, saline ocean. Water movements throughout an estuary are affected by any change in either the freshwater inflows or the ocean tide, and are otherwise determined by the configuration of the estuary and by winds. The effects of various configurations include resonances, which produce standing waves that affect the tidal range, and friction or narrow openings, which delay the progress of tidal change upstream and affect the character of freshwater and saltwater mixing. Winds contribute to vertical circulations and generate waves that suspend sediment deposited in shallow bays. The differences in freshwater and saltwater densities cause the ocean water to move landward near the bottom and to mix upward with the fresher water near the water surface.

3. Sediment circulations are even more complex than that of estuarial waters. Eroded soil material enters an estuary with freshwater drainage, by wave erosion of shores, or by aeolian transport. In areas having seasonal precipitation, the bulk of the sediment can enter during a few winter or spring months, and a portion may pass directly to the ocean with high river flows. The eroded material typically

contains large amounts of clay and silt materials which, in the increasingly saline waters and hydraulic conditions of the estuary, aggregate and settle in shallow bays as well as in deepened waterways. Onshore breezes occur daily in coastal regions and keep the material in shallow areas in suspension while slow tidal currents circulate the suspended material. A portion may be carried with ebb tide to the ocean and during calm hours the material settles again. Continued settling may also occur in deepened channels and harbor areas where currents are insufficient to resuspend the material.

#### Effects on Aquatic Biota

4. The effects of sediments on water quality for aquatic biota include limitation of the penetration of sunlight and the absorption of toxic compounds from solution. The concentrations of nutrients for algae in some estuaries are often sufficient to cause excessive algae blooms. The rate of multiplication of algae in such estuarial waters is limited by a reduced light supply resulting from high turbidity caused by suspended sediment particles. Heavy metals and pesticides are found sorbed on sediment materials with equilibrium between dissolved and sorbed materials frequently favoring the sorbed phase. The sediment materials appear to be providing a large assimilative capacity for toxic compounds discharged to the waters in wastes. Storage of river waters upstream and their diversion for agriculture and for urban uses will sharply reduce sediment inflows as water resources become more precious. It will be necessary to predict the effects of reduced sediment inflows to ascertain the minimum waste management needed to achieve desirable water quality.

5. Due to the low flow velocities prevalent in most rivers where they enter estuaries, a large portion of the total sediment load is usually composed of suspended silt and clay mineral particles. These fine sediments form interparticle bonds when they become mutually attractive and can then form aggregates under suitable conditions. Their mode of transport and the beds they form are very

different from that of noncohesive sands and gravels. Modeling sediment circulation requires the application of mathematical descriptions of the processes of aggregation, deposition, and resuspension to the transport model. Such descriptions are available from laboratory and field studies of estuarial sediments.

### Previous Models

6. Although studies have been conducted on the vertical distribution of suspended material in relatively simple flow fields, e.g., Dobbins (7), Sayre (24), Jobson and Sayre (10), the mathematical model developed by Odd and Owen (18) was the first to include erosion, transport, and deposition. The latter model was one-dimensional and considered the flow divided into two unequal horizontal layers. The model was designed for the Thames estuary, which was assumed rectangular in section with breadth varying exponentially along the length. Since then Christodoulou, Leimkuhler, and Ippen (6) developed a mathematical model for dispersion in coastal waters. They assumed constant flow depth, a simple function for the flow, and did not characterize scour or aggregation. The models described worked well on the specific problems they were applied to, and have been responsible for the development of the art to its present state.

7. The finite element model SEDIMENT I (1,2) was developed with the aim of general application to suspended phase transport in a time-varying two-dimensional flow field. It includes expressions for erosion and deposition and can account for aggregation. The model is applicable to the transport of any conservative material - or of non-conservative materials if the reaction rates are known. The vertical and axial dimensions with the breadth averaged, or the two horizontal dimensions with the depth averaged, may be used in the model. The time-varying two-dimensional flow field, obtained from field measurements or a hydraulic model, must be provided as input to SEDIMENT I to simulate the suspended sediment concentrations and bed profile as they vary with time. The model described herein, SEDIMENT

II, is a further developed version of SEDIMENT I.

### Purpose and Scope of This Study

8. The need for descriptions of estuarial sediment movements and deposition, and for a means of predicting such movement under changed conditions, has been felt keenly by people engaged in design of channels and harbors, those concerned with management of dredged material, and agencies responsible for the maintenance and enhancement of the quality of estuary waters. The study described in this report is the latest in a sequence that includes studies of sediment material properties including those of suspended aggregates, studies of individual transport processes including deposition and erosion in flows and under waves, and field studies of sediment material circulation in estuaries. This effort combines the information from the previous studies in a formal, quantitative way to provide a means for describing existing or changed cohesive particle concentrations throughout a water body as they change with time. The model also describes rates of deposition or bed erosion.

## PART II. PROPERTIES OF COHESIVE SEDIMENTS

9. The properties of cohesive sediments relevant to the transport process have been presented in different degrees of detail in references 1, 2, 3, 12, 13, and 14. These descriptions are summarized in this part since they are essential to an understanding of the model described in this report.

### Cohesion

10. Cohesive sediments are comprised largely of colloidal clay particles and fine silts which possess colloidal properties to a lesser degree. The remainder includes algae, organic matter from contiguous drainage areas, and waste materials. Clay minerals are hydrated aluminum silicates in a layer lattice crystal structure which typically gives the particles platy shapes. They are divided into three main groups according to crystal structure, namely: kaolinite, illite, and montmorillonite. The positively charged elements (cations) of the crystals occupy interior layers, and the electro-negative hydroxyl and oxygen atoms are located on the platy surfaces. Positive charges are exposed at the crystal edges. The cations in the crystal lattice may be isomorphously substituted by other ions, generally of lower valence, producing a net charge deficiency which makes the surface negative charge even greater.

11. This surface charge distribution causes clay particles suspended in water to adsorb water and to attract dissolved ions that form a diffuse layer of ions. These sorbed ions may be exchanged for others of like charge when the chemical composition of the surrounding medium is changed. The capacity to exchange cations, cation exchange capacity (CEC), is usually expressed as the milli-equivalents (me) of exchangeable cations held by 100 g of dry mineral. The CEC is an effective measure of the activity of a clay, i.e., the extent to which it possesses colloidal properties, and depends on the surface charge density and the surface area per unit weight of dry mineral. Values

of CEC of common clay minerals are typically montmorillonite, 50 to 150 me/100 g; illite, 10 to 40 me/100 g; kaolinite, 1 to 15 me/100 g.

12. The principal forces between clay particles can be broadly classified into coulombic and van der Waal's. The former are due to the electric charges on the particles and the distribution of sorbed ions surrounding the suspended particle and may be attractive or repulsive depending on the type and amount of ions in solution. Van der Waal's forces do not depend on the surface charge, are of a much shorter range, and are always attractive. The net interparticle attraction depends on:

- a. The surface charge density, which is a property of the clay mineral.
- b. The salt concentration of the surrounding water, attraction increasing with increasing concentration.
- c. The valency of the cations in solution, attraction increasing markedly with increasing valency.
- d. The temperature, attraction decreasing with increasing temperature.
- e. The separation, attraction decreasing very rapidly with increasing distance.
- f. The pH of the surrounding water.
- g. The kind of anions in solution.

13. The net interparticle force determines the potential for particles to form aggregates upon collision. It can be seen from the above list of variables that particles in a suspension can be made mutually repulsive or cohesive by changing the composition and concentration of sorbed ions. These ions tend to seek equilibrium concentrations with those in the surrounding solution. It is possible to predict, from the concentrations of dissolved cations, when the various clay minerals become cohesive. Application of the Gapon equation to the exchange reaction of the commonest ions in natural waters, sodium, calcium, and magnesium, results in an equilibrium constant called the sodium adsorption ratio (SAR) which is given by

$$\text{SAR} = \frac{[\text{Na}^+]}{\sqrt{\frac{1}{2}([\text{Ca}^{++}] + [\text{Mg}^{++}])}} \quad (2.1)$$

where the brackets indicate concentrations in me/l.

14. The SAR of the bulk solution is easily determined and is proportional to the ratio of exchangeable sodium to calcium plus magnesium ions found in the diffuse layer of sorbed ions near the mineral surfaces (11). Together the CEC of the clay, the total salt concentration, SAR, and pH of the suspending water predominate in determining cohesion. The critical concentrations and corresponding salinities of diluted seawater at which kaolinite, illite, and montmorillonite become cohesive are reported in Ariathurai (1) and reproduced in Table 2.1.

Table 2.1

Critical Cation Concentrations and Corresponding Salinity  
for Potential Aggregation in Seawater (Ref. 1)

<u>Clay Type</u>	<u>Total Cation Concentration me/l</u>	<u>Salinity g/l</u>
Kaolinite	1.0	0.6
Illite	2.0	1.1
Montmorillonite	4.3	2.4

15. These values were calculated using SAR and concentration data obtained from sedimentation tests that were conducted at various electrolyte chemical compositions (11) to obtain boundary curves between aggregated and dispersed states. The range of salinities presented in Table 2.1 (0.6 g/l to 2.4 g/l) compares well with the 1 to 3 g/l range in which Krone (13) observed an increase in the median settling velocity.

## Aggregation

16. When suspended clay particles are mutually cohesive and are subjected to repeated collision, they form aggregates. These aggregates often contain millions of clay particles. Since the aggregates are of a much larger size than the primary particles they are composed of, they settle at velocities orders of magnitude higher than that of the primary particles. Aggregation is therefore a factor of major importance in cohesive sediment transport.

17. There are three principal mechanisms of interparticle collision in suspension. The first is due to Brownian motion which is produced by the thermal motions of the molecules of the suspending medium. The frequency of collision  $I$ , on one particle by others, was described by Whytlaw-Gray and others (30) as

$$I = \frac{4kTn}{3\mu} \quad (2.2)$$

where\*

$k$  = Boltzmann's constant

$T$  = absolute temperature

$n$  = number concentration of suspended particles

$\mu$  = viscosity of the water.

Under typical conditions where the water temperature is 20°C,  $I = 5 \times 10^{-12} n$  collisions per second. Aggregation rates by this mechanism are too slow to be significant in estuaries unless the weight concentration is above approximately 10 g/l. Aggregates formed by this mechanism have a lacelike structure, are weak, and easily dispersed by shearing or are easily crushed in a deposit.

18. The second mechanism of interparticle collision is that due to internal shearing produced by the local velocity gradients in the fluid. Collision will occur if the paths of the particle centers in

---

\* For convenience, symbols and unusual abbreviations are listed and defined in the notation (Appendix F).

the velocity gradient are displaced less than the sum of their radii, which is called the collision radius,  $R_{ij}$ , between i-size and j-size particles. The frequency of collision J on a suspended spherical particle was derived by Smoluchowski (26) as

$$J = \frac{4}{3} n_i R_{ij}^3 G \quad (2.3)$$

where G is the local velocity gradient. Aggregates produced by this mechanism are relatively dense and strong because only those bonds that are strong enough to resist the local fluid stresses remain. The product,  $n_i R_{ij}^3$ , is large when aggregates are mixed with a large number of dispersed particles, as is the case in an estuarial mixing region.

19. The third mechanism of interparticle collision results from differential settling velocities of different size particles. The frequency of collision H due to this mechanism is described by Fuchs (8) as

$$H = \pi E R_{ij}^2 V n \quad (2.4)$$

where

E = a capture coefficient

V = relative velocity between particles.

This produces weak aggregates and contributes to the observed rapid clarification of estuarial waters at slack.

20. All three of these mechanisms operate in an estuary. Differential settling is probably important only when aggregation is already far advanced and the currents are relatively small as at times of slack water. In most estuaries internal shearing is by far the most important collision mechanism.

21. Krone (14) described a system of aggregate structures as follows:

Aggregates formed by adding primary mineral particles one at a time to form a uniform aggregation are designated a

primary particle aggregate or a zero-order aggregate. When primary particle aggregates collide with each other and aggregate, first-order aggregates are formed. First-order aggregates will include interaggregate pores in addition to the interparticle pores of the zero-order aggregate and are less dense and weaker than zero-order aggregates. First-order aggregates can collide with each other to form second-order aggregates, and so on. The densities and shear strengths of progressively higher order aggregates so formed will decrease progressively. If the stress on an aggregate already formed exceeds its apparent shear strength, the aggregate will be rendered until a lower order aggregate having the necessary shear strength remains. A freshly deposited cohesive bed surface is one order of aggregation greater than that of the depositing aggregates, so that it is weaker. Aggregates can be rendered to successively lower order when exposed to increasing shearing rates and then reform when appropriate hydraulic conditions occur. The structure, density, and shear strength are sensitive to the previous and prevailing hydraulic conditions.

22. Densities and shear strengths for a number of estuarial sediments obtained from concentric cylinder viscometer tests (13) are presented in Table 2.2.

### Settling Velocity

23. An important sediment property in the modeling of cohesive sediment transport is the settling velocity. For particles smaller than about 10 microns\* in diameter, Brownian motion is significant compared with gravitational motion (15). The downward flux of these particles in a standing cylinder settling test is the net result of gravitational motion and thermal diffusion. When the settling particles are cohesive they aggregate on collision forming larger aggregates with higher or lower settling velocities. This process further complicates the settling velocity determination.

24. In a steady state flow with a logarithmic velocity profile, the concentration  $C_z$  of uniform suspended particles at elevation  $z$

---

\* A table of factors for converting customary units to SI units is presented on page ix.

Table 2.2

Properties of Sediment Aggregates

<u>Sediment Sample</u>	<u>Order of Aggregation</u>	<u>CEC me/100 g</u>	<u>Density g/cu cm</u>	<u>Shear Strength dynes/sq cm</u>
Wilmington District	0	32	1.250	21
	1		1.132	9.4
	2		1.093	2.6
	3		1.074	1.2
Brunswick Harbor	0	38	1.164	34
	1		1.090	4.1
	2		1.067	1.2
	3		1.056	0.62
Gulfport Channel	0	49	1.205	46
	1		1.106	6.9
	2		1.078	4.7
	3		1.065	1.8
San Francisco Bay	0	34	1.269	22
	1		1.179	3.9
	2		1.167	1.4
	3		1.113	1.4
	4		1.098	0.82
	5		1.087	0.36
	6		1.079	0.20
White River (salt)	0	60	1.212	49
	1		1.109	6.8
	2		1.079	4.7
	3		1.065	1.9

above the bed can be shown to be

$$\frac{C_z}{C_a} = \left( \frac{a}{d-a} \right)^\zeta \left( \frac{d-z}{a} \right)^\zeta \quad (2.5)$$

where

a = some reference elevation at which the concentration  $C_a$  is known

d = depth of flow

$\zeta = V_s/kU_*$

$V_s$  = settling velocity

k = von Karman's constant

$U_*$  = shear velocity.

By measuring the concentrations and currents at a number of points in the vertical, it would be possible to use equation 2.5 to compute the settling velocity. If it can be assumed that the suspended aggregates have reached a terminal size because of the uniform flow and low suspended solids concentration, and if the velocity profile is logarithmic, the settling velocities so obtained may then be used to predict settling rates when the flow conditions are changed as long as the change is not drastic. Such conditions can be expected in only a limited number of cases.

25. The results of extensive studies (13,17,18,20) on the settling velocities of cohesive sediments in still water can be summarized as follows.

#### Effect of concentration

26. Three ranges of concentration have been identified in which the settling velocity of aggregates varies in different ways. The first range is for suspended sediment concentrations from 0 to some  $C_1$  g/l. In this range the number concentration is so low that there is very little mutual interference between the particles and further collisions are infrequent. The settling velocity can be assumed a constant for the particular hydraulic conditions. When terminal aggregate size has been reached, the settling velocity in this range was found to follow the relationship:

$$V_s = KC^m \quad 0 \leq C \leq C_1 \quad (2.6)$$

where

K = empirical constant

C = suspended sediment concentration

m = empirical exponent.

27. In the second range,  $C_1 \leq C \leq C_2$  g/l, there is significant mutual interference between flows around the settling aggregates - "hindered settling" is said to occur. A sharp demarcation of the sediment surface appears and settling at a uniform velocity begins. This hindered settling velocity of estuarial sediments was shown by Pierce and Williams (22) and of activated sludges by McGauhey and Krone (16) to be described by the Richardson-Zaki relation

$$V_s = V_p (1 - \phi)^a \quad (2.7)$$

where

$V_p$  = settling velocity of individual aggregates in a dilute suspension

$\phi$  = volume concentration of suspended aggregates

a = constant that was determined by Richardson and Zaki to be 4.65 (a = 5 is often assumed).

Pierce and Williams applied equation 2.7 by considering  $\phi = bC$ , where C is the weight concentration and plotting  $V_s^{1/5}$  vs C. An unchanged aggregate structure over the range of concentrations studied was assumed. The points should fit a straight line, and values of  $V_p$  and C can be calculated from the intercept and slope of the line, although these have not been verified by other measurements.

28. Settling particles accumulate on the bed or bottom of a settling cylinder at concentrations above  $C_2$  and form a steadily deepening deposit. If the settling particles were sand or silt, the structure of the deposit would not be altered significantly as overburden increases, but particles that are aggregates of cohesive mineral or organic particles crush linearly as the overburden develops

until the larger void spaces are collapsed, then crush a smaller amount with increasing overburden as smaller pores collapse.

29. The time rate of consolidation is determined by the rate at which expelled pore water can work its way upward through the deposit. The most useful description of the consolidation of a deposit is the empirical relation proposed by Bosworth (4), i.e.,

$$\frac{h}{h_{\infty}} - 1 = \frac{t'}{t} \quad (2.8)$$

where

$h$  = the measured height of the deposit surface above the rigid bottom

$h_{\infty}$  = the final consolidated height

$t'$  = a characteristic time

$t$  = the time of consolidation at which  $h$  is measured.

30. The values of the critical concentrations  $C_1$  and  $C_2$  and the exponent  $m$  in equation 2.6, obtained by various investigators, are summarized in Table 2.3.

Table 2.3

Settling Velocity Parameters for Sea Water

<u>Investigator (Reference)</u>	<u><math>C_1</math> g/l</u>	<u><math>C_2</math> g/l</u>	<u><math>m</math></u>
Krone (13)	0.3	10	4/3
Odd and Owen (18)	0.05	15	1 to 2
Owen (20)	-	9	~1
Migniot (17)	-	10-20	~1

Effect of salinity

31. The effect of increasing total salt concentration and varying the SAR has been discussed in Part II. However, the effect of increasing the salinity beyond the concentration required to make

the particles mutually attractive is not understood clearly. For sediment concentrations less than 1 g/l, Krone (13) observed no significant change in the settling velocity above a salinity of about 5 g/l. Owen (20) conducted a number of settling tests at various salinities and observed that the settling velocity increases with salinity up to a value which was between 28 and 43 g/l, depending on the concentration of sediments. After this value, there was a decrease in the settling velocity with increasing salinity. Evidently, the salinity affects the density of the settling aggregate.

#### Effect of depth

32. The depth through which settling occurs affects the settling velocity only if aggregation is continuing. It would then be expected that the greater the depth through which particles settle, the greater would their settling velocities become as aggregation continues. However, it has been observed (20) that the settling velocity actually decreased in the first meter or so and then increased to a terminal value at a depth of about 2 m.

## PART III. TRANSPORT PROCESSES

33. Erosion, convection and diffusion, and deposition constitute the transport processes. Cohesive sediments move entirely as suspended load and form a cohesive bed when they are deposited. Descriptions of estuarial sediment transport processes have only been obtained during recent years. This section presents a distillation of these descriptions obtained during a succession of laboratory and field studies.

### Erosion

34. The electro-chemical bond between cohesive particles must first be broken before detachment and transport of such materials can take place. The factors that determine the strength of this electro-chemical bond have been discussed in the previous chapter with respect to suspended sediments. All of those factors affect the erodibility of a cohesive bed as well. Clay minerals, particularly montmorillonite, form gels when they settle on the bed and are left undisturbed. If the gel is mechanically sheared, it becomes a slurry, then the gel gradually redevelops. This behavior is typical of colloids and is a property termed thixotropy. Kaolinite and illite exhibit this property to a much lower degree unless aided by the presence of organic matter.

35. Most natural cohesive beds are hydraulically smooth in the range of flow conditions encountered in practice. Hence, the hydraulic shear stress at the bed is an accurate measure of the entrainment force. Since the interparticle bonds must be broken before entrainment can take place, it would be expected that a critical shear stress must be exceeded before surface erosion of a bed can begin. Extensive laboratory experiments (11,12,13,17,20) have shown this to be true. The critical shear stress of a cohesive bed is defined as the intercept on the shear stress axis on a plot of erosion rate vs. bed shear stress.

36. The resistance of a cohesive bed to erosion by flowing water depends on the following:

- a. The types of clay minerals that constitute the bed.
- b. Structure of the bed, which in turn depends on the environment in which the aggregates that formed the bed were deposited, elapsed time, temperature, and the rate of gel formation.
- c. The chemical compositions of the pore and eroding fluids.
- d. Stress history, i.e., the maximum overburden pressure the bed had experienced and the elapsed time at various stress levels.
- e. Presence of organic matter and its state of oxidation.

37. The greater the overburden pressure and elapsed time, the greater the resistance to erosion. Krone (12) presents the variation in critical shear stress with depth of deposit obtained from experiments in a recirculating flume. It was observed that the aggregates that settle out are crushed by those settling above, resulting in an increased number of interparticle bonds causing an increase in resistance to erosion. This increase in resistance to fluid shear stress occurred in layers of about 1-inch thickness until the overburden was sufficient to crush the aggregates to primary particles. Beyond this depth the bed resists erosion as any saturated cohesive soil deposit, the erodibility of which has been studied by investigators such as Kandiah (11).

38. At bed shear stress just above critical value, erosion occurs particle by particle; this process is called surface erosion. At higher levels of stress, however, the bulk shear strength of the bed may be exceeded. The portion of a bed in such a state is susceptible to mass erosion, i.e., as the bed shear exceeds the critical shear stress of that portion of the bed, it fails totally and is instantly suspended.

39. To model the transport process, it is necessary to know the critical shear stress of each stratum of the bed and also the erosion rate if the erosive mechanism is surface erosion. At present, laboratory measurements must be made to obtain these parameters. The critical shear stress for scour and rates of erosion may be measured

in a flume for beds of relatively low strength. Stronger beds may be tested in the rotating cylinder apparatus by the method described by Sargunam et al. (23), although this method is not suitable for thin layers.

40. The erosion rate for particle erosion is given by Partheniades (21) as

$$(dm/dt)_e = M (\tau_b/\tau_{ce} - 1) \quad (3.1)$$

$$\tau_b > \tau_{ce}$$

where

- $(dm/dt)_e$  = mass rate of erosion per unit area
- $\tau_b$  = bed shear stress
- $\tau_{ce}$  = critical shear stress for erosion
- $M$  = erodibility constant.

If  $d$  is the local depth of flow,

$$(dC/dt)_e = (dm/dt)_e/d \quad (3.2)$$

is the rate of change of concentration of the suspension due to erosion of the bed.

41. When mass erosion occurs

$$(dC/dt)_e = (\Delta m/\Delta t)/d \quad (3.3)$$

where

- $\Delta m$  = mass eroded per unit bed area
- $\Delta t$  = a characteristic time in which erosion occurs.

#### Deposition

42. When the shear stress on the bed is not sufficient to resuspend particles that contact and bond with the bed, deposition occurs. The shear stress at which there is an incipient net rate of

deposition is termed the critical shear stress for deposition. This value may be the same or less than the critical shear stress for erosion, depending on the history of the bed surface.

43. As a result of extensive laboratory studies, Krone (12) described the depositional behavior of cohesive sediments in the following manner.

44. The probability  $P$  of particles sticking to the bed increases linearly with a decrease in the bed shear and is given by

$$P = 1 - \tau_b / \tau_{cd} \quad (3.4)$$

where  $\tau_{cd}$  = critical shear stress for deposition. In the absence of continuing aggregation of the transported aggregates, the rate of loss from suspension is

$$\frac{dC}{dt} \Big|_d = - \frac{PV_s C}{d} \quad (3.5)$$

where  $d$  = average depth through which the particles settle.

Integration of equation 3.5 leads to

$$\log \frac{C}{C_o} = - K_o t \quad (3.6)$$

where  $K_o = V_s P / (2.3 d)$ . This relation was verified in a recirculating flume where the aggregation rate was found to be negligibly slow at concentrations below 300 mg/l so long as unusual eddy-producing disturbances to the flow were avoided.

45. At higher concentrations, or under flow conditions where collisions of suspended particles are frequent relative to the time of observation, a relation that includes the effect of continuing aggregation was demonstrated that simplifies to

$$\log \frac{C}{C_o} = - K_2 \log t \quad (3.7)$$

where

$K_2$  = empirical constant  
 $C_0$  = initial concentration  
 $t$  = elapsed time.

The coefficient  $K_2$  equals  $K_3 V_s P/d$ , where  $K_3$  includes properties of the aggregating aggregate. For practical purposes,  $K_3 V_s$  can be combined to give an empirical constant.

### Mass Balance

46. Since the sediment-water system is a binary solid-liquid mixture the mass balance for sediment must be developed with care. In a diffusing mixture the various species move at different velocities. In addition, the negatively buoyant sediment particles will settle with respect to the suspending water, so that the vertical convective velocity of the water differs from that of the sediment by the settling velocity  $V_s$ .

47. The local mass averaged velocity  $\vec{V}$  for the mixture is defined as

$$\vec{V} = (C_w \vec{V}_1 + C \vec{V}_2) / (C_w + C) \quad (3.8)$$

where

$\vec{V}_1$  = velocity of water  
 $\vec{V}_2$  = velocity of sediment  
 $C_w$  = mass of water/volume of suspension  
 $C$  = mass of sediment/volume of solution.

The density of the suspension  $\rho$  equals  $(C + C_w)$ .

48. Choosing a fixed Cartesian system of axes with the x-axis along the longitudinal, pointing downstream; the y-axis vertical, opposite to the direction of gravity; and the z-axis from left to right, the convective velocity of water  $\vec{V}_1$ , and of sediment  $\vec{V}_2$  may be written as

$$\vec{V}_1 = u\vec{i} + v\vec{j} + w\vec{k}$$

$$\vec{V}_2 = u\vec{i} + (v + v_s)\vec{j} + w\vec{k} \quad (3.9)$$

where  $u$ ,  $v$ , and  $w$  are the components of the fluid velocity.

49. Here the water and sediment are assumed to convect in the two horizontal directions,  $x$  and  $z$ , with identical velocities. The settling velocity  $v_s$  will be negative except for positively buoyant particles.

50. The law of conservation of mass applied to the sediment yields

$$\frac{\partial C}{\partial t} + \nabla \cdot C\vec{V}_2 + \nabla \cdot \vec{f} = s \quad (3.10)$$

where

$\vec{f}$  = diffusive flux

$s$  = source/sink term to account for addition or removal of sediment.

51. By Fick's law

$$\vec{f} = -\rho M \nabla(C/\rho) \quad (3.11)$$

where  $M$  is the molecular diffusivity. The equation for continuity for the mixture is

$$\frac{\partial \rho}{\partial t} + \nabla \cdot \rho\vec{V} = 0 \quad (3.12)$$

52. For suspensions with relatively low concentrations of sediment,  $\rho$  may be assumed constant. Then equation 3.10 can be written as

$$\frac{\partial C}{\partial t} + \nabla \cdot C\vec{V}_2 = \nabla \cdot M \nabla C + s \quad (3.13)$$

53. For turbulent flows with temporal velocity fluctuations such as  $u'$ , and concentration fluctuations  $c'$ , a Fickian analogy is used, so that

$$\overline{u'c'} = - e_x \frac{\partial \bar{C}}{\partial x} \quad \text{etc.} \quad (3.14)$$

Here  $e_x$  = turbulent diffusion coefficient, and the overbars signify time averaging.

54. Then

$$\frac{\partial C}{\partial t} + \nabla \cdot C \vec{V}_2 = \nabla \cdot E \nabla C + S \quad (3.15)$$

where  $E = e + m$  is the diffusion tensor, in which the off-diagonal terms are neglected. The above equation is applicable to the convection and diffusion of sediment in a three-dimensional flow field. The concentration or its normal derivative must be specified everywhere on the boundary of the domain as a boundary condition.

#### Two-Dimensional Transport Equation

55. If it is necessary to use the two-dimensional form of the convection-diffusion equation (3.15), as is the case in this study, the mass balance must either be obtained by macroscopic consideration or by integration.

56. Usually there will exist both velocity and concentration profiles in the direction that is being averaged. For example, when depth averaging (y-direction), the lateral velocity components  $u$  and  $w$  and the point concentration  $C$  will vary with depth. This gives rise to dispersion terms.

57. The governing equation (3.15) can be integrated over the depth  $d$ , with  $b(x,z)$  being the elevation of the bed and  $h(x,z,t)$  that of the free surface, so that  $d = h - b$ . The velocity components and concentration along  $y$  are expressed as a mean value  $\bar{c}$ , for example, and a deviation  $c''$ , i.e.,

$$C = \bar{c} + c'' \quad \text{etc.} \quad (3.16)$$

Then

$\int_b^h c'' dy = \frac{\partial c''}{\partial x} = 0$  etc., in exactly the same fashion as in temporal averaging.

Also:

$$\bar{c} = \frac{1}{d} \int_b^h c dy \quad (3.17)$$

Writing Leibnitz' rule as

$$\int_b^h \frac{\partial C}{\partial x} dy = \frac{\partial}{\partial x} \int_b^h c dy - [C]_h \frac{\partial h}{\partial x} + [C]_b \frac{\partial b}{\partial x} \quad (3.18)$$

and again using Fickian analogy

$$\overline{u''c''} = -K_x \frac{\partial \bar{c}}{\partial x} \quad (3.19)$$

where

$K_x$  = a dispersion coefficient

$\nabla \cdot V = 0$  for a fluid of constant mass density

$\frac{\partial v_s}{\partial y} = 0$ , i.e., settling velocity is constant over the depth.

58. The depth-integrated equation for mass conservation reduces to

$$\frac{\partial C}{\partial t} + u \frac{\partial C}{\partial x} + w \frac{\partial C}{\partial z} = \frac{\partial}{\partial x} D_x \frac{\partial C}{\partial x} + \frac{\partial}{\partial z} D_z \frac{\partial C}{\partial z} + S \quad (3.20)$$

where  $D_x = K_x + E_x$  is the effective turbulent diffusion coefficient. The velocities and concentration in the above equation are both time and depth averaged. For the depth-averaged equation (3.20), the source/sink term  $S$  is the rate of erosion or deposition. At solid boundaries such as the banks  $\frac{\partial c}{\partial n}$  equals 0, where  $n$  is the normal direction. The breadth-averaged equation is

$$\frac{\partial C}{\partial t} + u \frac{\partial C}{\partial x} + (v + v_s) \frac{\partial C}{\partial y} = \frac{\partial}{\partial x} D_x \frac{\partial C}{\partial x} + \frac{\partial}{\partial y} D_y \frac{\partial C}{\partial y} + S \quad (3.21)$$

There can be no flux across the free surface and the boundary condition there may be written as

$$\left\{ uc - D_x \frac{\partial c}{\partial x} \right\} n_x + \left\{ (v + V_s)c - D_y \frac{\partial c}{\partial y} \right\} n_y + \left\{ wc - D_z \frac{\partial c}{\partial z} \right\} n_z = 0 \quad (3.22)$$

where  $n_x$ ,  $n_y$ , and  $n_z$  are the components of the unit normal to the free surface.

At the bed interface, whatever material convects or diffuses out is considered to be part of the depositional flux. The normal diffusive flux  $f_n$  is specified as

$$f_n = \dot{\epsilon} + \left| v_s c \frac{\tau_b}{\tau_{cd}} \right| \quad (3.23)$$

$$\left( \frac{\tau_b}{\tau_{cd}} = 1 \text{ if } \tau_b > \tau_{cd} \right)$$

where  $\dot{\epsilon}$  is the normal flux due to erosion and the second term is the part of the depositional flux that is resuspended and is always positive.

59. For both the vertical and horizontal models it is necessary to solve an equation of the form

$$\frac{\partial C}{\partial t} + u \frac{\partial C}{\partial x} + w \frac{\partial C}{\partial z} = \frac{\partial}{\partial x} D_x \frac{\partial C}{\partial x} + \frac{\partial}{\partial z} D_z \frac{\partial C}{\partial z} + \alpha_1 C + \alpha_2 \quad (4.1)$$

which is a second-order, linear, parabolic, partial differential equation. Traditional time marching solutions would involve the solution of the elliptic spatial equation which results on discretizing the time derivative alone. Except for schemes which are fully implicit in the space dimensions, high ratios of convective transport to diffusive transport result in instability.

60. The finite element method (FEM) is used in this model in preference to the finite difference method (FDM) for the following reasons:

- a. The FEM permits the use of arbitrarily shaped elements without loss in the order of convergence; the quadrilateral elements used in this study may even have curved sides.
- b. Regions of rapid change in which it would be desirable to concentrate elements and "islands" in the domain are handled easily by the FEM.
- c. Derivative boundary conditions require special treatment in the FDM, whereas in the FEM they are included directly.
- d. Stability is less of a problem with the FEM.

61. The main disadvantage of the FEM is the more complex formulation and coding.

62. It is more economical, in terms of computational effort and computer memory, to solve the elliptic equation that results by treating the term  $(\partial c/\partial t)$  as an instantaneous constant and then marching in time. The elliptic equation

$$u \frac{\partial C}{\partial x} + w \frac{\partial C}{\partial z} - \frac{\partial}{\partial x} D_x \frac{\partial C}{\partial x} - \frac{\partial}{\partial z} D_z \frac{\partial C}{\partial z} - \alpha_1 C + Q = 0 \quad (4.2)$$

where  $Q = (\partial c/\partial t) - \alpha_2$  is first solved by the finite element method.

The transient problem is then solved by a finite difference scheme. This method yields a more accurate solution than the finite element in both space and time.

### Application of the Finite Element Method

63. The finite element method is an approximate method of solving differential equations and is described in a number of texts such as Zienkiewicz (31).

64. The method is applied in the following basic steps:

- a. Divide the domain into a number of finite elements.
- b. Approximate the dependent variable within each element and express this approximation in terms of the unknown values at the element node points - the number and location of the nodes must ensure continuity of dependent variable values across element boundaries.
- c. Minimize an appropriate measure of error so that a set of simultaneous equations results.
- d. Include the boundary conditions.
- e. Solve the resulting set of equations for the node point unknowns.

65. Quadrilateral, isoparametric elements with a quadratic approximation for both the geometry and concentration are used. Parabolic element sides are therefore permissible.

66. Variational functionals for equation 4.1 have been presented by Guymon et al. (9) and Smith et al. (25). However, these measures of error have very limited applicability due to the inability of existing computers to handle the exponentials involved. The Galerkin Weighted Residual Method, which does not encounter such problems, is used in this solution.

#### Galerkin weighted residual method

67. The governing differential equation 4.2 can be written as

$$L(C) = 0 \quad (4.3)$$

where  $L$  is a differential operator.

68. If the approximate concentration  $\hat{C}$  given by

$$\hat{C} = N_i c_i \quad i = 1, 8 \quad (4.4)$$

(where  $N_i$  are the shape functions - see Appendix A) is substituted for  $C$  in equation 4.3, a residual  $r(x, z)$  would result, i.e.

$$L(\hat{C}) = r(x, z) \quad (4.5)$$

$x, z \in D$

where  $D$  = entire domain.

69. The approximation  $\hat{C}$  satisfies the concentration boundary conditions exactly, although it would not in general satisfy the derivative boundary conditions exactly. Therefore, both on the element interfaces and external boundaries, it must be required that the algebraic sum of the normal concentration fluxes from adjacent elements and any source or sink equals zero.

70. Then

$$q_i^+ + q_i^- + q_i^s = 0 \quad (4.6)$$

$$\xi \in \ell_i, \quad i = 1, NL$$

where

- NL = number of internal and external boundaries  $\ell_i$
- $q_i^+$  = outward normal flux from one element
- $q_i^-$  = flux from adjacent element
- $q_i^s$  = flux from source on the boundary  $i$
- $\xi$  = variable length along the boundary.

On external boundaries, only one element contributes to the flux, so that  $q_i^- = 0$ .

71. Since the fluxes,  $q_i^+$  and  $q_i^-$ , in equation 4.6 are also computed from the approximate concentration  $\hat{C}$  an additional residual  $\rho(\xi)$  would result, i.e.,

$$\rho(\xi) = \hat{q}_i^+ + \hat{q}_i^- + q_i^s$$

$$\xi \ni \ell_i, \quad i = 1, \text{NL} \quad (4.7)$$

where  $\hat{q}$  are approximate fluxes.

72. Then the total residual  $R(x,z)$  over the entire domain  $D$  is given by

$$R(x,z) = \rho(x,z) + r(x,z) \quad (4.8)$$

73. The Galerkin method applied to this system yields

$$\sum_{i=1}^{\text{NE}} \iint_{D_{\text{ne}}} N_j L(\hat{c}) \, dx dy + \sum_{i=1}^{\text{NL}} \int_{\xi} N_j \rho \, d\xi = 0 \quad (4.9)$$

where

NE = number of elements

$D_{\text{ne}}$  = element subdomain

NL = number of element boundaries

$j$  = number of node points in each element.

74. The diffusion terms in the above equation are second derivatives and would require continuity of slopes at all element interfaces to avoid singularities in these terms (31). To avoid this restriction the second derivatives are reduced to first derivatives by the transformation described next.

#### Transformation of the diffusion terms

75. Consider the equation

$$\int_V N L(C) \, dV = 0 \quad (4.10)$$

on some domain  $V$ , where  $L$  is the same differential operator as before.

76. Then 4.10 may be written in vector form as

$$\int_V N \{ \vec{V} \cdot \nabla C - \nabla \cdot \vec{F} - \alpha_1 C + Q \} dV = 0 \quad (4.11)$$

where the vector operators "del" and "grad" are two-dimensional (x and z directions);  $N(x, z)$  and  $C(x, z)$  are scalar fields;  $\vec{F} = D \nabla C$  is the diffusive flux vector; and  $D$  is a tensor. Both  $N$  and  $C$  are continuous in  $V$ .

77. By a vector identity

$$N \nabla \cdot \vec{F} = \nabla \cdot (N \vec{F}) - (\nabla N) \cdot \vec{F} \quad (4.12)$$

78. According to the Divergence Theorem

$$\int_V \nabla \cdot (N \vec{F}) dV = \int_S N \vec{F} \cdot \vec{n} ds \quad (4.13)$$

where  $\vec{n}$  is the outward normal to the surface  $S$  which contains the domain  $V$ .

79. Then

$$\int_V N \nabla \cdot \vec{F} dV = \int_S N \vec{F} \cdot \vec{n} dS - \int_V (\nabla N) \cdot \vec{F} dV \quad (4.14)$$

80. Hence

$$\begin{aligned} \int_V N L(C) dV &= \int_V \left[ N \vec{V} \cdot \nabla C + (\nabla N) \cdot (D \nabla C) + N(Q - \alpha_1 C) \right] dV \\ &\quad - \int_S (N D \nabla C) \cdot \vec{n} ds \end{aligned} \quad (4.15)$$

81. If the above relationship is substituted in equation 4.9

$$\begin{aligned}
& \sum_{ne=1}^{NE} \iint_{D_{ne}} \left[ N_j \left( \rho + u \frac{\hat{\partial C}}{\partial x} + w \frac{\hat{\partial C}}{\partial z} - \alpha_1 C \right) + \frac{\partial N_j}{\partial x} D_x \frac{\hat{\partial C}}{\partial x} \right. \\
& \quad \left. + \frac{\partial N_j}{\partial z} D_z \frac{\hat{\partial C}}{\partial z} \right] dx dz - \oint_{ne} N_j \left( D_x \frac{\hat{\partial C}}{\partial x} n_x + D_z \frac{\hat{\partial C}}{\partial z} n_z \right) d\ell \\
& \quad + \sum_{i=1}^{NL} \int_{\xi} N_j (\hat{q}_i^+ + \hat{q}_i^- + q_i^s) d\xi = 0 \tag{4.16}
\end{aligned}$$

where  $\oint$  is the contour integral over the boundary  $\ell$  of each element and  $n_x, n_z$  are the components of the outward normal to the element subdomain  $D_{ne}$ .

82. By Fick's Law

$$q_x = D_x \frac{\partial C}{\partial x} \quad \text{etc.} \tag{4.17}$$

83. Therefore,

$$\begin{aligned}
& \sum_{i=1}^{NL} \int_{\xi} N_j (\hat{q}_i^+ + \hat{q}_i^-) d\xi = \\
& \sum_{ne=1}^{NE} \int_{ne} N_j \left\{ D_x \frac{\hat{\partial C}}{\partial x} \cdot n_x + D_z \frac{\hat{\partial C}}{\partial z} \cdot n_z \right\} d\ell \tag{4.18}
\end{aligned}$$

and equation 4.16 may be written as

$$\sum_{ne=1}^{NE} \iint_{D_{ne}} \left[ N_j \left\{ Q + u \frac{\partial \hat{C}}{\partial x} + w \frac{\partial \hat{C}}{\partial z} - \alpha_1 \hat{C} \right\} + \frac{\partial N_j}{\partial x} D_x \frac{\partial \hat{C}}{\partial x} + \frac{\partial N_j}{\partial z} D_z \frac{\partial \hat{C}}{\partial z} \right] dx dz + \sum_{i=1}^{NL} \int_{\xi} N_j q_i^S d\xi = 0 \quad (4.19)$$

84. The concentration or diffusive flux must be specified along the boundaries as boundary conditions. The quantities in 4.19 are derived from the shape functions as in Appendix A.

### Transient Problem

85. Equation 4.19 may be written as the matrix differential equation

$$[T] \frac{\partial \{C\}}{\partial t} + [K] \{C\} + \{F\} = 0 \quad (4.20)$$

where

$$[T] = \iint_D [N]^T [N] dx dz$$

[K] = steady state system coefficient matrix

$$\{F\} = - \iint_D [N]^T \{\alpha_2\} dx dy + \int_{\xi} [N]^T \{q\}^S d\xi$$

86. The area integrals are for the entire domain and  $\xi$  is the boundary contour. The derivation of these arrays is presented in Appendix A.

87. If the above equation is discretized with a Crank-Nicolson type scheme in time

$$\left\{ \frac{[T]}{\Delta t} + \theta [K]^{n+1} \right\} \{C\}^{n+1} = \left\{ \frac{[T]}{\Delta t} - (1 - \theta) [K]^n \right\} \{C\}^n + \theta \{F\}^{n+1} + (1 - \theta) \{F\}^n \quad (4.21)$$

where  $\theta$  = implicitness factor ( $\theta = 1$ , fully implicit).

88. This is a two point recurrence relationship between the concentrations  $C^{n+1}$  and  $C^n$ , at time steps  $(n+1)$  and  $n$ . It is this equation that is solved to yield the transient concentrations at each time step.

### The Bed

89. The sediment bed is considered to be composed of a number of layers of known bulk density, shear strength, critical shear stress for erosion, and thickness. The local bed elevations, with reference to some fixed datum, and the layer properties are the initial bed conditions. As transport occurs in the fluid domain, there is interchange between the material on the bed and that in suspension by the processes of erosion and deposition. The bed is treated on an element by element basis, so that the bed properties and elevation within each element are assumed constant.

90. When deposition occurs in a time interval of duration  $\Delta t$ , for a particular element, the dry mass of sediment  $M$  transferred to the bed is given by

$$M = \frac{dC}{dt} \times \Delta t \times V \quad (4.22)$$

where  $dC/dt$  = rate of deposition obtained from equation 3.5, and  $V$  = volume of suspension in the element. The rate of deposition varies with time and the value used for the time interval is the temporal average. As deposition continues, the increased overburden pressure causes the material below to consolidate and consequently increase its density and resistance to erosion. Krone (13) found that an overburden

thickness of about 1 inch (2.5 cm) causes the aggregate forming the bed to reduce to the next lower order. The densities and shear strengths for different orders of aggregation of a number of sediments were presented in Table 2.2.

91. The thickness  $T$  of deposit formed on the bed by dry mass  $M$  is computed as

$$T = \frac{(\rho_s - \rho_w)}{\rho_s(\rho_B - \rho_w)} \times \frac{M}{A} \quad (4.23)$$

where

$\rho_s$  = density of clay particle

$\rho_w$  = density of water

$\rho_B$  = bulk density of layer

$A$  = area of element for horizontal model; (length of base x width) for vertical model.

92. If  $T$  is greater than the characteristic thickness, 1 inch in this case, more than one layer would be added to the bed. In such a case the mass  $M$  should be divided into the number of layers formed with the appropriate bulk density for each layer.

93. Erosion occurs when the shear stress at the bed is greater than the critical shear stress of the uppermost layer. Each successive layer is then tested for possible erosion. When mass erosion occurs the contribution to the source term  $\Delta S$  due to the erosion of one layer is

$$\Delta S = \frac{\rho_s(\rho_B - \rho_w)}{(\rho_s - \rho_w)} \times \frac{T}{d\Delta t} \quad (4.24)$$

where  $d$  = average depth of flow in the element.

94. It is possible to check the accuracy of the numerical scheme by solving certain special forms of the governing equation that have known exact solutions. The numerical solution obtained can be compared with the exact solution to determine stability and order of convergence.

### Test Problems

95. The following equations which apply to a number of physical problems were solved with the finite element model. The usual plots of numerical and exact solutions are not presented since, in most cases, the difference between the two is not discernible on an ordinary graph. However, the magnitude of the error in each case can be seen in the section entitled "Convergence Characteristics."

#### Steady state one-dimensional convection-diffusion

96. Equation

$$u \frac{dC}{dx} - D_x \frac{d^2C}{dx^2} - S = 0 \quad (5.1)$$

where  $S =$  constant source-sink term.

Boundary Conditions

$$C(0) = a \quad (5.2)$$

$$\left. \frac{dC}{dx} \right|_L = 0$$

Exact Solution

$$C = a + \frac{SD_x}{u} \left\{ e^{-N} P_e - e^{-N} P_e (1-x/L) \right\} + \frac{Sx}{u} \quad (5.3)$$

where  $L$  = length of system and  $N_{pe} = uL/D_x$  is the Peclet number, which is the ratio of convective transport to diffusive transport.

97. A rectangular grid with elements of equal length was used in the numerical solution. The values of the parameters used were  $S = 5$ ,  $L = 1$ ,  $u = 1$ ,  $a = 1$ , and  $D_x = 1$ . The largest relative error obtained, i.e., for the run with one element, was  $4 \times 10^{-3}$ .

#### Laplace equation

98. The Laplace Equation was solved for a rectangular domain,  $0 \leq x \leq a$ ,  $0 \leq y \leq b$ , with a parabolic boundary condition for a quantity such as temperature, specified on  $y = 0$ .

99. Equation

$$D_x \frac{\partial^2 C}{\partial x^2} + D_y \frac{\partial^2 C}{\partial y^2} = 0 \quad (5.4)$$

Boundary Conditions

$$\begin{aligned} C &= f(x), & y &= 0, & 0 < x < a \\ C &= 0, & y &= b, & 0 < x < a \\ C &= 0, & x &= 0, & 0 < y < b \\ C &= 0, & x &= a, & 0 < y < b \end{aligned}$$

$$\text{with } f(x) = \frac{dx}{2} (a - x) \quad (5.5)$$

Exact Solution

$$C = \sum_{n=1}^{\infty} f_n \sin(n\pi x/a) \sinh\{(b-y)n\pi/a\} / \sinh(n\pi b/a)$$

where

$$f_n = 4d (1 - \cos n\pi) / n^3 \pi^3 \quad (5.6)$$

100. Due to the large arguments in the hyperbolic sines, double precision arithmetic must be used to compute the exact solution when using a digital computer. Since the series converges slowly, a

sufficient value of  $n$  must be chosen depending on the accuracy required. The values  $a = 3$ ,  $b = 4$ , and  $d = 40$  were used in the trial solution.

One-dimensional transient heat conduction

101. Equation

$$\frac{\partial C}{\partial t} = D_x \frac{\partial^2 C}{\partial x^2} \quad (5.7)$$

Boundary Conditions

$$\begin{aligned} C &= 0, & 0 < x < 1, & t = 0 \\ C &= C_o, & x = L, & t > 0 \\ \frac{\partial C}{\partial x} &= 0, & x = 0, & t > 0 \end{aligned} \quad (5.8)$$

Exact Solution (Reference 5, p. 100)

$$\frac{C}{C_o} = 1 - \frac{4}{\pi} \sum_{n=0}^{\infty} \frac{(-1)^n}{m} e^{-m^2 \pi^2 T/4} \cos \frac{m\pi x}{2L}$$

where

$$m = 2n + 1, \text{ and } T = \frac{D_x t}{L^2} \quad (5.9)$$

Here  $t$  is the elapsed time. The values  $C_o = 1$ ,  $T = 0.1$ , and  $L = 1$  were used in the test problem.

Heat conduction with radiation

102. This test problem was chosen to check the flux boundary condition formulation that is necessary in the model due to the resuspension term at the bed. The governing equation is the same as equation 5.7 with the boundary conditions

$$\begin{aligned}
C &= 0 & , & & 0 \leq x \leq l, & & t = 0 \\
C &= C_0 & , & & x = l, & & t > 0 \\
\frac{\partial C}{\partial x} + hc &= 0, & & & x = 0 & & t > 0
\end{aligned} \tag{5.10}$$

103. The exact solution is similar to that given in Reference 5, p. 126, i.e.,

$$\frac{C}{C_0} = \left( \frac{1 + hx}{1 + hL} \right) - \sum_{n=1}^{\infty} \frac{2(\beta_n^2 + h^2 L^2) \sin \beta_n (1-x/L) e^{-\beta_n^2 T}}{\beta_n (hL + h^2 L^2 + \beta_n^2)} \tag{5.11}$$

where  $\beta_n$  are positive roots of  $\beta \cot \beta + hL = 0$ ,  $h$  = linear heat transfer coefficient for the surface, and  $T$  = time factor as defined in equation 5.9. Values of  $h = 0.7$ ,  $C_0 = 2$ , and  $L = 1$  were used.

Transient convection-diffusion

104. Equation

$$\frac{\partial C}{\partial t} + u \frac{\partial C}{\partial x} - D_x \frac{\partial^2 C}{\partial x^2} = 0 \tag{5.12}$$

Boundary Conditions

$$\begin{aligned}
C &= 0 & , & & x > 0, & & t = 0 \\
C &= C_0 & , & & x = 0, & & t > 0 \\
C &= 0 & , & & x = \infty, & & t > 0
\end{aligned} \tag{5.13}$$

The exact solution is derived by Ogata and Banks (19) as

$$\frac{C}{C_0} = \frac{1}{2} \left[ \operatorname{erfc} \left( \frac{1-\xi}{2\sqrt{\xi\eta}} \right) + \exp \left( \frac{1}{\eta} \right) \operatorname{erfc} \left( \frac{1+\xi}{2\sqrt{\xi\eta}} \right) \right] \tag{5.14}$$

where  $\xi = ut/x$  and  $\eta = D_x/ux$ .

105. Here again double precision arithmetic must be used to evaluate the exact solutions when using the computer. A number of runs were made with various Peclet numbers ( $N_{Pe} = uL/D_x$ ). The distance  $x$

which can be considered to be  $\infty$  for solution purposes depends on the velocity  $u$  and the time  $t$ . For  $ut/x \ll 1$  a domain of unit length can be used as was done here.

### Convergence Characteristics

106. An estimate of the maximum absolute truncation error  $\epsilon$  resulting from discretization may be expressed as

$$\epsilon = Kh^m \quad (5.15)$$

where

$K$  = coefficient involving the derivatives of the dependent variable

$h$  = the step size or spacing

$m$  = the order of convergence.

For a stable and consistent numerical scheme, as  $h \rightarrow 0$ , the true solution is approached, both  $K$  and  $m$  become more nearly constant. The exponent  $m$  is termed the asymptotic convergence factor and  $K$  can similarly be termed the asymptotic convergence coefficient. Both of these quantities are important in error estimation.

107. Taking the logarithm of both sides of equation 5.15 yields

$$\log \epsilon = m \log h + \log K \quad (5.16)$$

108. The maximum absolute error produced by a numerical solution is obtained by comparing it with the exact solution at each of the discrete points, so that

$$\epsilon = (\epsilon_i)_{\max}$$

where

$$\epsilon_i = |C_i - C_{\text{ex}}| \quad (5.17)$$

in which  $C_i$  = numerical solution and  $C_{ex}$  = exact solution.

109. The asymptotic gradient of the plot of  $\log \epsilon$  vs.  $\log h$  would be  $m$ , and the intercept at  $h = 1$ ,  $\log K$ . A number of test runs, with progressively larger numbers of elements or smaller time steps, were made for each of the problems described in the previous section. Plots of number of elements vs. maximum absolute error are presented on log-log scale for solutions to the steady state convection-diffusion equation and the Laplace equation in Fig. 5.1 and Fig. 5.2, respectively.

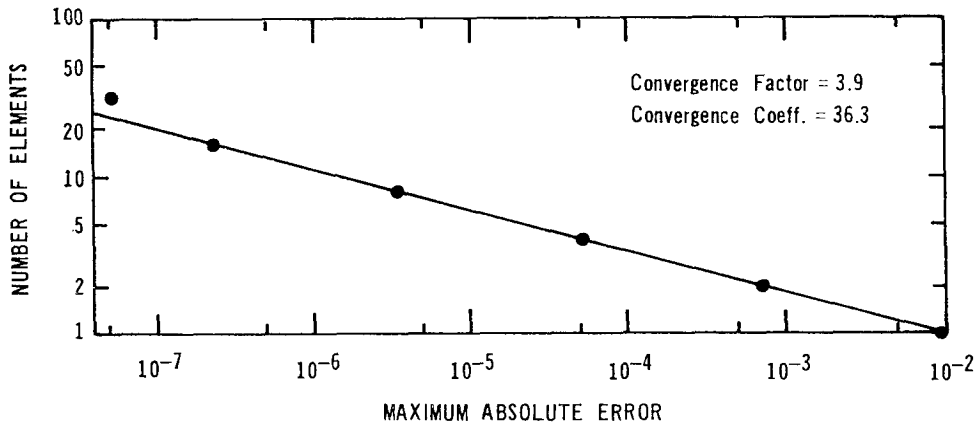


Fig. 5.1. Order of Convergence of Solution to the 1-D Convection-Diffusion Equation

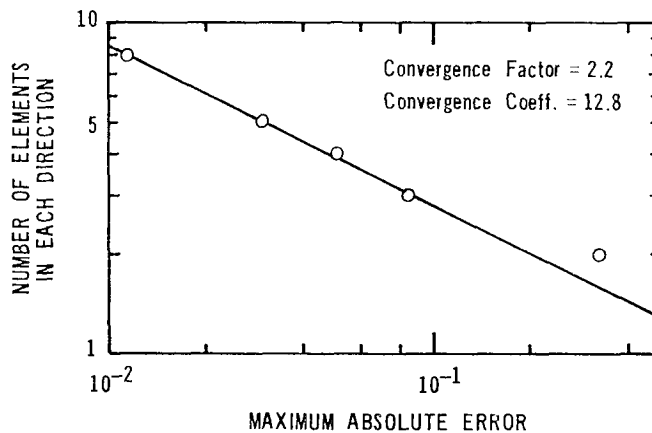


Fig. 5.2. Order of Convergence of Solution to Laplace Equation

The quadratic approximation within the element would be expected to yield second-order convergence for the steady-state problems (Strang and Fix, 28). However, the one-dimensional convection-diffusion solution shows quadratic convergence. The reason for this increased accuracy may be the nullification of some of the higher derivatives in the error term for this particular problem.

110. In general, for the implicitness factor  $\theta$  other than 0.5, the error term would be

$$\epsilon = \theta(\Delta x^2) + \theta(\Delta t) \tag{5.18}$$

and for  $\theta = 0.5$ ,

$$\epsilon = \theta(\Delta x^2) + \theta(\Delta t^2) \tag{5.19}$$

111. When temporal convergence tests are made, sufficient number of elements must be used to ensure that the spatial error is much smaller than the temporal. Figure 5.3 is the log-log plot of time step size vs.  $|\epsilon_{\max}|$  for the solution to the transient heat conduction equation. Figure 5.4 is a similar plot for the same problem except with radiation at one end.

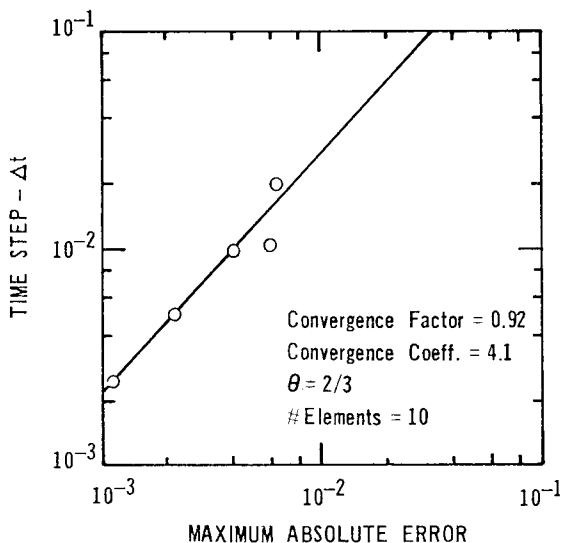


Fig. 5.3. Order of Convergence of Solution to Heat Conduction Equation

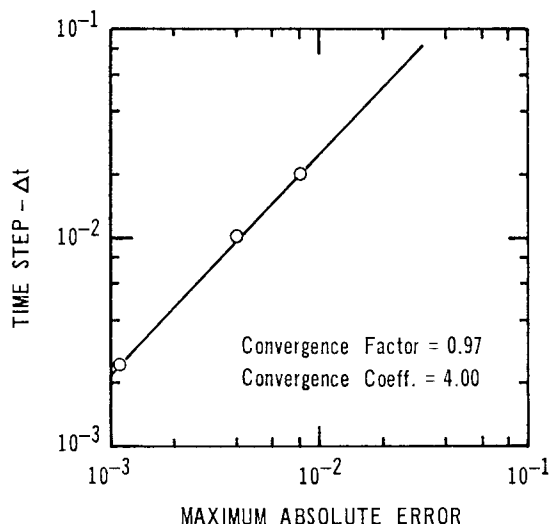


Fig. 5.4. Order of Convergence of Solution to Heat Conduction Problem With Radiation

112. The transient convection-diffusion equation (5.12) was studied in more detail since it possesses all the elements of the full governing equation, i.e., temporal, convective, and diffusive, except that it is one-dimensional in space. The results of these test runs are discussed in the sections that follow.

113. The convergence characteristics of each of the problems solved are presented in Table 5.1. These numbers, when substituted in equation 5.16, give an error bound for the respective problems.

Table 5.1

Convergence Characteristics of Solution

<u>Problem</u>	<u>Asymptotic Convergence Factor</u>	<u>Asymptotic Convergence Coefficient</u>
1-D Convection Diffusion	3.9	36.3
Laplace Equation	2.2	12.8
Heat Conduction	0.92	4.1
Heat Conduction with Radiation	0.97	4.0

Stability

114. Stability alone does not necessarily mean that the deviation between the true solution to a certain partial differential equation and its numerical approximation will be in any sense small. Rather, it implies boundedness of the numerical solution. A numerical solution with a thousand percent error can result from a stable scheme. All that is assured is that if the step size is progressively reduced, more accurate solutions would result. The classical method of obtaining an error estimate when no theoretical error bound is known is to half the step size and compare the results of the two solutions. The difference between the two solutions is an estimate of the error in the second solution (that with the step size halved). This can turn out to be time consuming and expensive in terms of computer costs,

especially in a case such as this where both spatial and temporal discretization is carried out. Some a priori estimate would therefore be of great value.

115. In general, a solution is said to be unstable if errors introduced at some state in the computation, e.g., from erroneous initial conditions or local truncation or round off errors, are propagated without bound throughout subsequent calculations.

116. Both the finite element scheme used to solve the elliptic spatial problem and the implicit finite difference scheme used for the transient problem are theoretically unconditionally stable. However, it is not necessarily true that an unconditionally stable scheme plus an unconditionally stable scheme equals an unconditionally stable scheme.

117. Fortunately, all the test runs made indicate that the combination of the two schemes was in fact stable.

#### Consistency

118. The term consistent applied to a certain numerical procedure means that the procedure will in fact approximate the solution of the differential equation which is to be solved and not some other. Both stability and consistency are necessary for convergence to the true solution as the step size tends toward zero. An example of an inconsistent scheme is the unconditionally stable finite difference scheme proposed by DuFort and Frankel to solve the heat conduction equation. In fact it solves the equation,

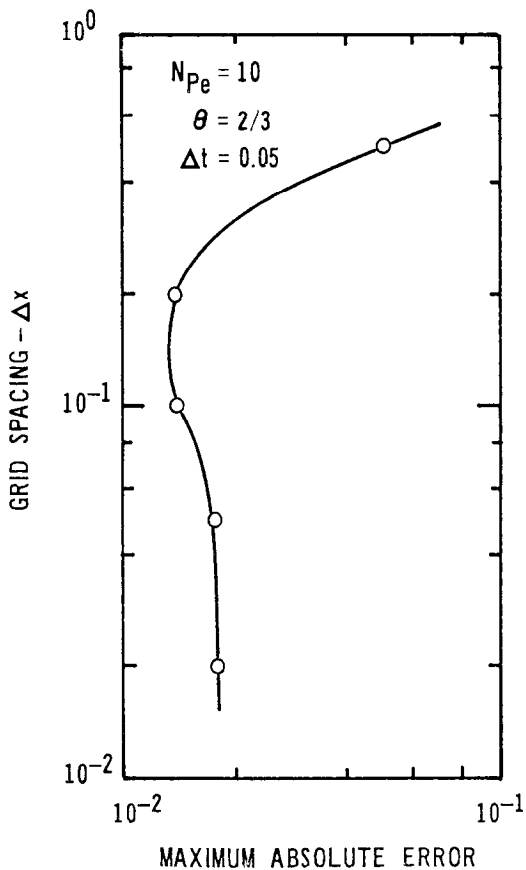
$$\frac{\partial C}{\partial t} = \frac{\partial^2 C}{\partial x^2} - \frac{\partial t}{\partial x} \frac{\partial^2 C}{\partial t^2} \quad (5.20)$$

where the last term is a spurious diffusion type term brought about by discretizing. Similar inconsistency is produced in the finite difference time scheme by the spatial error term in the finite element scheme. The factors that affect the magnitude of this numerical dispersion term are  $\Delta t$ ,  $\Delta x$ , and  $\theta$ . The effect on the solution depends on the ratio of this numerical dispersion term to the physical diffusion coefficient  $D$ .

119. The Peclet number  $N_{Pe}$  is the ratio of convective transport to diffusive transport. High Peclet numbers suppress the diffusion term in equation 5.12 and cause the parabolic equation to tend toward the hyperbolic equation.

$$\frac{\partial C}{\partial t} + u \frac{\partial C}{\partial x} = 0 \quad (5.21)$$

Parabolic equations are dissipative; i.e., errors at one point in the computation are dissipated as the solution proceeds. Hyperbolic equations, on the other hand, are nondissipative. The Peclet number was found to have great influence on the accuracy of the solution.



120. In order to isolate the spatial error term from the temporal error, a number of runs were made for the same time step size,  $\Delta t = 0.05$ , with increasing number of elements,  $N = 1/\Delta x$ . A plot of grid spacing vs.  $|\epsilon_{max}|$  is presented in Fig. 5.5. For this problem, it is seen that the solution is virtually unaffected by using more than ten elements, i.e., the temporal error term dominates after this. Subsequent time convergence tests were carried out with a twenty element grid.

Fig. 5.5. Spatial Convergence for  $\Delta t = 0.05$

121. The first set of temporal convergence tests were performed for problems with various Peclet numbers. Figure 5.6 is a log-log plot of the number of time steps vs.  $|\epsilon_{\max}|$  for Peclet numbers of 1, 10, and 1000. For  $N_{Pe} < 10$ , second-order convergence is achieved--as expected when  $\theta = 0.5$ . However, at  $N_{Pe} = 1000$ , the order of convergence reduces to  $\sim 1$ . It is believed that there is inconsistency produced as the Peclet number is increased. Reducing the time step to  $\Delta t = 0.01$  improves the accuracy considerably as is seen in Fig. 5.7 which is a plot of nondimensional concentration vs. nondimensional length for  $N_{Pe} = 1000$ . The front has advanced to  $x/L = 0.3$  in Fig. 5.7, and the sharp gradient at that point is seen to cause the numerical solution to oscillate about the exact solution for coarse time steps. The gradient for  $N_{Pe} = 10$  is much smaller as seen in Fig. 5.8, where even for  $\Delta t = 0.1$ , the error is relatively small.

122. The next set of runs was designed to determine the effect of changing the implicitness of the time scheme, i.e., the  $\theta$  value. When  $\theta = 0.5$ , a centered difference scheme results and for  $\theta = 1.0$ , a fully implicit scheme. Again, a Peclet number of 1000 was used and the relatively coarse time interval  $\Delta t = 0.5$  was chosen to show the form of the error more clearly. The effect of increasing the value of  $\theta$  is seen vividly in Fig. 5.9. The solution seems more stable for higher  $\theta$  values, but in fact the largest errors for  $\theta = 0.5$  and  $\theta = 1$  are of similar magnitudes. As  $\theta$  is increased, the oscillations about the exact solution are dampened; a numerical dispersion effect is introduced; and inconsistency develops. At  $\theta = 1$  the problem that is solved seems to have a lower Peclet number than 1000.

### Summary

123. The prime objective of making convergence tests on the problems that have been described in this chapter was to verify the accuracy of the formulation and coding. The results indicate that the

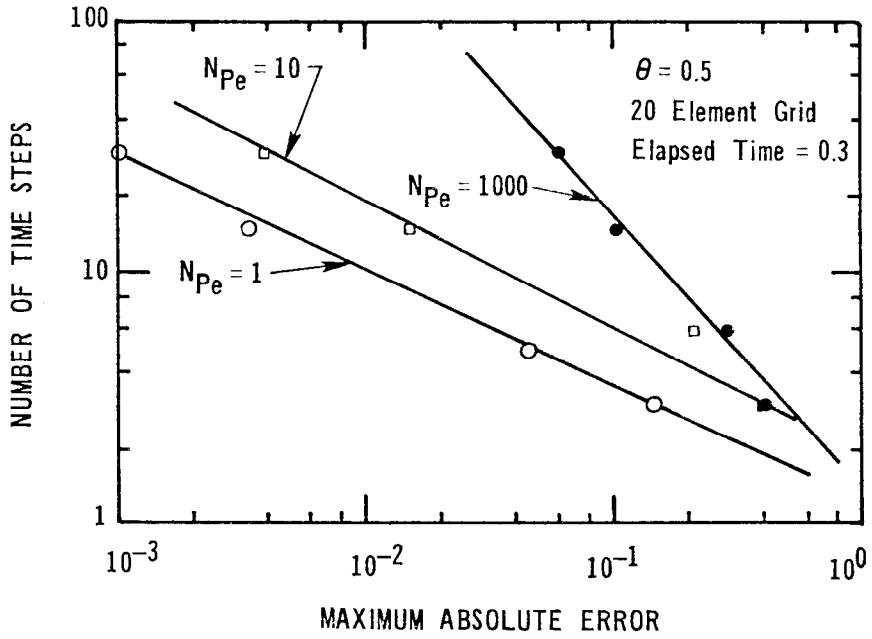


Fig. 5.6. Influence of Peclet Number on Accuracy

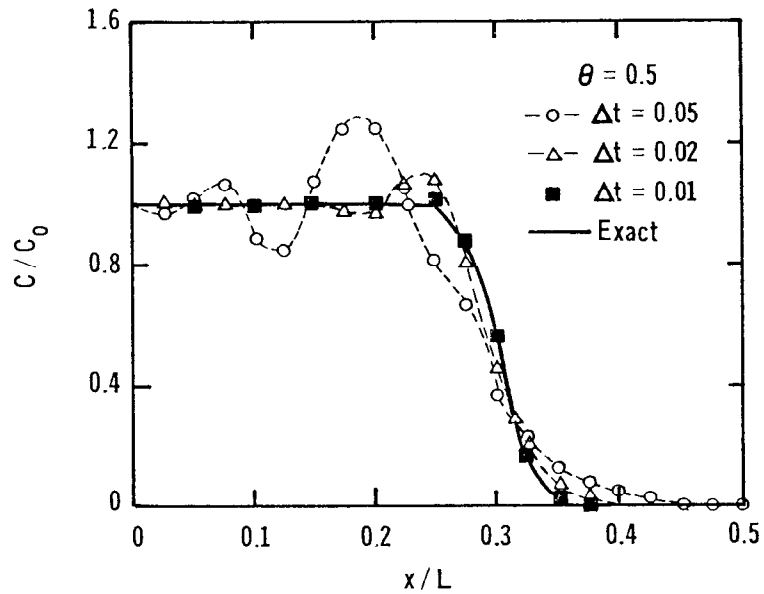


Fig. 5.7. Effect of Reducing Time Step Size,  $N_{Pe} = 1000$

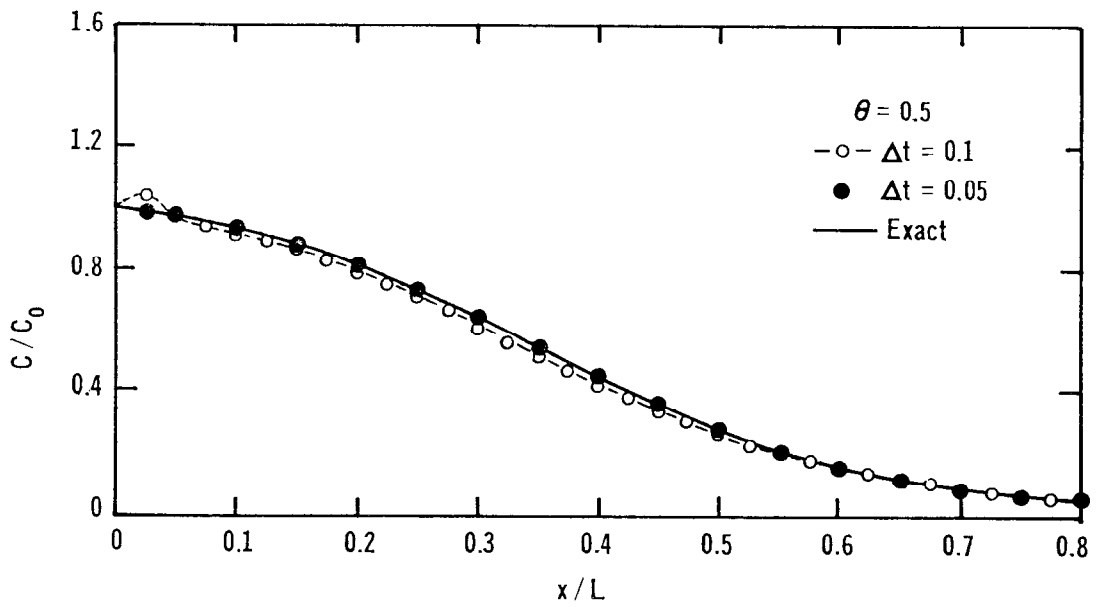


Fig. 5.8. Effect of Reducing Time Step Size,  $N_{Pe} = 10$

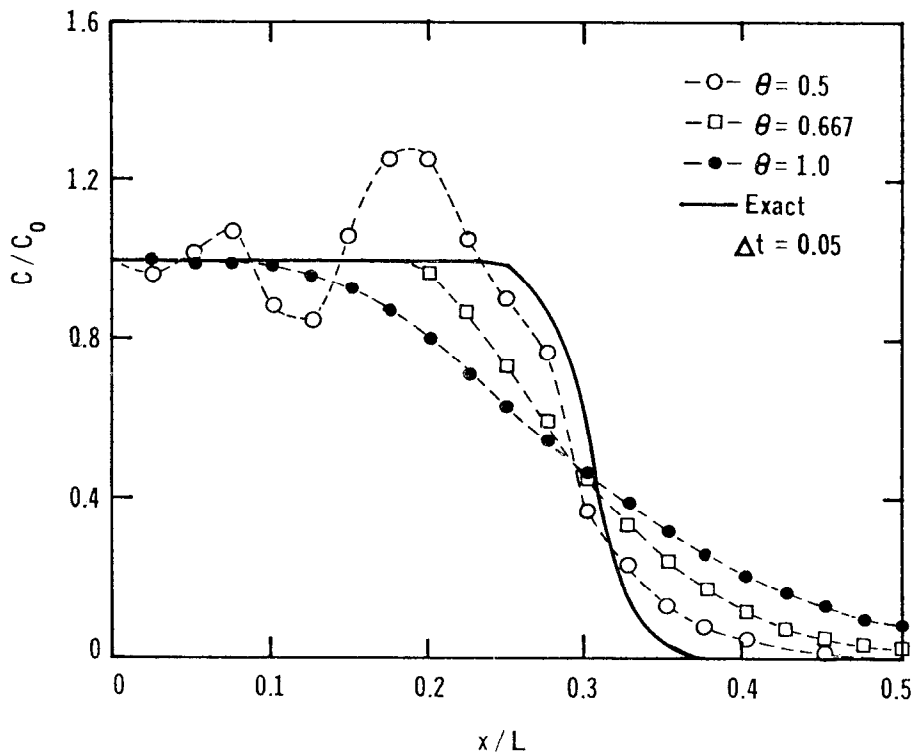


Fig. 5.9. Effect of Changing  $\theta$  Value,  $N_{Pe} = 1000$

program solves the governing equation with theoretically anticipated convergence rates.

124. In addition, the following observations have been made:

- a. High Peclet numbers ( $>$  about 100) cause a deterioration in accuracy. Smaller time step sizes must be used to improve accuracy in such cases.
- b. The numerical scheme is unconditionally stable in the classical sense.
- c. High  $\theta$  values produce smoother solutions due to the introduction of numerical dispersion, which means that the solution becomes inconsistent. However, these smoother solutions are no more accurate than the oscillatory solutions produced by  $\theta = 0.5$ .

## PART VI. SIMULATION OF SEDIMENT TRANSPORT IN THE SAVANNAH ESTUARY

125. Obtaining field or laboratory measurements sufficiently detailed and accurate to verify a two-dimensional transport model is exceedingly difficult. Dispersion measurements that have been made in the past have been made with dyes or were restricted in scope when sediment was used. However, field measurements that should provide more information for testing the sediment model described in this study are now being conducted by the Dredged Material Research Program (DMRP). The original version of the sediment model, SEDIMENT I (1), was tested with shoal measurements in a laboratory flume. The two horizontal dimensions were used in the simulation with a measured velocity field. The model predicted shoaling patterns and rates very well. However, the spatial variation of suspended sediment concentration was negligible in the test, and data which included this effect was sought for the verification of SEDIMENT II.

126. Krone (14) conducted a field study of flocculation as a factor in shoaling processes in the Savannah Estuary, Georgia, under contract to the Committee on Tidal Hydraulics of the U.S. Army Corps of Engineers. Although the measurements in the Savannah are perhaps the most complete with respect to satisfying the information required to make a simulation, certain assumptions had to be made as described later.

### Sediment Transport in the Savannah Estuary

127. The Savannah Estuary is located in Georgia and is a typical example of a partially mixed estuary. It has simple geometry and most of the shoaling occurs in a well-defined reach. A plan of Savannah Harbor presented in Fig. 6.1 shows the portion of the channel subject to rapid shoaling and the locations of the three current measuring and water sampling stations used in the flocculation study (14).

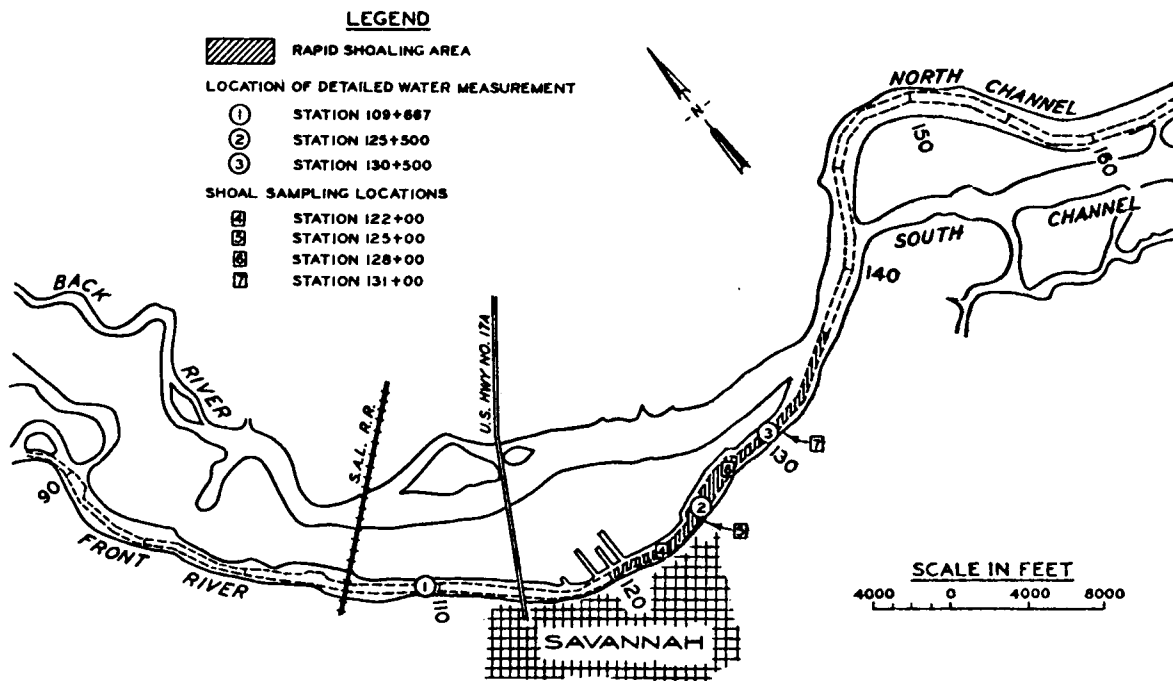


Fig. 6.1. Locations of Water Measurement and Shoal Sampling Stations

128. The material transported in the reach was typically 58% clay and the remainder fine silt. There was little variation in the composition of the shoal material throughout the test reach. Internal shearing, most pronounced during ebb flows, is the principal mechanism for aggregating suspended particles in the estuary. The sampling stations were located in the mixing zone where fresh water mixes with salt water. The partially mixed character of the estuary is evidenced by the large salinity gradients measured in the mixing zone which tend to stabilize the flow and reduce the turbulent diffusion process.

129. The shear stress at the bed is higher during flood than during ebb flows so that layers of the bed having a higher resistance to shear may be suspended during flood. Subsequent ebb flows are not able to resuspend all the layers of the bed resulting in a net upstream movement of the sediment. A schematic diagram summarizing the various processes in the mixing zone is reproduced from Krone (14) in Fig. 6.2.

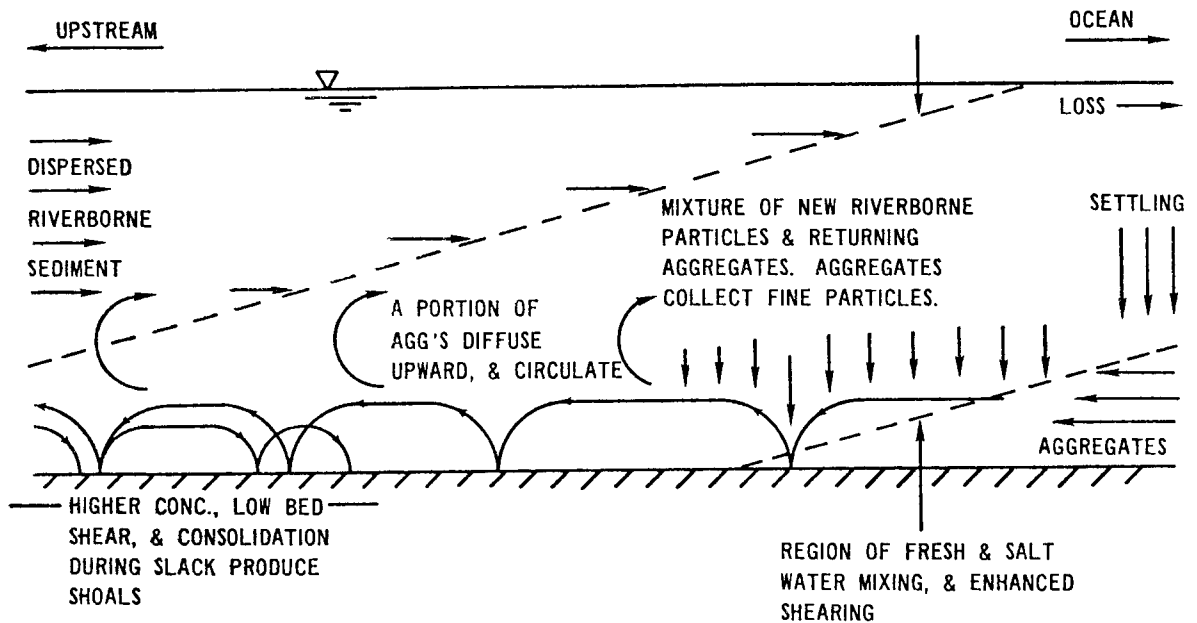


Fig. 6.2. Transport and Shoaling Processes in the Study Area

#### Description of Field Measurements

130. For each of a spring, mean, and neap tidal cycle, vertical distributions of suspended sediment, salinity, and currents were measured at the three stations: 1) at 109 + 667 ft; 2) at 125 + 500 ft; and 3) at 130 + 500 ft, as shown in Fig. 6.1. At each vertical section measurements were made at seven elevations more or less geometrically spaced above the bed - 1, 2, 4, 8, 16, and 25 ft, and at the surface. These profiles were obtained at half-hour intervals simultaneously at each of the three stations during a complete tidal cycle.

131. The bed material in the test reach was a soft mud and shows up as a very faint image on a fathometer trace. Since the currents near the bed determine the shear stress there, it is very important to locate the bed surface accurately, i.e., the elevation at which the flow velocity is zero. A bottom sensor was developed for the field study (14) and considerable care was exercised in locating the bed.

132. Using the steady state vertical concentration equation 2.5, the average settling velocities at each station for the three tides were computed by Krone (14) to be as shown in Table 6.1.

Table 6.1

Aggregate Settling Velocities

<u>Station</u>	<u>Aggregate Settling Velocities, fps</u>		
	<u>Spring Tide</u>	<u>Mean Tide</u>	<u>Neap Tide</u>
109+667			
Ebb	0.028	0.038	0.030
Flood	0.033	--	0.012
125+500			
Ebb	0.014,0.013	0.091	0.084
Flood	0.033	0.017	0.047
130+500			
Ebb	0.151	--	0.016
Flood	0.098	--	0.040

Required Input for Transport Model

133. The information required as input to the model is listed below:

- a. The geometry of the domain, which in this case is bounded by the bed, the free surface, and the sections at stations 1 and 3.
- b. The velocity components  $u$  and  $v$  at each node point for each time step.
- c. The initial concentration at each node point.
- d. The node point concentrations at stations 1 and 3 for each time step. (These are the concentration boundary conditions.)
- e. The effective turbulent diffusion coefficients  $D_x$  and  $D_y$ .
- f. The average settling velocity  $V_s$  ( $t$ , element #) for each element.
- g. The initial bed profile and properties for the bottom elements, i.e., the number of layers, layer thickness, density of each layer, and critical shear stress of each layer.

- h. The critical shear stress for deposition.
- i. Consolidation characteristics of the bed - as material is deposited on the bed, it is crushed by the overburden and becomes denser and more resistant to erosion. A table of the number of different layers with thickness, bulk density, and critical shear strength for each layer must be provided for the dynamic simulation.

134. Items a, c, and d of the above list had been measured. The transient velocity field was generated using a finite element flow model as described in Appendix B. The flow model used the same grid as the transport model so that the velocities at the node points required in item b were produced. The grid was generated by using the automatic grid generator described in Appendix C. This grid generator saves considerable time and effort in the preparation of input data and permits a preview of the grid. The bed shear stress at each bottom node was computed by assuming a logarithmic velocity profile near the bed. The computation of the shear stress by passing a parabola through the bottom three points and differentiating to obtain the velocity profile does not yield very good results since numerical solutions do not match the derivative very well, especially near the boundaries.

135. A contour plotting routine that is especially suited for finite element networks was developed to provide graphical output (see Appendix D). This routine proved invaluable in obtaining a graphical view of the thousands of simulated values.

#### Diffusion coefficients

136. The solution stability analysis in Part V has shown that small diffusion coefficients, i.e., large Peclet numbers, produce large oscillations in the solution. The longitudinal diffusion coefficient  $D_x$  would not be expected to affect the solution significantly as long as it is not so small as to cause the oscillations in the numerical solution or so large as to suppress the convective effects. Contrary to the belief of some researchers, the vertical diffusion coefficient, especially near the bed, is solution determining.

137. A value of  $D_x = 0.5 \text{ m}^2/\text{sec}$  as observed in the Gironde estuary, France, by Sauzay and Allen (27) was used for all runs. The initial values of the vertical diffusion coefficient  $D_y$  used were those computed on a tidally averaged basis for the Savannah by Tesche (29) (see Table 6.2).

Table 6.2

Average Values of Vertical Eddy Diffusivity Used for  
Spring Tide Simulation

<u>Elevation above Bed Surface</u>		<u>Vertical Eddy Diffusivity</u>
<u>Feet</u>	<u>Metres</u>	<u><math>D_y, \text{ m}^2/\text{sec}</math></u>
0 - 1	0.0 - 0.3048	0.0006
1 - 2	0.3048 - 0.6096	0.001
2 - 4	0.6096 - 1.2192	0.002
4 - 8	1.2192 - 2.4384	0.004
8 - 16	2.4384 - 4.8768	0.006
16 - 25	4.8768 - 7.6200	0.004
25 - Surface	7.6200 - Surface	0.003

138. A number of runs were made to calibrate the vertical diffusion coefficients keeping the other parameters constant. The solution was calibrated for two hours using the measured values at mid-station. However, the number of degrees of freedom with the limited time and budget did not permit more than a coarse calibration.

Assumed sediment and bed properties

139. No measurements were made on any of the sediment or bed properties as part of the Savannah field measurement program. Past measurements on similar sediments were therefore used.

140. The critical shear stress for deposition was assumed to be  $0.02 \text{ N/m}^2$  ( $0.2 \text{ dynes/cm}^2$ ). A constant settling velocity of  $0.005 \text{ m/sec}$  was used for the entire tidal cycle. The simulation was begun at the peak of flood when the bed was assumed to have been scoured to

a firm bottom. The initial bed profile, therefore, had zero thickness.

141. The bed layer properties used are given in Table 6.3. The thickness of each bed layer is automatically computed from the bulk density of the sediment using a specified dry weight per square meter in each layer. The value chosen corresponded to a thickness of about .025 m (1 inch) per layer. The properties for the sediment were obtained from the extensive laboratory and field measurements made by Krone (12,14).

Table 6.3

Bed Layer Properties

<u>Layer</u>	<u>Bulk Density</u> <u>kg/m<sup>3</sup></u>	<u>Shear Strength</u> <u>N/m<sup>2</sup></u>
1	107.9	.02
2	108.7	.04
3	109.8	.08
4	111.3	.14
5	113.7	.14
6	117.9	.39
7	126.9	2.2

142. Once the top six layers are filled, further deposition results in the excess being transferred to the seventh layer, which has no restriction on thickness.

Simulation Results

143. The measured and simulated concentration profiles at mid-station were compared to determine the accuracy of the simulation. Figure 6.3 is a series of half-hourly space plots of the logarithm of suspended sediment concentration vs. elevation above the bed, and Fig. 6.4 shows the temporal variation of suspended solids at mid-

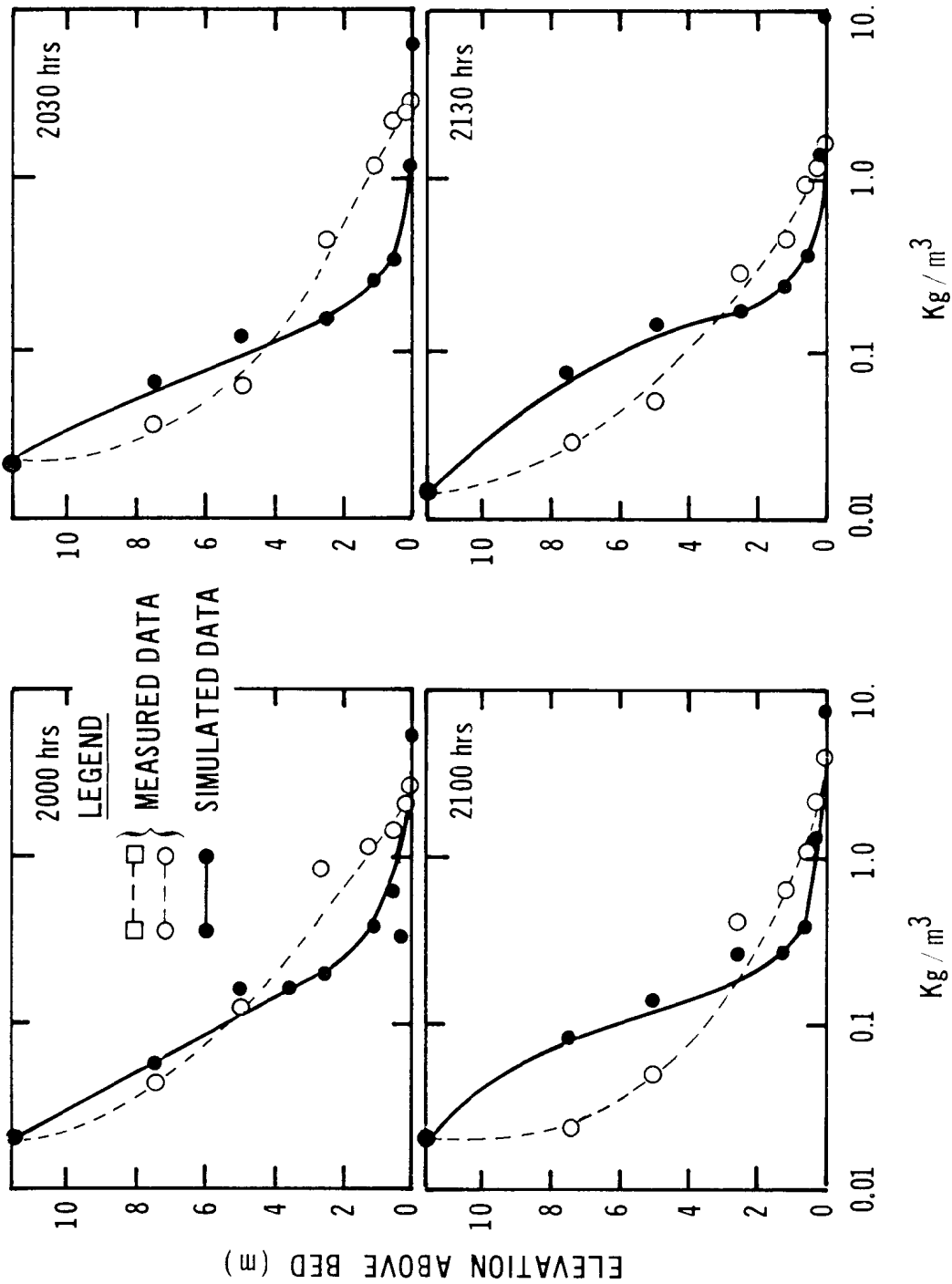


Fig. 6.3. Half-Hourly Suspended Sediment Concentrations at Sta. 125+500, During Spring Tide

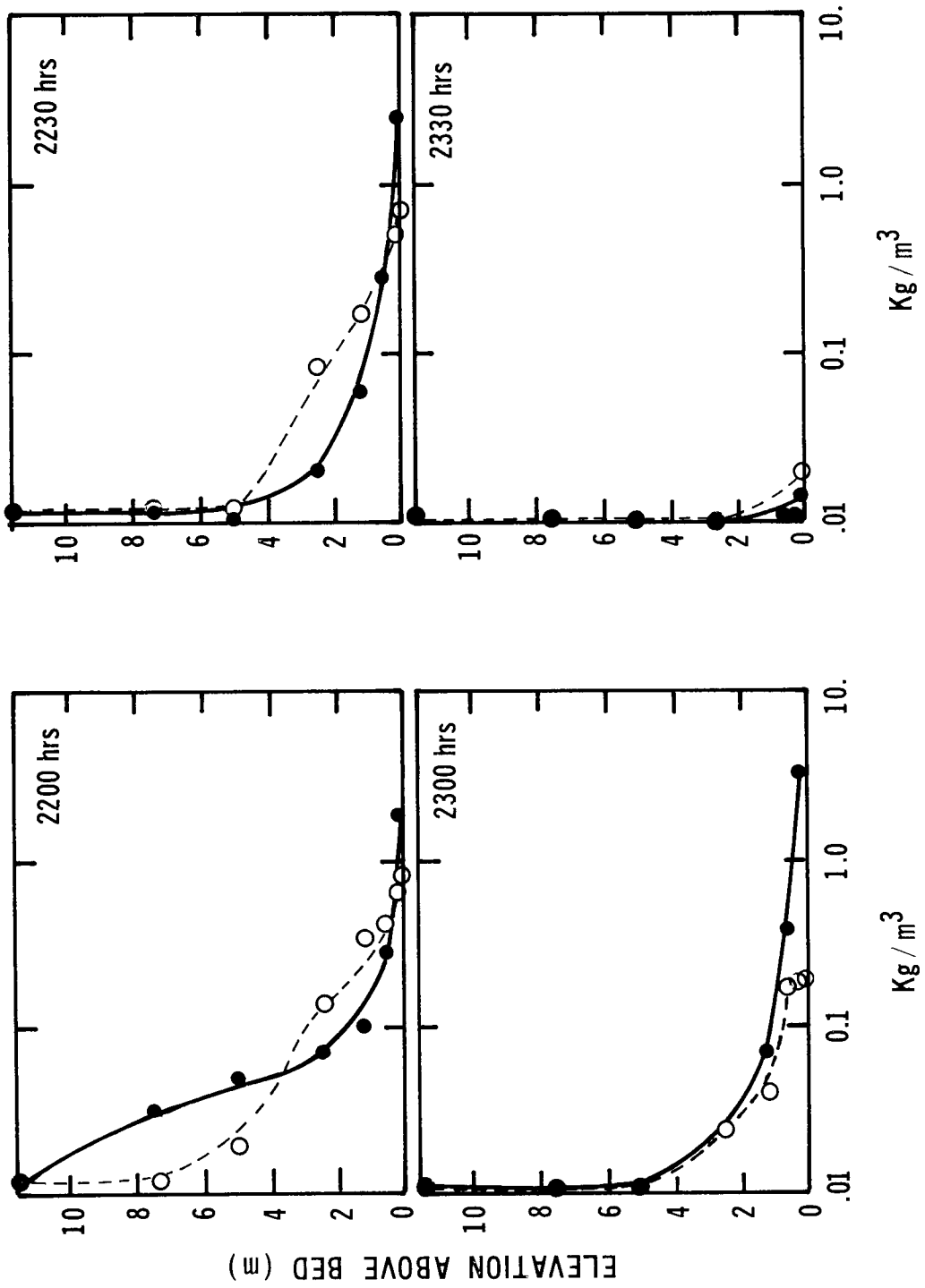


Fig. 6.3 (Continued)

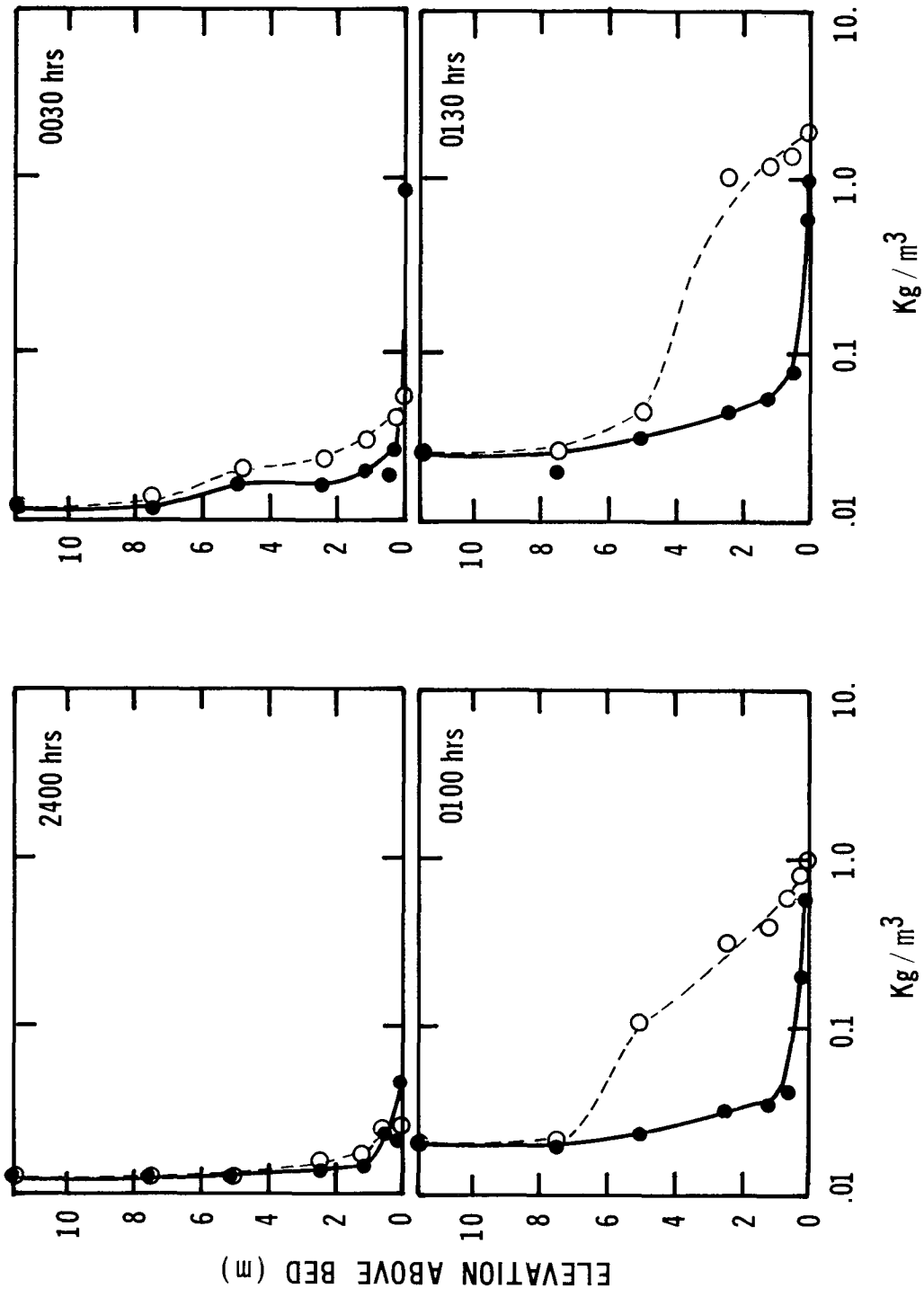


Fig. 6.3 (Continued)

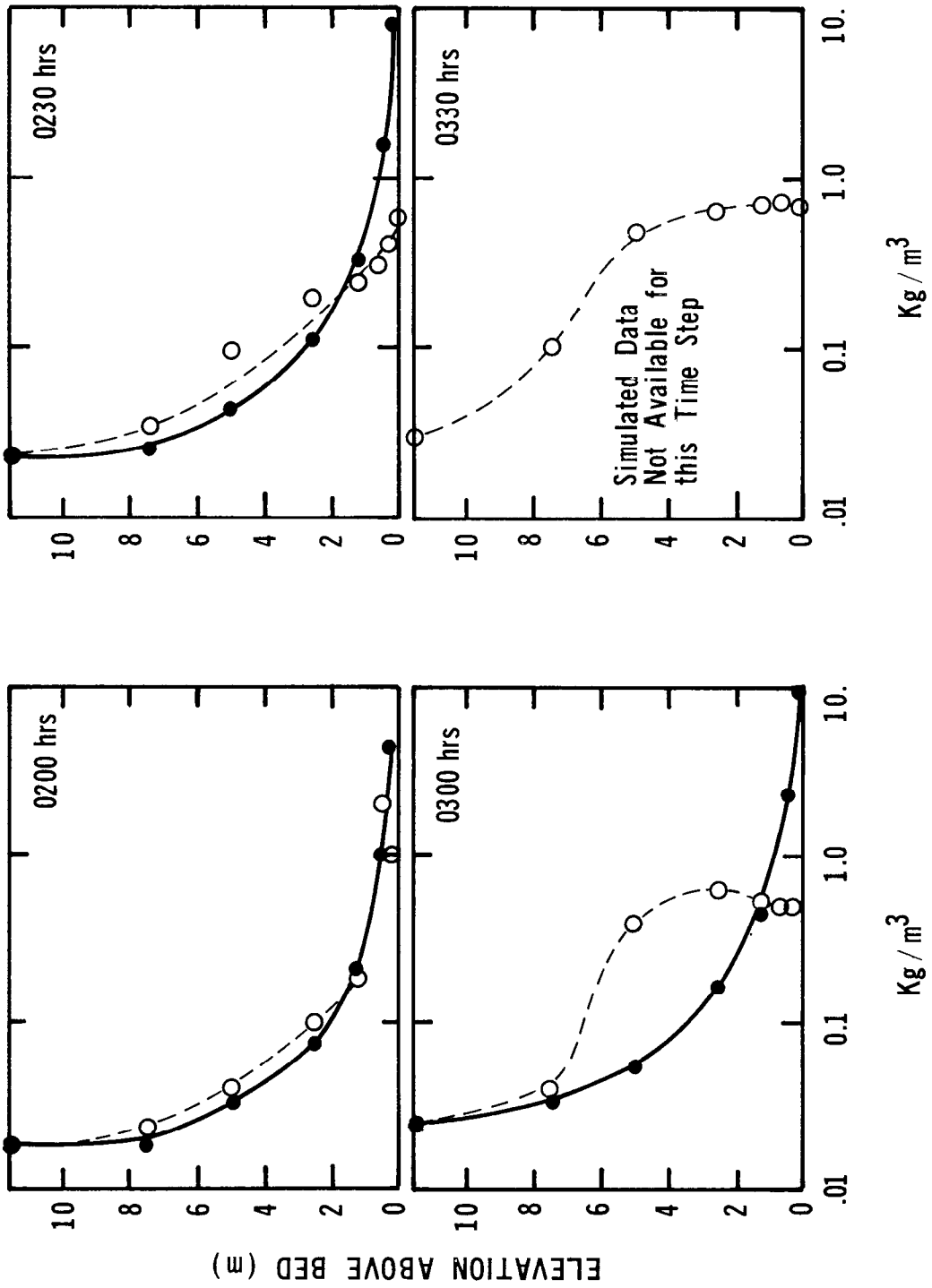


Fig. 6.3 (Continued)

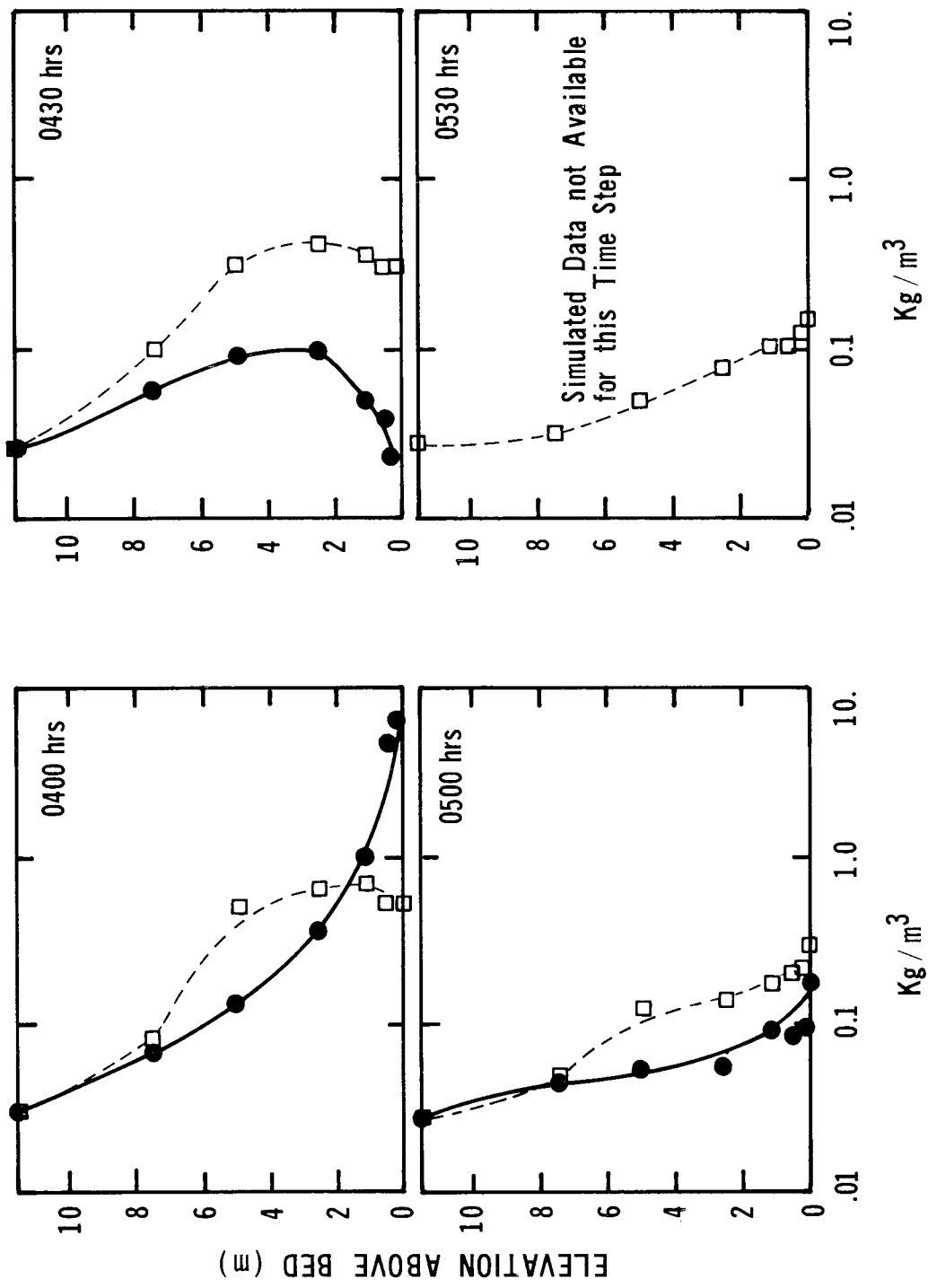


Fig. 6.3 (Continued)

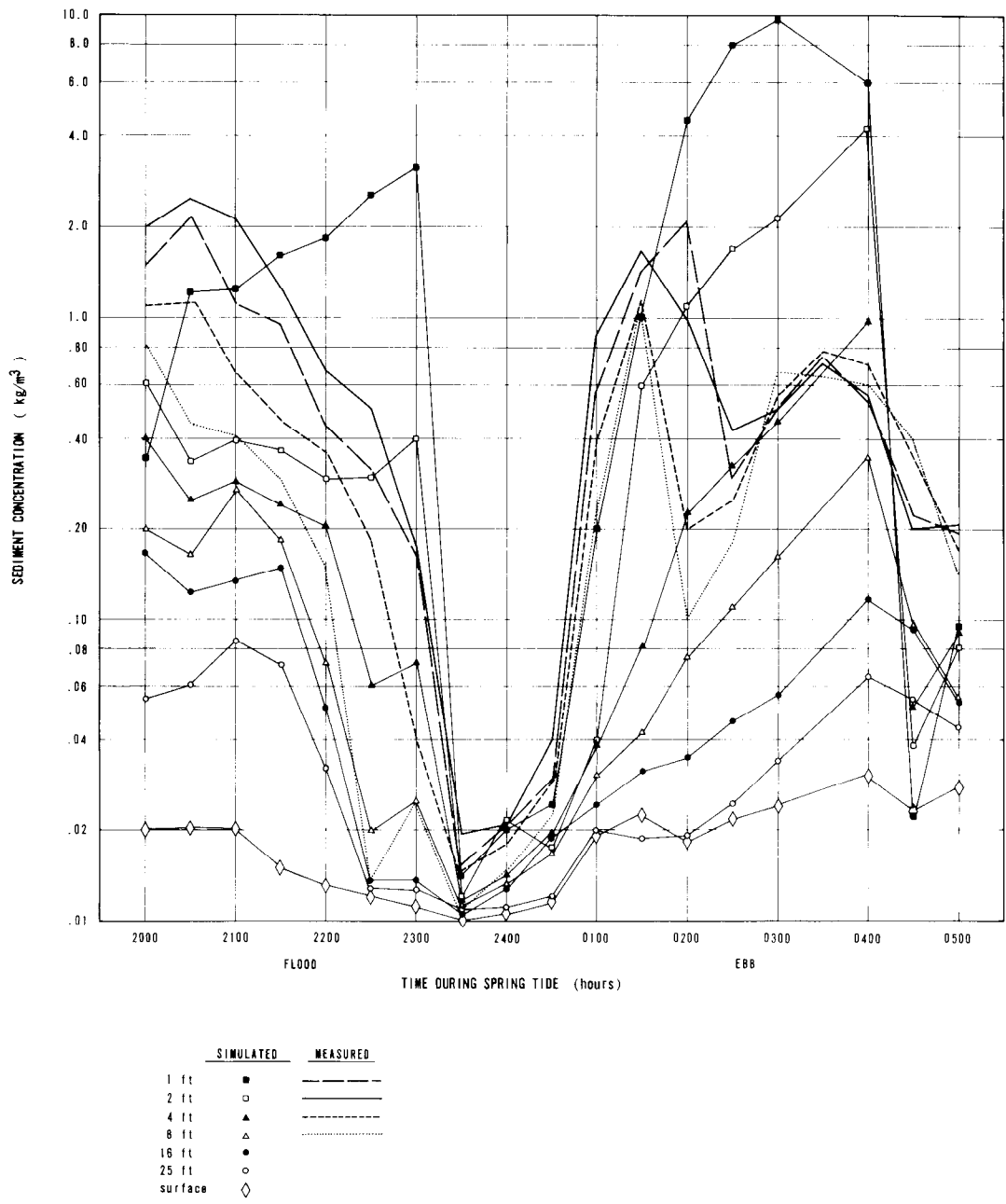


Fig. 6.4. Suspended Sediment Concentrations at Station 125+500, Spring Tide

station.

144. Considering the fact that constant values for settling velocity and diffusion coefficients were used throughout the tidal cycle - due to the lack of a better description in this case, the simulated values of suspended sediment concentrations compare very well with the measurements. When the flow velocities are high, both the concentration and the concentration gradient near the bed are also high. Under these circumstances, measurements of sediment concentrations are prone to the greatest error and it is seen that the simulated values deviate from those measured near the bed at these very times.

145. The simulated values generally yield a higher concentration of sediment near the bed than those measured in the field. This was observed in all the simulations using realistic parametric values. It seems that a fluid mud layer which is mobilized at high current intensities exists on the bottom. It is possible that the bottom sensor did not penetrate this thick mud layer to the actual depth of zero velocity; at these depths even a few centimeters error in locating the bottom would cause a significant difference in the concentration measured due to the very high concentration gradient. An analysis of the measured velocities and concentrations showed that mass was not being conserved in the test reach, especially during high flows. Lateral variations in velocity and concentration and inaccurate location of the bed can account for this error.

146. In an estuary such as the Savannah the sediment settling velocities and the vertical diffusion coefficient are the two parameters that have the greatest effect on the solution. If the response of the model to variations in these parameters was known precisely, it would have made the calibration task much simpler. Since the grid size and time step also have a significant effect on the solution a systematic sensitivity analysis needs to be conducted to obtain model response to the parameters involved.

147. As indicated by Krone (14), the settling velocity of the sediments during ebb are lower than that at flood. If smaller

settling velocities were used during ebb a better comparison may have resulted.

148. The transient bed profile that was simulated is shown in Fig. 6.5. Net upstream excursion of the shoal is seen. The filling up of the depression produced by the dredged area is shown vividly. It is reported that maximum intra-tidal cycle shoal depths are about 3-4 feet in that region, which compares very well with the 1 meter or so of deposit that is predicted. It is interesting to note that there is little deposition in the depression during flood and that it is the ebb flow which fills the dredged area with sediment. The saline wedge which moves along the bottom during flood has far greater ability to scour the bed than the ebb flows which ride over the salt water below.

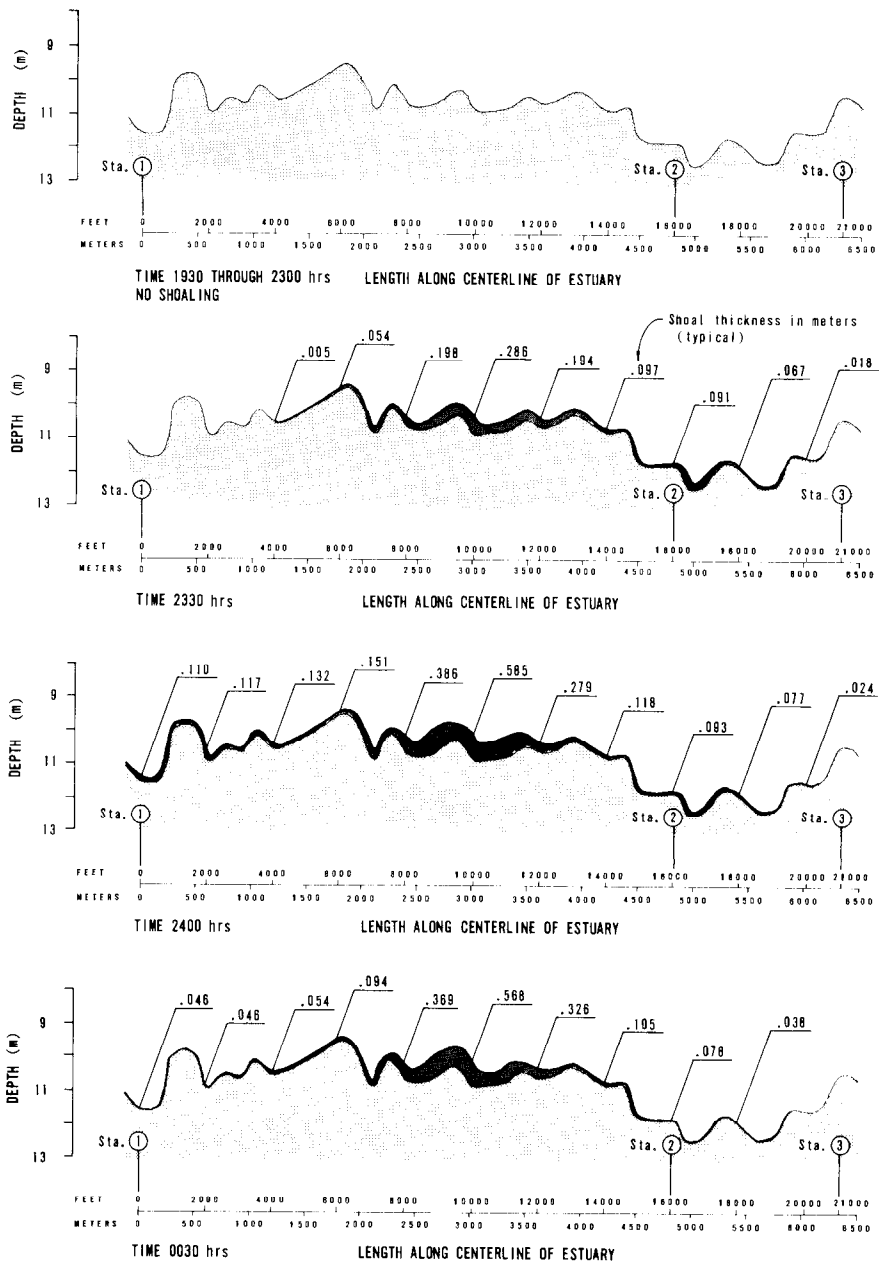


Fig. 6.5. Simulated Average Shoal Thickness, Spring Tide

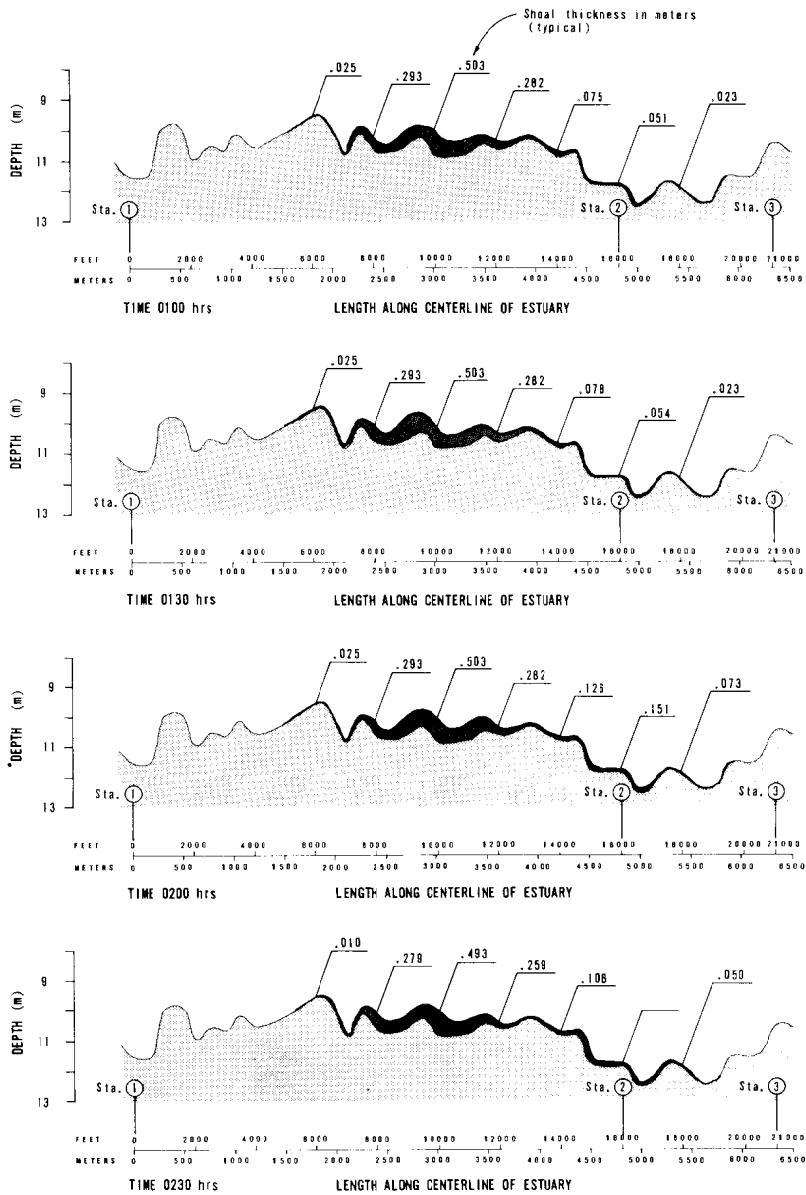


Fig. 6.5 (Continued)

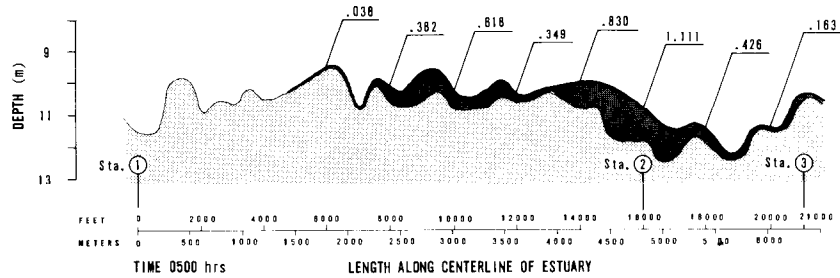
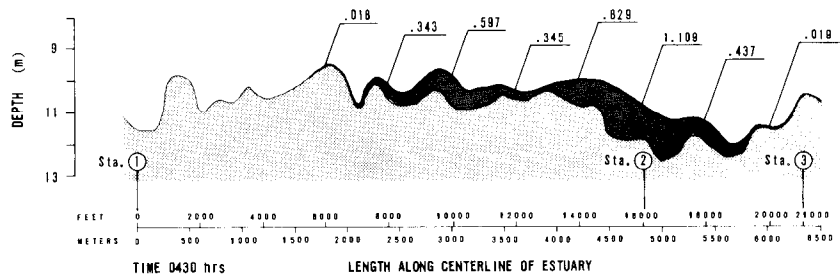
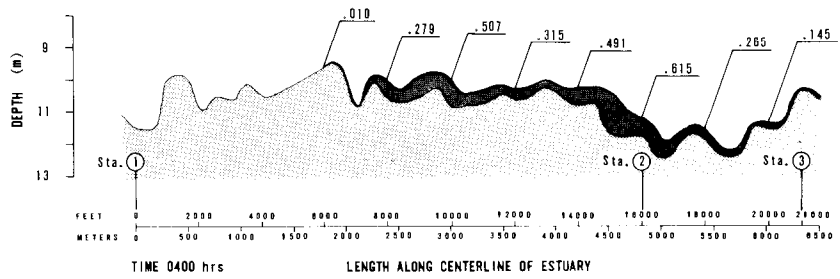
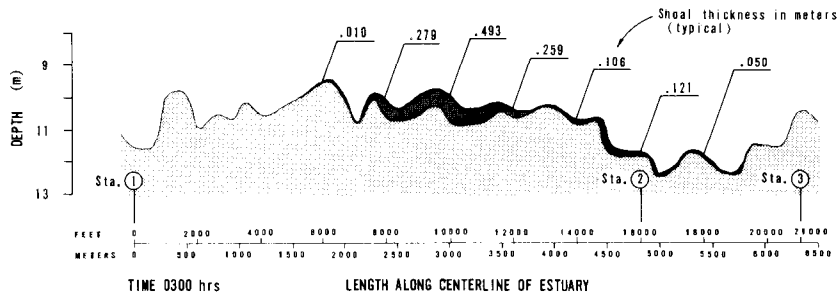


Fig. 6.5 (Concluded)

Conclusions

General

149. Perhaps the most complex situation to model is a stratified, highly turbulent estuary in which continuing aggregation causes rapid change of sediment properties and the nonlogarithmic velocity profiles make the computation of bed shear stress difficult. The Savannah is such an estuary. This problem was chosen for a first full-scale model test only because there does not exist any other data as complete as the information available from the Savannah measurements. Although many important parameters had to be estimated from previous experience, the model showed the essential trends exceedingly well. Better transient concentrations could be obtained by varying the transport parameters systematically. Some field measurement of sediment and bed properties would have reduced the number of variables, thereby reducing the number of trial runs necessary to calibrate the other model parameters. This experience showed the central importance of the vertical diffusion coefficient and of the settling velocities of suspended aggregates.

150. The horizontal problem, i.e., depth averaged ( $x, z$  dimensions), is an order of magnitude less difficult than the vertical problem due to the generally lower concentration gradients and simpler boundary conditions. Relatively shallow extensive estuaries, lakes, reservoirs, and settling ponds fall in this category. Settling velocity and diffusion coefficients have a much smaller effect on these horizontal problems and the model can be applied with minimal parametric information to these situations.

Specific

- a. The two-dimensional finite element model developed and tested under this study predicts suspended sediment concentrations and bed profile in a transient flow field.

- b. The model is applicable to any problem that can be averaged in one of the spatial dimensions and in which a median settling velocity suffices to describe the settling of the suspended phase.
- c. The numerical scheme used is stable for all conditions. However, the accuracy of the solution depends on the Peclet Number ( $N_{pe}$ ), the fineness of the grid, and the time step size.
- d. The simulation of sediment transport in the Savannah estuary is an illustration of the potential applicability of the model. The measured and computed values of sediment concentration are in good agreement except near the bed at high flows. It is possible that there were errors in sensing the bottom while the measurements were made.
- e. The model can be applied to a whole class of problems called scalar transport problems, i.e., the constituent that is being modeled can be any scalar quantity such as temperature, chemical in solution, or algae. The model can be modified easily to apply to more than one constituent including sediment particles of various settling velocities.

#### Recommendations

151. A mathematical model such as that developed in this study is a tool whose utility value is enhanced by repeated use. The model is based on sound theory but the parameters to be used must be measured or chosen with knowledge that is gained by experience with the physical processes and workings of the model. A systematic sensitivity analysis will provide a basis for selecting the proper grid, time step size, and other physical parameters. Such an analysis will also result in quantifying model response to a particular parameter - the user will know what percent error to expect in the solution for a given deviation of a particular parameter.

152. Well planned field measurement programs under diverse conditions are necessary for comparison with model simulations so that the model can be improved continually.

## REFERENCES

1. Ariathurai, Ranjan, A Finite Element Model for Sediment Transport in Estuaries, Ph.D. Thesis, Department of Civil Engineering, University of California, Davis, August 1974.
2. Ariathurai, Ranjan and Krone, Ray B., "Finite Element Model for Cohesive Sediment Transport," Journal of the Hydraulics Division, American Society of Civil Engineers, Vol. 102, No. HY3, March 1976, pp. 323-388.
3. Ariathurai, Ranjan and Krone, Ray B., "Mathematical Modeling of Sediment Transport in Estuaries," Paper presented at 3rd International Conference, Estuarine Research Federation, Galveston, Texas, October 1975.
4. Bosworth, R. C. L., "The Kinetics of Collective Sedimentation," Journal of Colloid Science, Vol. 2, 1956, pp. 496.
5. Carslaw, H. S. and Jaeger, J. C., Conduction of Heat in Solids, Clarendon Press, Oxford, 1959.
6. Christodoulou, G., Leimkuhler, W. F., and Ippen, A. T., Unpublished report on current measurements by drogues in Massachusetts Bay, Massachusetts Institute of Technology, Department of Civil Engineering, September 1973.
7. Dobbins, W. F., "Effects of Turbulence on Sedimentation," Transactions, American Society of Civil Engineers, Vol. 109, Paper No. 2218, 1944.
8. Fuchs, N. A., The Mechanics of Aerosols, Pergamon, New York, 1964.
9. Guymon, G. L., Scott, V. H., and Herrmann, L. R., "A General Numerical Solution of the Two-Dimensional Diffusion-Convection Equation by the Finite Element Method," Water Resources Research, Vol. 6, No. 6, December 1970, pp. 1611-1617.
10. Jobson, Harvey E. and Sayre, William W., "Vertical Transfer in Open Channel Flow," Journal of the Hydraulics Division, American Society of Civil Engineers, Vol. 96, No. HY3, March 1970, pp. 703-724.

11. Kandiah, A., "Fundamental Aspects of Surface Erosion of Cohesive Soils," Ph.D. Thesis, Department of Civil Engineering, University of California, Davis, 1974.
12. Krone, R. B., Flume Studies of the Transport of Sediment in Estuarial Shoaling Processes, Final Report, Hydraulic Engineering Laboratory and Sanitary Engineering Research Laboratory, University of California, Berkeley, June 1962.
13. Krone, R. B., A Study of Rheologic Properties of Estuarial Sediments, Final Report, SERL Report No. 63-8, Hydraulic Engineering Laboratory and Sanitary Engineering Laboratory, University of California, Berkeley, September 1963.
14. Krone, R. B., "A Field Study of Flocculation as a Factor in Estuarial Shoaling Processes," Technical Bulletin No. 19, Committee on Tidal Hydraulics, Corps of Engineers, June 1972.
15. Kruyt, H. R., ed., Colloid Science I, Elsevier Publishing, New York, 1952.
16. McGauhey, P. H. and Krone, R. B., "Soil Mantle as a Wastewater Treatment System," Final Report, SERL Report No. 67-11, University of California, Berkeley, December 1967.
17. Migniot, C., "A Study of the Physical Properties of Various Forms of Very Fine Sediments and Their Behaviour Under Hydrodynamic Action," La Houille Blanche, No. 7, 1968, pp. 591-620.
18. Odd, N. U. M. and Owen, M. W., "A Two Layer Model of Mud Transport in the Thames Estuary," Proceedings of the Institute of Civil Engineers, Paper 7517-S, 1972.
19. Ogata, Akio and Banks, R. B., "A Solution of the Differential Equation of Longitudinal Dispersion in Porous Media," U.S. Geological Survey, Professional Paper 411-A, 1961.
20. Owen, M. W., "A Detailed Study of the Settling Velocities of an Estuary Mud," Report No. Int. 78, Hydraulics Research Station, Wallingford, England, September 1970.

21. Partheniades, E., "A Study of Erosion and Deposition of Cohesive Soils in Salt Water," Ph.D. Dissertation, University of California, Berkeley, 1962.
22. Pierce, T. J. and Williams, D. J., "Experiments on Certain Aspects of Sedimentation of Estuarine Muds," Institution of Civil Engineers, Paper No. 6931, London, 1966.
23. Sargunam, A., Riley, P., Arulanandan, K., and Krone, R. B., "Physico-Chemical Factors in Erosion of Cohesive Soils," Technical Note No. 9609, Journal of the Hydraulics Division, American Society of Civil Engineers, Vol. 99, No. HY3, March 1973.
24. Sayre, William W., "Dispersion of Silt Particles in Open Channel Flow," Journal of the Hydraulics Division, American Society of Civil Engineers, Vol. 95, No. HY3, May 1969, pp. 1009-1038.
25. Smith, I. M., Farraday, R. V., and O'Connor, B. A., "Rayleigh-Ritz and Galerkin Finite Elements for Diffusion-Convection Problems," Water Resources Research, Vol. 9, No. 3, June 1973, pp. 593-606.
26. Smoluchowski, Von M., Ann. Physik, Vol. 21, 1906, p. 756.
27. Sauzay, G. and Allen, G., Personal Communication, "Report of Radioactive Tracer Studies, Sumatra," Report prepared for Government Offices of Sumatra, 1975.
28. Strang, Gilbert and Fix, G. J., An Analysis of the Finite Element Method, Prentice Hall, Inc., 1973.
29. Tesche, Thomas William, "Vertical Turbulent Transport in a Partially-Mixed Estuary," Ph.D. Thesis, Department of Civil Engineering, University of California, Davis, 1974.
30. Whytlaw-Gray, R., Smoke, a Study of Aerial Disperse Systems, London, 1932.
31. Zienkiewicz, O. C., The Finite Element Method in Engineering Science, McGraw-Hill, London, 1971, 521 pages.

The element coefficient and load matrices are derived in this section together with the line integrations for the flux boundary conditions and mass deposited.

The Element and Shape Functions

Quadrilateral elements with any or all sides being curved can be used. Each element is defined by eight node points numbered counter-clockwise as in Fig. A.1.

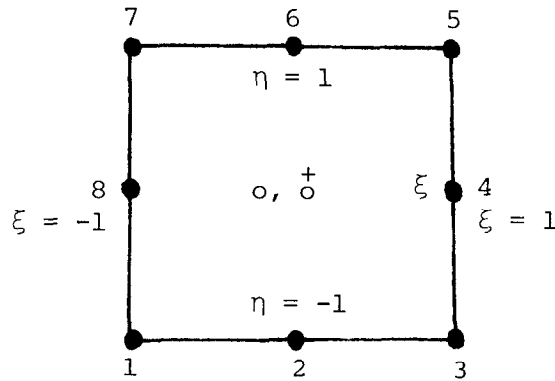


Fig. A.1. Element With Local Coordinate System

Both the approximations for the concentration and geometry of the element are quadratic, hence, the element is called isoparametric. Geometric transformation to local coordinates  $(\xi, \eta)$  would be exact for linear and parabolic sides. The shape function  $N_{\kappa}$  must be unity at node point  $\kappa$  and zero at every other node point.

There are then eight shape functions,  $N_i$  ( $i = 1, 8$ ), given in terms of the local variables  $\xi, \eta$  and the node point coordinates  $\xi_i, \eta_i$  as in Table A.1. The coordinates  $\xi_i$  and  $\eta_i$  take the values -1 and 1.

Table A.1

## Quadratic Shape Functions

Node Number	Shape Function
CORNER NODES 1, 3, 5, 7	$N_i = (1 + \xi\xi_i) (1 + \eta\eta_i) (\xi\xi_i + \eta\eta_i - 1)/4$
MIDSIDE NODES 2, 6, $\xi_i = 0$	$N_i = (1 - \xi^2) (1 + \eta\eta_i)/2$
MIDSIDE NODES 4, 8, $\eta_i = 0$	$N_i = (1 - \eta^2) (1 + \xi\xi_i)/2$

The approximation  $\hat{C}$  to the concentration within each element is written in terms of the shape functions and node point concentrations as:

$$\hat{C} = N_i C_i \quad (i = 1, 8) \quad \text{A.1}$$

In the Galerkin formulation of the governing equation, the derivatives  $\hat{C}$  with respect to the global variables  $x$  and  $z$  appear. These need to be transformed to the local unknown  $\xi$  and  $\eta$ .

The coordinate transformation from the global coordinate system  $(x, z)$  to the local  $(\xi, \eta)$  system is effected by using the same quadratic shape functions  $N_i$ . Uniqueness and continuity of mapping are discussed in Zienkiewicz\*.

---

\* Zienkiewicz, O. G., The Finite Element Method in Engineering Science, McGraw-Hill, 1971.

## Derivatives of Functions

The coordinates of any point  $(x, z)$  are

$$x = N_i x_i$$

$$z = N_i z_i \quad (i = 1, 8) \quad \text{A.2}$$

where  $(x_i, z_i)$  are the node point coordinates in the global coordinate system.

By the chain rule of partial differentiation,

$$\frac{\partial N_i}{\partial \xi} = \frac{\partial N_i}{\partial x} \cdot \frac{\partial x}{\partial \xi} + \frac{\partial N_i}{\partial z} \cdot \frac{\partial z}{\partial \xi} \quad \text{A.3}$$

$$\frac{\partial N_i}{\partial \eta} = \frac{\partial N_i}{\partial x} \cdot \frac{\partial x}{\partial \eta} + \frac{\partial N_i}{\partial z} \cdot \frac{\partial z}{\partial \eta} \quad \text{A.4}$$

or

$$\begin{bmatrix} \frac{\partial N_i}{\partial \xi} \\ \frac{\partial N_i}{\partial \eta} \end{bmatrix} = \begin{bmatrix} \frac{\partial x}{\partial \xi} & \frac{\partial z}{\partial \xi} \\ \frac{\partial x}{\partial \eta} & \frac{\partial z}{\partial \eta} \end{bmatrix} \begin{bmatrix} \frac{\partial N_i}{\partial x} \\ \frac{\partial N_i}{\partial z} \end{bmatrix} \quad \text{A.5}$$

Jacobian [J]

Then

$$\frac{\partial N_i}{\partial x} = \left\{ \frac{\partial z}{\partial \eta} \cdot \frac{\partial N_i}{\partial \xi} - \frac{\partial z}{\partial \xi} \cdot \frac{\partial N_i}{\partial \eta} \right\} / |J| \quad \text{A.6}$$

$$\frac{\partial N_i}{\partial z} = \left\{ \frac{\partial x}{\partial \xi} \cdot \frac{\partial N_i}{\partial \eta} - \frac{\partial x}{\partial \eta} \cdot \frac{\partial N_i}{\partial \xi} \right\} / |J| \quad \text{A.7}$$

The derivatives of the shape functions with respect to  $\xi$  and  $\eta$  are tabulated below.

Table A.2  
Derivatives of Shape Functions

Node Number	Differential with respect to	Derivative
CORNER NODES 1, 3, 5, 7	$\xi$	$[N_i]_{\xi} = \frac{\xi_i}{4} (1 + \eta\eta_i) (2\xi\xi_i + \eta\eta_i)$
MID-SIDE NODES 2, 6, $\xi_i = 0$	$\xi$	$[N_i]_{\xi} = -\xi (1 + \eta\eta_i)$
MID-SIDE NODES 4, 8, $\eta_i = 0$	$\xi$	$[N_i]_{\xi} = \frac{\xi_i}{2} (1 - \eta^2)$
CORNER NODES 1, 3, 5, 7	$\eta$	$[N_i]_{\eta} = \frac{\eta_i}{4} (1 + \xi\xi_i) (2\eta\eta_i + \xi\xi_i)$
MID-SIDE NODES 2, 6	$\eta$	$[N_i]_{\eta} = \frac{\eta_i}{2} (1 - \xi^2)$
MID-SIDE NODES 4, 8	$\eta$	$[N_i]_{\eta} = -\eta (1 + \xi\xi_i)$

Also,

$$[x]_{\xi} = [N_i]_{\xi} x_i \quad ; \quad [x]_{\eta} = [N_i]_{\eta} x_i$$

$$[z]_{\xi} = [N_i]_{\xi} z_i \quad ; \quad [z]_{\eta} = [N_i]_{\eta} z_i \quad \text{A.8}$$

## Coefficient Matrices

Gaussian quadrature is used to form the element coefficient matrix. This requires the evaluation of the integrand in equation 4.19 at each quadrature point, which in turn requires the evaluation of the following quantities at that point  $(\xi, \eta)$ . The approximate point velocities  $\hat{u}$  and  $\hat{w}$  are given by

$$\hat{u} = N_{\alpha} u_{\alpha} \quad (\alpha = 1, 8) \quad \text{A.9}$$

$$\hat{w} = N_{\alpha} w_{\alpha} \quad (\alpha = 1, 8) \quad \text{A.10}$$

The set

$$[x]_{\xi} = [N_{\alpha}]_{\xi} x_{\alpha} \quad \text{etc.} \quad (\alpha = 1, 8) \quad \text{A.11}$$

and

$$|J| = [x]_{\xi} [z]_{\eta} - [x]_{\eta} [z]_{\xi} \quad \text{A.12}$$

Then

$$\frac{\partial N_j}{\partial x} \equiv [N_j]_x = \left\{ [z]_{\eta} [N_j]_{\xi} - [z]_{\xi} [N_j]_{\eta} \right\} / |J| \quad \text{A.13}$$

$$\frac{\partial N_j}{\partial x} \equiv [N_j]_z = \left\{ [x]_{\xi} [N_j]_{\eta} - [x]_{\eta} [N_j]_{\xi} \right\} / |J| \quad \text{A.14}$$

$$(j = 1, 8)$$

From equations 4.19 and 4.20, the element coefficient matrix  $[K]$  times the array of node point concentrations  $\{C\}$  is given by

$$\begin{aligned}
[K] \{C\} = & \iint_{D_{ne}} \left[ N_i \left\{ u \frac{\partial \hat{C}}{\partial x} + w \frac{\partial \hat{C}}{\partial z} - \alpha_1 \hat{C} \right\} + \frac{\partial N_i}{\partial x} D_x \frac{\partial \hat{C}}{\partial x} \right. \\
& \left. + \frac{\partial N_i}{\partial z} D_z \frac{\partial \hat{C}}{\partial z} \right] dx dz
\end{aligned} \tag{A.15}$$

Now

$$\iint dx dz = \iint |J| d\xi d\eta \tag{A.16}$$

Then the (i, j) term of the element coefficient matrix is

$$\begin{aligned}
K_{ij} = & \iint_{D_{ne}} \left[ N_i \left\{ (N_{\alpha} u_{\alpha}) [N_j]_x + (N_{\alpha} w_{\alpha}) [N_j]_z - \alpha_1 N_j \right\} \right. \\
& \left. + \left\{ D_x [N_i]_x [N_j]_x + D_z [N_i]_z [N_j]_z \right\} \right] |J| d\xi d\eta \\
& ((\alpha = 1, 8), \quad j = 1, 8), \quad i = 1, 8)
\end{aligned} \tag{A.17}$$

where  $[N]_x = \partial N / \partial x$ , etc.

The coefficient array [T] of the time rate of change of the node point concentrations  $\frac{\partial C_j}{\partial t}$  is given by

$$\begin{aligned}
T_{ij} = & \iint_{D_{ne}} N_i N_j |J| \partial \xi \partial \eta \\
& ((\alpha = 1, 8) \quad j = 1, 8) \quad i = 1, 8)
\end{aligned} \tag{A.18}$$

The load matrix

$$\{F\} = - \iint_{D_{ne}} [N]^T \{\alpha_2\} dx dy + \int_{\ell} [N]^T \{q^S\} d\ell \quad A.19$$

where  $\ell$  = boundary of element, and  $\{q^S\}$  is the flux source term.

The first term of  $F$

$$\iint_{D_{ne}} [N]^T \{\alpha_2\} dx dy = \iint_{D_{ne}} N_i N_j \alpha_2 |J| d\xi d\eta \quad A.20$$

The integration of the second term is described in the next section.

Each term in the relationships for the various arrays is integrated numerically using the Gauss-Legendre scheme, i.e.,

$$\iint_{-1-1}^{1 1} f(\xi, \eta) d\xi d\eta = \sum_{m=1}^n \sum_{k=1}^n H_m H_k f(\xi_k, \eta_m) \quad A.21$$

for  $n$  quadrature points where  $H$  represents the weight coefficients.

### Contour Integral of Flux

Where the flux  $q^S$  is specified at a boundary such as the bed the quantity

$$\int_{\ell} [N]^T \{q^S\} d\ell$$

needs to be evaluated.

Considering one side of an element at a time, the quadratic shape functions  $M$  can be written in terms of the local contour coordinate  $s$  as,

$$M_1 = s (s - 1)/2$$

$$M_2 = (s + 1) (1 - s) \quad \text{A.22}$$

$$M_3 = s (s + 1)/2$$

where  $-1 \leq s \leq 1$ .

Then the approximation to the flux

$$\hat{q} = M_i q_i \quad i = 1, 3 \quad \text{A.23}$$

where  $q_i$  represents the node point values of the flux for the three nodes that are on the side of the element being integrated. Now

$$d\ell = \sqrt{dx^2 + dy^2} \quad \text{A.24}$$

and

$$dx = \left( \frac{dM_i}{ds} x_i \right) ds$$

$$dy = \left( \frac{dM_i}{ds} y_i \right) ds \quad \text{A.25}$$

The two dimensional shape functions  $N$  evaluated on the element boundary are identical to  $M$ .

Therefore,

$$\int_{\ell} [N^T] \{q^S\} d\ell = \int_{-1}^1 M_i (M_j q_j) A ds \quad \text{A.26}$$

((j = 1, 3), i = 1, 3)

where

$$A = \sqrt{\frac{dM_\alpha}{ds} x_\alpha + \frac{dM_\beta}{ds} y_\beta} \quad \text{B.27}$$

$$\alpha, \beta = 1, 3$$

Gauss-Legendre' quadrature is used to evaluate the fluxes along the boundaries.

#### Computation of Net Mass Flux to the Bed

The net mass  $D_m$  deposited per unit width of bed is given by

$$D_m = \frac{V_s}{\tau_{cd}} \int_0^L \int_0^{\Delta t} (\tau_{cd} - \tau_b) C_b dt dl \quad \text{A.28}$$

where the integrand is zero if  $\tau_b > \tau_{cd}$ ;  $L$  = length of the element boundary with the bed;  $V_s$  = settling velocity of sediment;  $\tau_b$  = shear stress at the bed; and  $C_b$  = concentration of suspended sediment near the bed.

If the shear stress and concentration at the bed are assumed to vary linearly with time,

$$D_m = \frac{V_s t}{6\tau_c} \int_0^L \left\{ (3\tau_{cd} - 2\tau_b^n - \tau_b^{n+1}) C_b^n + (3\tau_{cd} - \tau_b^n - 2\tau_b^{n+1}) C_b^{n+1} \right\} dl \quad \text{A.29}$$

where  $\tau_b^n$  is the bed shear at time step  $n$ , etc.

Assuming a quadratic variation of shear and concentration along the boundary,

$$\hat{\tau}_b = M_i (\tau_b)_i$$

$$\hat{C}_b = M_i (C_b)_i$$

A.30

$$i = 1, 3$$

The integrand in equation A.29 is evaluated as described in previous section to compute the net mass flux to the bed due to deposition, in time  $\Delta t$ .

When  $\tau_b > \tau_{ce}$  (critical shear stress for erosion), any material on the bed will be eroded as described in Part IV of the main text.

## APPENDIX B: FLOW SIMULATION

The velocities and salinity calculations were made by application of an existing finite element hydrodynamic model (independent of the effects of suspended sediment) and used the observations at stations 109 + 667 and 130 + 500 as upstream and downstream boundary conditions, respectively. The output from the hydrodynamics model was used as input to the sediment model for the purposes of model calibration and validation.

### Technical Approach

The velocity and salinity modeling was done with a modified version of an existing finite element hydrodynamics model\*. This model provides a continuous two-dimensional description of velocities and salinities in the vertical, X-Z plane. The model allows for a free surface (zero pressure) condition at the air-water interface and surface tractions at the mud-water interface. The equations used in this study are two-dimensional versions of the turbulent analogies to the three-dimensional Navier-Stokes Momentum Equations, the continuity equation and the convection-diffusion equation.

If the flow is assumed to be incompressible and if the surface conditions are ignored, the governing differential equations may be written as:

---

\* King, Ian P., William R. Norton, and Gerald T. Orlob, A Finite Element Solution for Two-Dimensional Density Stratified Flow, U.S. Department of the Interior, Office of Water Resources Research, April 1973, 80 p.

Norton, William R., Ian P. King and Gerald T. Orlob, A Finite Element Model for Lower Granite Reservoir, Walla Walla District, U.S. Army Corps of Engineers, Walla Walla, Washington, March 1973, 138 p.

Finite Elements in Fluids, Vol. 1, "Viscous Flow and Hydrodynamics" Ed. R. H. Gallagher, J. T. Oden, C. Taylor, and O. C. Zienkiewicz, John Wiley & Sons, Ltd., 1975, 279 p.

### Momentum equations

$$\begin{aligned} a\rho \left( \frac{\partial u}{\partial t} + u \frac{\partial u}{\partial x} + w \frac{\partial u}{\partial z} \right) + \frac{\partial}{\partial x} ( Pa ) - \epsilon_{xx} \frac{\partial}{\partial x} \left( a \frac{\partial u}{\partial x} \right) \\ - \epsilon_{xz} \frac{\partial}{\partial z} \left( a \frac{\partial u}{\partial x} \right) = 0 \end{aligned} \quad (B.1)$$

$$\begin{aligned} a\rho \left( \frac{\partial w}{\partial t} + u \frac{\partial w}{\partial x} + w \frac{\partial w}{\partial z} \right) + \frac{\partial}{\partial x} ( Pa ) - a\rho g - \epsilon_{zx} \frac{\partial}{\partial x} \left( a \frac{\partial w}{\partial x} \right) \\ - \epsilon_{zz} \frac{\partial}{\partial z} \left( a \frac{\partial w}{\partial z} \right) = 0 \end{aligned} \quad (B.2)$$

### Continuity equation

$$\frac{\partial}{\partial x} ( au ) + \frac{\partial}{\partial z} ( aw ) = 0 \quad (B.3)$$

### Convection-diffusion equation for density

$$\frac{\partial \rho}{\partial t} + a \left( u \frac{\partial \rho}{\partial x} + w \frac{\partial \rho}{\partial z} \right) - D_x \frac{\partial}{\partial x} \left( a \frac{\partial \rho}{\partial x} \right) - D_z \frac{\partial}{\partial z} \left( a \frac{\partial \rho}{\partial z} \right) = 0 \quad (B.4)$$

where

$u, w$  = velocity components in X and Z directions

$\rho$  = fluid density

$P$  = fluid pressure

$\epsilon_{xx}, \epsilon_{xz}, \epsilon_{zx}, \epsilon_{zz}$  = turbulent exchange coefficients

$D_x, D_z$  = turbulent diffusion coefficients

$a$  = lateral width

In accordance with conventional fluid mechanics the extension of these essentially laminar equations has been achieved by replacing the molecular viscosity and diffusion coefficients by their turbulent counterparts. These coefficients are, of course, dependent upon the

flow regime and their values were determined by a trial and error process from the observed data for the neap tide.

Using the techniques of the finite element method, the above equations have been coded for solution by a digital computer. The resulting computer model incorporates both triangular and quadrilateral isoparametric elements, with velocities allowed to vary quadratically and the pressures linearly.

The model has been developed in FORTRAN-IV programming code on the UNIVAC 1108 computer with 65,000 words of storage. A version of the model has been used on the CDC 7600 for a very large problem with about 150,000 words of storage. An in-core equation solver has been used throughout to reduce run times on the iterations required at each time step. The equations are unsymmetrical, and this approximately doubles computer storage requirements and quadruples solution time over similar problems with symmetrical equations. The solution routine uses a dynamically allocated storage algorithm with a pseudo-rectangular form in which the diagonal term is located to minimize the storage actually used. One other feature of the model allows the user to, at his option, control the order of the solution process. For dynamic problems the solution is integrated in time with a two-point, finite difference scheme. The output from the model consists of tabular values of velocity (u and w), pressure, density, salinity, and location of the water surface at all network node points at each point in time.

## Model Application

### Introduction

The flow simulations were completed by a straightforward application of the existing hydrodynamics model. The only change made to the model was a slight modification in the eddy viscosity terms of the momentum equations to allow the diagonal and off-diagonal terms (e.g.,  $\epsilon_{xx}, \epsilon_{xz}$ ) to assume independent values. This change resulted in the calculation of improved velocity profiles at all locations in the

estuary, and is consistent with the mixing length approach to eddy viscosity.

Successful application of the flow model requires that a number of semi-independent, but interrelated, items be considered. Chief among these are the physical description of the system, its overall water balance, definition of proper boundary conditions, and reasonable estimates of the eddy viscosity and eddy diffusion coefficients. A summary of the methods and techniques used for each item is presented below, together with representative comparisons of the output produced by the computer program and corresponding field measurements. The conditions and data associated with the spring tide are used exclusively for discussion purposes; observations for the neap and mean tides are similar in content and generally show behavior parallel to the spring values.

#### Physical description of the Savannah Estuary

In all cases, existing Corps data\* were used to estimate the physical configuration of the Savannah Estuary. Figure B.1 shows a plan view of the general area, with the velocity and salinity sampling stations denoted as small circles (numbers 1, 2, and 3). The region of interest was estimated to be 20,833 feet long and to have a rectangular cross section with a width of 650 feet.

The estimate of top width was made from aerial photographs; for reference purposes, cross sections (approximate) from field soundings at the three sampling locations are shown in Fig. B.2. The cross section at station 125 + 500 is not representative of the overall system as it is located at a turning basin.

---

\* Krone, R. B., "A Field Study of Flocculation as a Factor in Estuarial Shoaling Processes," Tech. Bull. No. 19, Corps of Engineers, U.S. Army, June 1972, 62 p. plus Appendices.

Krone, R. B., "A Field Study of Flocculation as a Factor in Estuarial Shoaling Processes, Appendix D: Velocities, Salinities, and Suspended Solids from Field Measurements and Samples," Tech. Bull. No. 19, Corps of Engineers, U.S. Army, June 1972, 61 p.

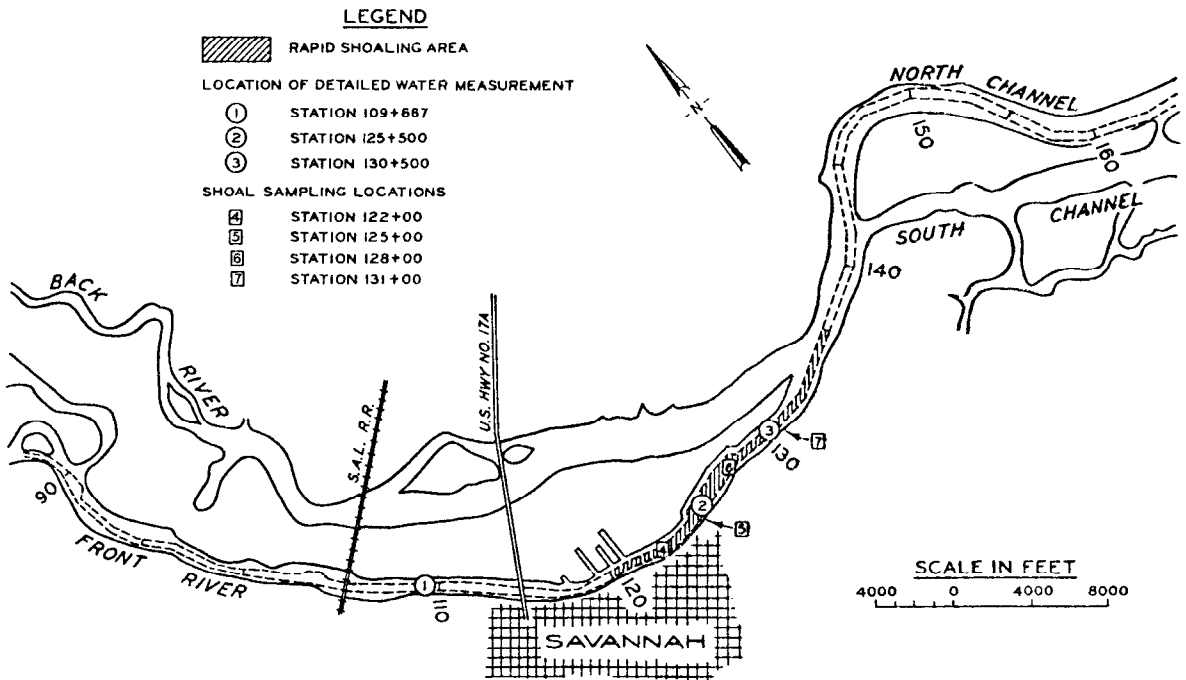


Fig. B.1. Locations of Water Measurement and Shoal Sampling Stations

Defining the elevation of the estuary's bottom presented a difficult problem. The constant deposition and scour which takes place moves the effective bottom up and down during a tidal cycle, perhaps as much as 4 feet. At the outset of the modeling work, this fact was recognized, but its influence was not expected to be large, and modifying the hydrodynamics model to accept a movable bottom was beyond the scope of the project. With this in mind, and using a sounding chart constructed from approximately eight field surveys spanning the summer of 1968, a bottom profile was estimated which ranged in elevation from a low of -40 feet at station 127 + 000 to a high of -32.5 at station 115 + 500. For reasons explained in the discussion, this configuration proved unsatisfactory and a revised estimate of bottom position was adopted. For all simulations reported herein the bottom elevation was set at a constant value of -35.0 feet.

The finite element network used to represent the final configuration is graphically depicted in Fig. B.3. This network was comprised of 49 quadrilateral elements with 176 node points. As can

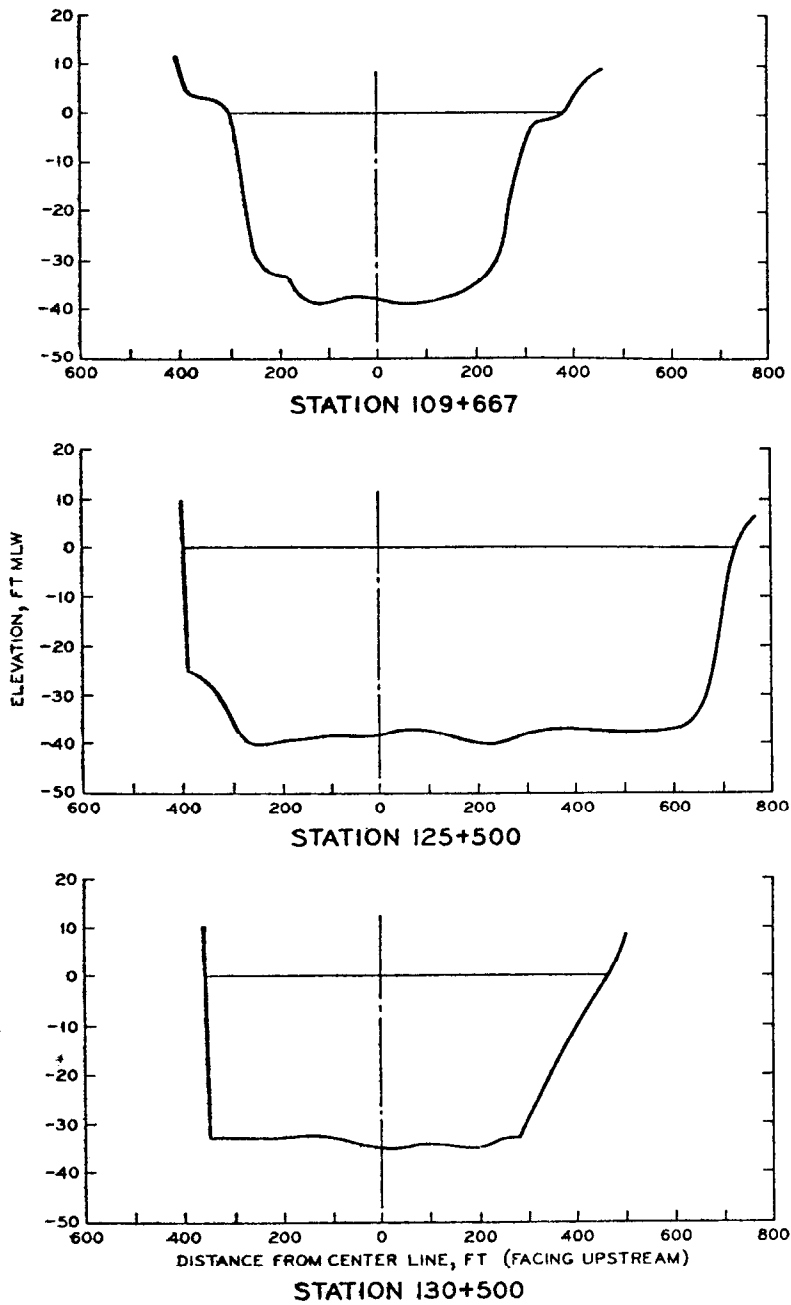


Fig. B.2. Midtide Cross Sections at the Sampling Stations

be seen in the figure, the network has relatively more detail near the bottom than near the free water surface. This construction is motivated by a desire to have a detailed description of the velocity profiles near the bed in order that shear stresses can be computed accurately for sediment calculation.

The network shown in Fig. B.3 indicates the upper boundary (free water surface) at elevation zero. During the simulations this boundary was allowed to move in accordance with the tidal behavior to maintain the zero surface pressure boundary condition; all other points in the system maintained their geometrical position during the simulations.

#### Water balance

Data observed in the Savannah Estuary included current speed, current direction, and water surface position. With a knowledge of the cross section and top width it is possible to calculate a water balance over time. From a modeling point of view, it is important that overall system continuity be maintained in the specification of boundary conditions or an inconsistent problem solution will result.

The water balance for the Savannah Estuary was calculated as follows. First, the geometric description outlined above was assumed to hold. Next, the observed elevation of the water surface (supplied by the Corps) was taken to be accurate. The difference in observed tidal elevations at the upper and lower ends of the estuary was very small; the water surface over the test section could therefore be treated as a horizontal plane.

The observed velocity profiles and storage changes were then integrated in time and space to compute the system water balance; the results of this exercise are summarized in Table B.1. Columns 3, 4, and 5 are the estimated flows at stations 1, 2, and 3 based on a vertical integration of the current speed and direction observations. Columns 6 and 7 show the net inflow/outflow in the estuary, first between stations 109 + 667 and 130 + 500 and then between stations 125 + 500 and 130 + 500. The final two columns indicate the rate of change of volume between stations 109 + 667

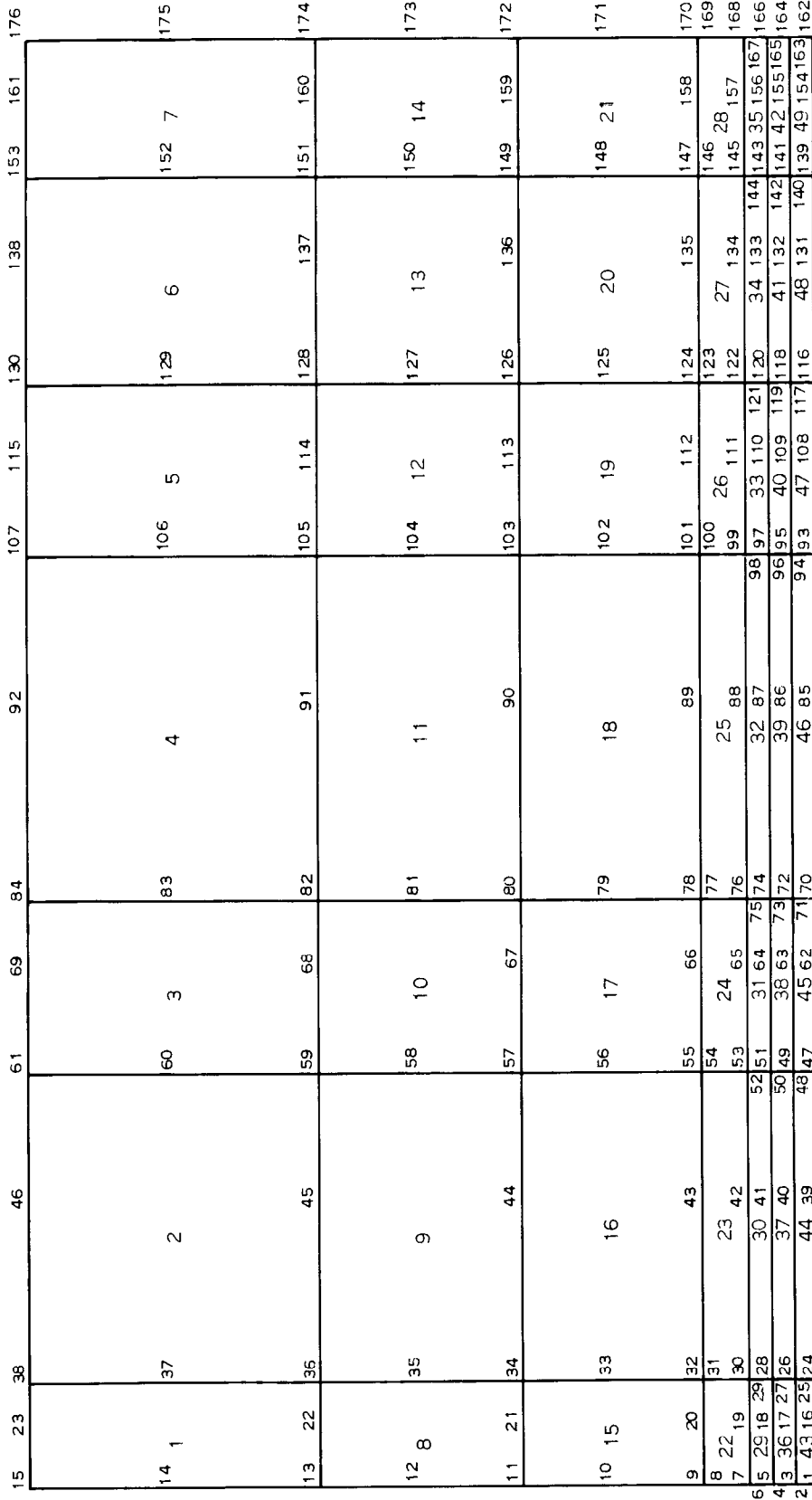


Fig. B.3. Finite Element Network used for Flow Simulation in the Savannah Estuary Between Stations 109+667 and 130+500

Table B.1

Net Flows and Rate of Change of Volume Between Stations 109+667  
and 130+500 in the Savannah Estuary, Sept. 24-25, 1968

Time* (Hours)	Water Surface (Feet)	Net Flow** Sta. 109 + 667 (cfs)	Net Flow Sta. 125 + 500 (cfs)	Net Flow Sta. 130 + 500 (cfs)	Net Flow Between Stations 109 + 667 and 130 + 500 (cfs)	Net Flow Between Stations 125 + 500 and 130 + 500 (cfs)	Rate of Change of Volume Between Station 109 + 667 and Station 130 + 500 (cfs)	Rate of Change of Volume Between Station 109 + 667 and Station 125 + 500 (cfs)
1530	1.70	57364	-	644	56720	-644	-6067	-1444
1600	0.90	53690	45403	48380	5309	-2977	-6067	-1443
1630	0.40	46941	30647	31495	15446	-848	-3792	-903
1700	0.55	33948	13611	3779	30169	9832	1138	271
1730	1.55	5121	-9601	-5583	10707	-4018	7583	1806
1800	1.70	-23516	-25365	-151	-23365	-25213	1138	271
1830	4.15	-48079	-40527	--	-48079	-40527	18579	4424
1900	5.30	-60679	-47391	-72183	11503	24792	8721	2076
1930	6.60	-65448	-40864	-67753	2106	26889	9858	2347
2000	7.60	-73092	-44471	-63794	-9298	19323	7583	1805
2030	8.30	-74175	-37249	-57077	-17097	19828	5308	1264
2100	8.75	-61963	-52519	-52273	-9690	-246	3413	812
2130	9.00	-45186	-37313	-44395	-791	7082	1896	451
2200	9.05	-46547	-31085	-35319	-11227	4235	379	90
2230	8.95	-28806	-22036	-19560	-9246	-2476	-758	-181
2300	8.70	-6166	-3762	1309	-7475	-5071	-1896	-451
2330	8.20	23208	14708	24936	-1727	-10228	-3791	-902
2400	7.45	47527	41068	48683	-156	-7614	-5688	-1354
0030	6.70	72330	60982	75066	-2735	-14084	-5688	-1354
0100	5.80	77840	82181	87848	-10007	-5667	-6825	-1625
0130	4.70	75576	78814	86455	-10878	-7641	-8342	-1986
0200	3.75	64292	75509	80307	-16015	-4798	-7204	-1715
0230	2.90	65017	65679	70248	-5231	-4569	-6446	-1535
0300	2.00	61712	54386	72055	-10342	-17668	-6825	-1625
0330	1.25	52781	50645	60178	-7397	-9533	-5688	-1354
0400	0.65	50442	36933	50934	-491	-14000	-4550	-1083
0430	0.30	37053	27389	35094	1959	-7705	-2654	-632
0500	0.45	21022	10992	12529	8493	-1536	1138	271
0530	1.00	-842	-7964	-10088	9246	2124	4170	993

\*Beginning Sept. 24, 1968

\*\*Ebb is positive

and 130 + 500 as calculated from the change of water surface.

If there was absolute consistency between the velocity (net flow) and water surface observations, a simple water balance could be written as

$$Q_I - Q_O = \frac{\Delta v}{\Delta t} \quad (\text{B.5})$$

where

$Q_I$  = the observed inflow to the test reach, cfs

$Q_O$  = the observed outflow from the test reach, cfs

$\frac{\Delta v}{\Delta t}$  = the observed rate of volume change in the reach, cfs

In order to prepare a consistent water balance, it was assumed that the rate of change of volume within the test section was a relatively accurate calculation, and that any inconsistencies could be attributed to velocity measurements. Also, the observations at station 130 + 500 were judged to have the highest likelihood of consistency of the three velocity measurements. Under these assumptions, equation B.5 was modified to the form

$$RQ_I - Q_O = \frac{\Delta v}{\Delta t} \quad (\text{B.6})$$

or

$$R = \left( \frac{\Delta v}{\Delta t} + Q_O \right) / Q_I \quad (\text{B.7})$$

where

R = a correction factor to be applied to the observed velocities at stations 109 + 667 and 125 + 500 to achieve an exact system water balance. If all the observations are consistent R = 1.0

Equation B.7 was solved for each time step; the results from the spring tide are presented in Table B.2. In general these values

Table B.2

Velocity Correction Factors for an Exact Water Balance,  
Savannah Estuary, Sept. 24-25, 1968

Time Hours	Correction Factor R @ Station 109 + 667	Correction Factor R @ Station 125 + 500
1530	-0.09	--
1600	0.79	1.03
1630	0.59	1.00
1700	0.14	0.30
1730	0.39	0.39
1800	-0.04	-0.01
1830	-0.39	-0.11
1900	1.05	1.48
1930	0.88	1.60
2000	0.77	1.39
2030	0.70	1.50
2100	0.79	0.98
2130	0.94	1.18
2200	0.75	1.13
2230	0.71	0.90
2300	0.10	-0.23
2330	0.91	1.63
2400	0.89	1.15
0030	0.96	1.21
0100	1.04	1.05
0130	1.03	1.07
0200	1.14	1.04
0230	0.98	1.05
0300	1.06	1.29
0330	1.03	1.16
0400	0.92	1.35
0430	0.88	1.26
0500	0.65	1.16
0530	7.03	1.14

are about what would be expected from this type of calculation, with the majority of the observed flow profiles meeting continuity within  $\pm 15\%$ . The largest percentage errors can also be seen to occur at times of low velocity, a period at which the time to make the observations and relatively large turbulent eddies may influence the

results. In the discussions which follow, the correction factor R has been applied to observed velocities for the sake of consistency.

### Model calibration

The momentum and convection-diffusion equations for the hydrodynamic model contain certain semiempirical coefficients called eddy viscosity and eddy diffusion coefficients. Proper model operation is contingent on reasonable estimates of these values, and a substantial amount of this work was devoted to a definition of these values. A number of spatial and temporal schemes were proposed and evaluated with the data from the neap tide. Several different forms of the turbulence analogy were attempted and their behavior compared to field observations. None of the proposed schemes were found to provide consistently better or more accurate results than simple eddy viscosity relationships indicated in equations B.1 and B.2, and constant values were adopted for all computer runs. It should be pointed out that at most times in the Savannah Estuary the flow field is dominated by inertial effects; therefore, the model's output is somewhat insensitive to the eddy viscosity values.

The values selected were:

$$\begin{aligned}\epsilon_{xx} &= 5 \times 10^3 \text{ lb-sec/ft}^2 \text{ at all locations} \\ \epsilon_{xz} = \epsilon_{zx} &= 1 \times 10^{-4} \text{ lb-sec/ft}^2 \text{ at all locations} \\ \epsilon_{zz} &= 5 \times 10^2 \text{ lb-sec/ft}^2 \text{ at all locations} \\ D_x &= 5 \times 10^2 \text{ ft}^2/\text{sec at all locations} \\ D_y &= 1 \times 10^1 \text{ ft}^2/\text{sec from elevations -35.0 to -30.0 and} \\ &5 \times 10^{-4} \text{ ft}^2/\text{sec elsewhere}\end{aligned}$$

### Model results

The model was operated on the Savannah Estuary for the periods indicated. Time steps of 30 minutes were specified, and the complete dynamic behavior of the system calculated at each node point at each time step. The output from the model consisted of velocities, pressures, densities, and salinities; this data was punched into cards for subsequent use by the sediment model.

As an indication of the shape and magnitude of simulated and observed velocity profiles, Fig. B.4 presents model/prototype comparisons at four times spanning a period of tidal reversal. Each of the plots represents the behavior at station 125 + 500, with the solid line indicating the simulated values and the plotted points the observed values.

### Discussion

The modeling results produced in the course of this work are in reasonable agreement with the limited field observations and are thought to be adequate for input to the sediment model. The major problem encountered in this effort, and one which was never really resolved, was the proper location of the movable bottom. As was pointed out earlier, the first network constructed for the estuary was configured with a depression in the area of station 125 + 500. The results produced by the model with this network were judged quite satisfactory when compared to field observations at all points except very near the bed, where lower than observed velocities were calculated. No amount of coefficient adjustment, within the range of reasonable values, could rectify this situation, and flow simply passed over the bottom depression.

Not surprisingly, as the bottom depression was removed by network adjustment, the velocities near the bed increased. It soon became evident that near-bed flows were highly influenced by the location of the bottom, while velocities higher in the water column were relatively unaffected. Primarily due to the lack of more precise data, it was finally decided to perform the simulations with a flat bed at a fixed, average elevation. The results from such an approach are shown in Fig. B.4, and display the expected characteristics--higher than observed near-bed velocities.

The ultimate solution to this problem is conceptually simple, but technically difficult; the sediment and hydrodynamic solutions should be coupled for simultaneous solution. The preparation of such

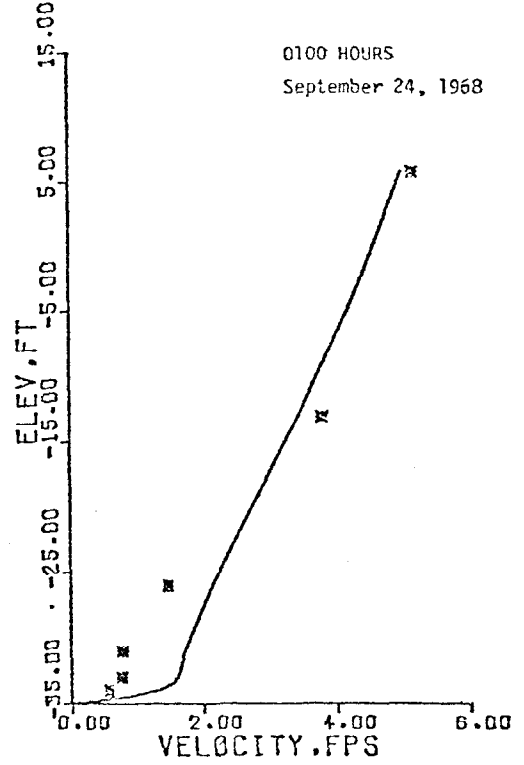
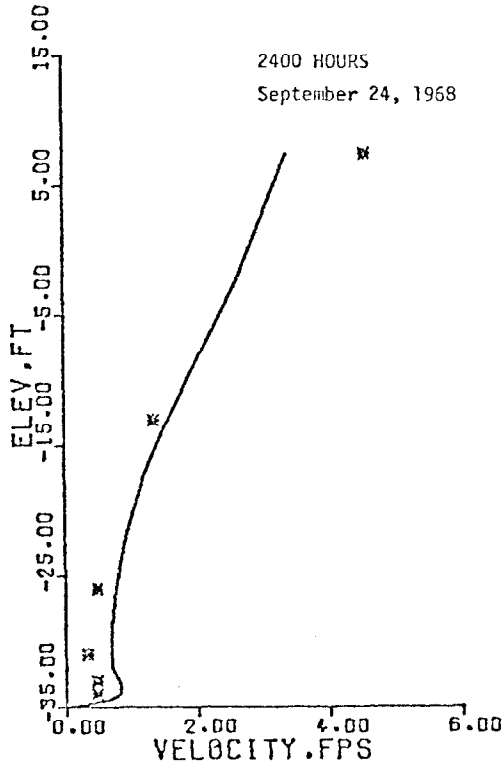
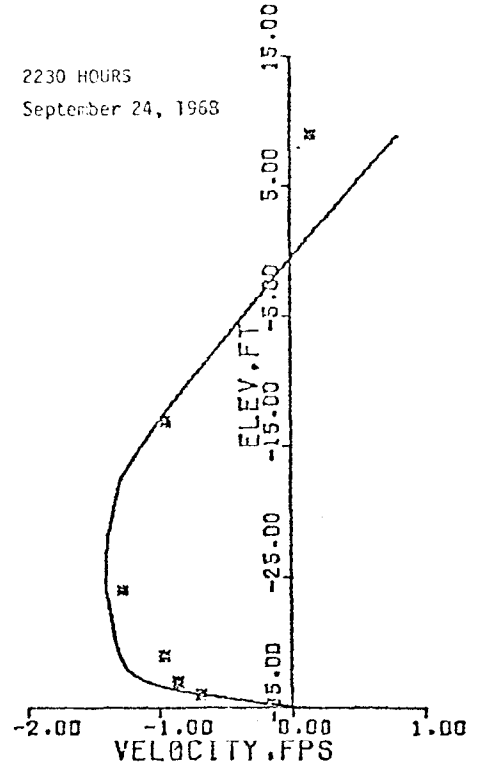
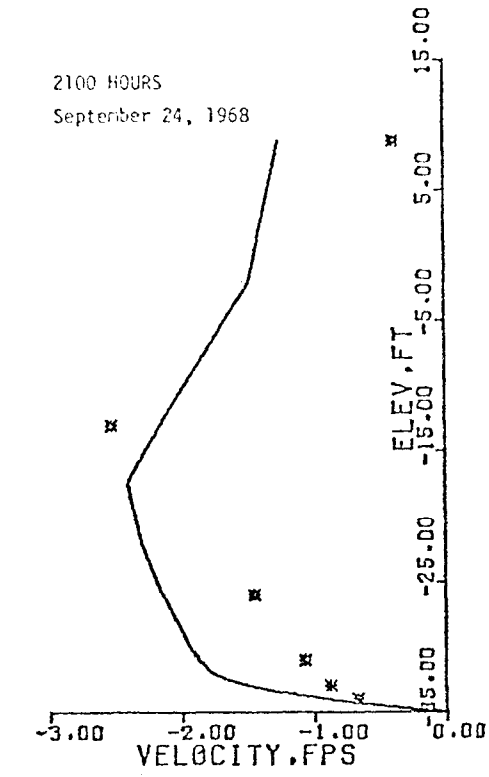


Fig. B.4. Comparison Between Simulated and Observed Velocities at Station 125+500 in the Savannah Estuary

a model awaits further development, with the approach demonstrated by this project representing a workable alternative until that final step is taken.

Theory

The underlying theory for the grid generator is discussed below.

Generalized equations

Consider a typical nonrectangular grid shown in Fig. C.1. Location of an interior node  $i$  can be computed in terms of its neighboring nodes ( $n_j, n_k, n_\ell, \dots$ ) by the following equations:

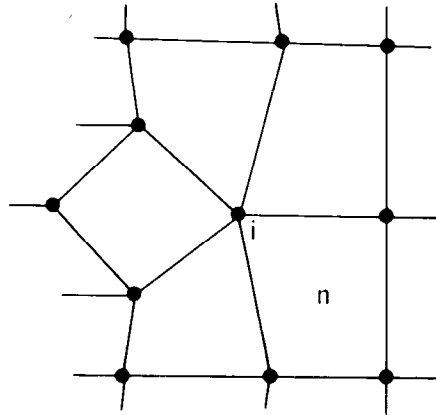
$$x_i = \frac{1}{N_i(2-w)} \sum_{n=1}^{N_i} (x_{n_j} + x_{n_\ell} - w x_{n_k}) \quad (C.1)$$

$$0 \leq w \leq 1$$

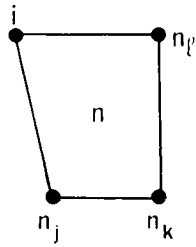
$$i = 1 \rightarrow I$$

$$y_i = \frac{1}{N_i(2-w)} \sum_{n=1}^{N_i} (y_{n_j} + y_{n_\ell} - w y_{n_k}) \quad (C.2)$$

where  $N_i$  denotes the number of elements containing node  $i$ . The value of the weighting coefficient  $w$  determines the type of generation scheme employed. If  $w = 1$ , the equations above will yield an isoparametric generation scheme. Setting  $w = 0$  produces a Laplacian scheme. Values of  $w$  between 0 and 1 will result in a mixed generating scheme which is biased towards either an isoparametric or Laplacian method depending on the exact value of  $w$ . Coordinate computation for the  $i$ -th node is usually done by iteration. An iterative method of the Gauss-Seidel type was employed in this program because of desirable convergence characteristics. For the application to nonrectangular type grids the coding is slightly more complex for the Gauss-Seidel scheme, but the storage requirements and the execution time per iteration cycle are essentially the same. For



PORTION OF A NON-RECTANGULAR GRID



DETAILED VIEW OF ELEMENT "n"

Fig. C.1. Neighborhood of Node "i" Non-Rectangular Grid

a particular example (shown later as Fig. C.6) a comparison of the number of iterations required for various values of  $w$  is given in Fig. C.2; the rapid increase in the number of iterations as  $w \rightarrow 1.0$  is to be noted.

The rate of convergence can be substantially improved by using an over-relaxation factor  $R$  (the improved estimate for the  $n$ -th iteration is denoted by  $x_i^{(n)*}$ ), i.e.,

$$x_i^{(n)*} = x_i^{(n-1)} + R(x_i^{(n)} - x_i^{(n-1)}), \text{ etc.}$$

It was found desirable to use a value of  $R$  in the neighborhood of 1.3 (for the second example given in the next section, a value of 1.3 yielded approximately a 40% reduction in the required number of iteration cycles).

#### Laplacian scheme

If  $w$  is equal to zero, equations C.1 and C.2 reduce to

$$x_i = \frac{1}{2N_i} \sum_{n=1}^{N_i} (x_{n_j} + x_{n_\ell}) \quad (C.3)$$

$i = 1 \rightarrow I$

$$y_i = \frac{1}{2N_i} \sum_{n=1}^{N_i} (y_{n_j} + y_{n_\ell}) \quad (C.4)$$

Application of the above equations to obtain coordinates of the  $i$ -th node as shown in Fig. C.3 yields

$$x_i = \frac{1}{4} (x_{i_1} + x_{i_2} + x_{i_3} + x_{i_4}) \quad (C.5)$$

$i = 1 \rightarrow I$

$$y_i = \frac{1}{4} (y_{i_1} + y_{i_2} + y_{i_3} + y_{i_4}) \quad (C.6)$$

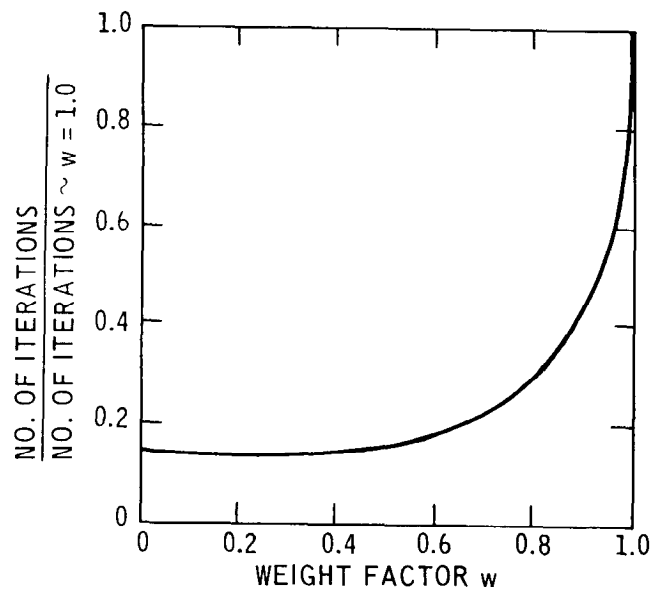


Fig. C.2. Number of Iterations Required for Convergence as a Function of  $w$

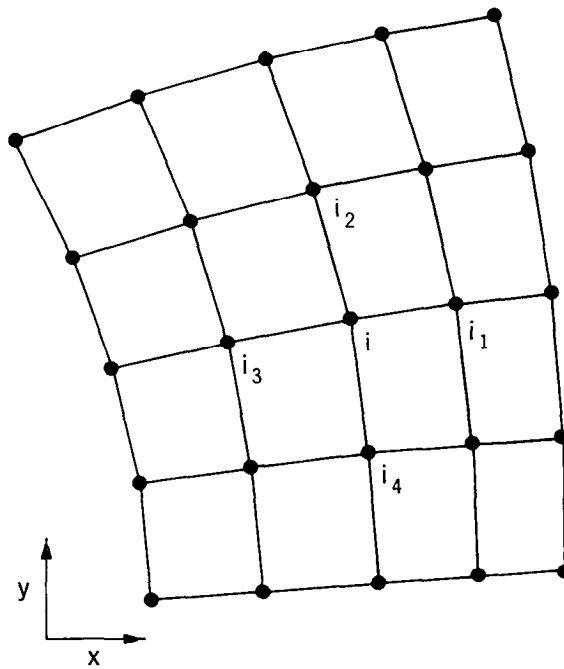


Fig. C.3. Neighborhood of Node "i"

This scheme is very simple to apply; however, it suffers from a serious drawback. It has a tendency to distort interior elements and, in the case of complicated shapes, coordinates of interior nodes can even be established outside of the body producing erroneous results.

Alternative methods such as the isoparametric scheme were developed specifically to avoid such problems. Theoretical development of the isoparametric method is given in the following section.

### Isoparametric scheme

The following equations apply to an isoparametric scheme ( $w = 1$ ):

$$x_i = \frac{1}{N_i} \sum_{n=1}^{N_i} (x_{n_j} + x_{n_\ell} - x_{n_k}) \quad (C.7)$$

$$y_i = \frac{1}{N_i} \sum_{n=1}^{N_i} (y_{n_j} + y_{n_\ell} - y_{n_k}) \quad (C.8)$$

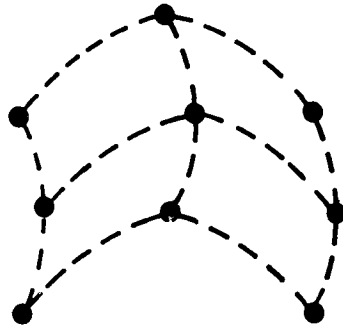
For the grid shown in Fig. C.4 the above equations can be reduced to:

$$x_i = \frac{1}{4} [2(x_{i_1} + x_{i_2} + x_{i_3} + x_{i_4}) - (x_{i_5} + x_{i_6} + x_{i_7} + x_{i_8})] \quad (C.9)$$

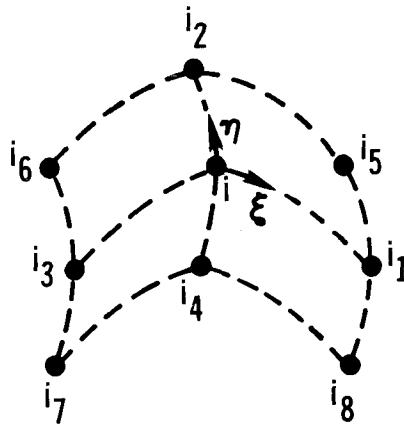
$$i = 1 \rightarrow I$$

$$y_i = \frac{1}{4} [2(y_{i_1} + y_{i_2} + y_{i_3} + y_{i_4}) - (y_{i_5} + y_{i_6} + y_{i_7} + y_{i_8})] \quad (C.10)$$

These expressions can be written in terms of a second order isoparametric transform. For an element defined by eight external nodes and quadratic shape functions  $N(\xi, \eta)$  the transformation between  $x, y$  and  $\xi, \eta$  coordinate systems, where the origin of  $\xi, \eta$  coordinates coincides with node  $i$ , may be written in the form



C.4a. SKETCH OF A GRID



C.4b. ISOPARAMETRIC REPRESENTATION OF GRID

Fig. C.4. Isoparametric Transformation of Neighborhood of Node "i"

$$x_i = x(\xi = 0, \eta = 0) = \sum_{m=1}^8 x_{i_m} N_m(\xi = 0, \eta = 0) \quad (C.11)$$

$$y_i = y(\xi = 0, \eta = 0) = \sum_{m=1}^8 y_{i_m} N_m(\xi = 0, \eta = 0) \quad (C.12)$$

Upon expansion the above expressions will be identical with equations C.9 and C.10.

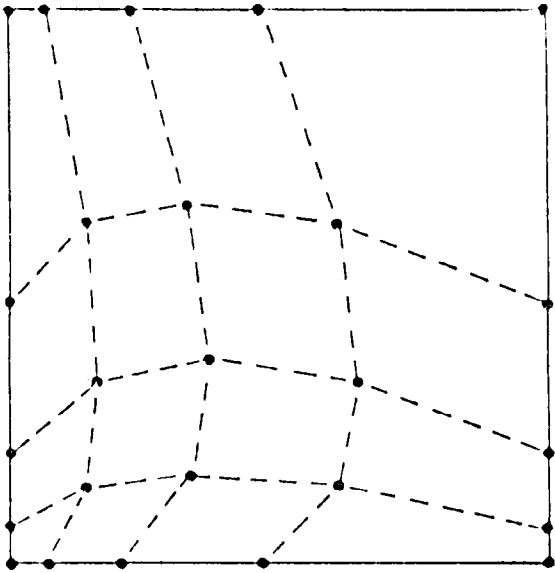
### Illustrative examples

Two relatively simple examples of grids generated by the isoparametric procedure, the Laplacian procedure, and (for the first example) an intermediate procedure are shown in Figs. C.5 and C.6 to illustrate the effects of boundary node spacing and boundary curvature, respectively. The exterior nodes were defined by specifying the coordinates of the nodes lying on the ends of the straight or circular boundary segments; these values were used in conjunction with a straight or circular line generator to locate the intermediate boundary nodes.

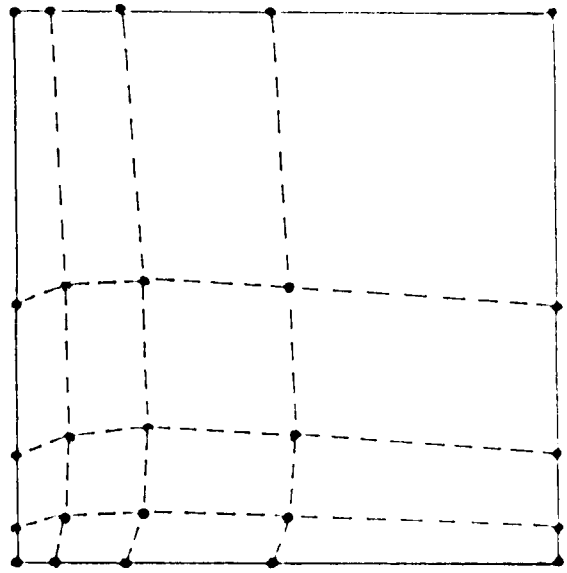
### Data Preparation

The finite element procedure requires the subdivision of the solution domain into a net of defined geometrical shapes (usually triangles or quadrilaterals in two-dimensional space). Because the detailed preparation of such grids may be quite laborious, semi-automatic generation procedures have been developed. The procedures available in this program are described in the following paragraphs.

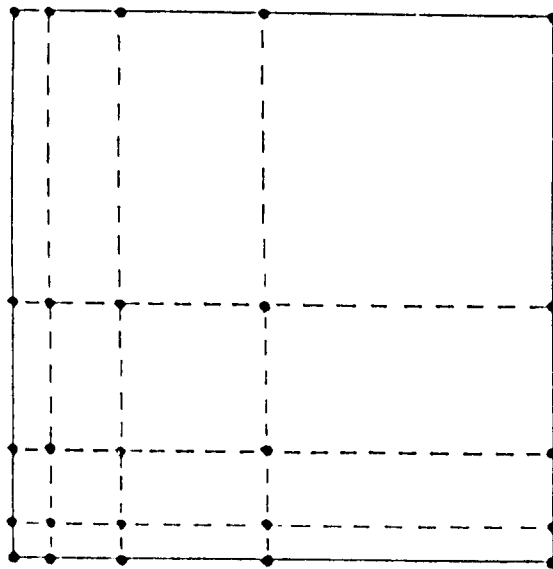
The region to be analyzed is represented by a series of quadrilateral elements, as shown in Fig. C.7. Each grid is defined by the nodal coordinates and the sets of eight node numbers which describe particular elements.



a. LAPLACE GRID  $\sim w = 0$

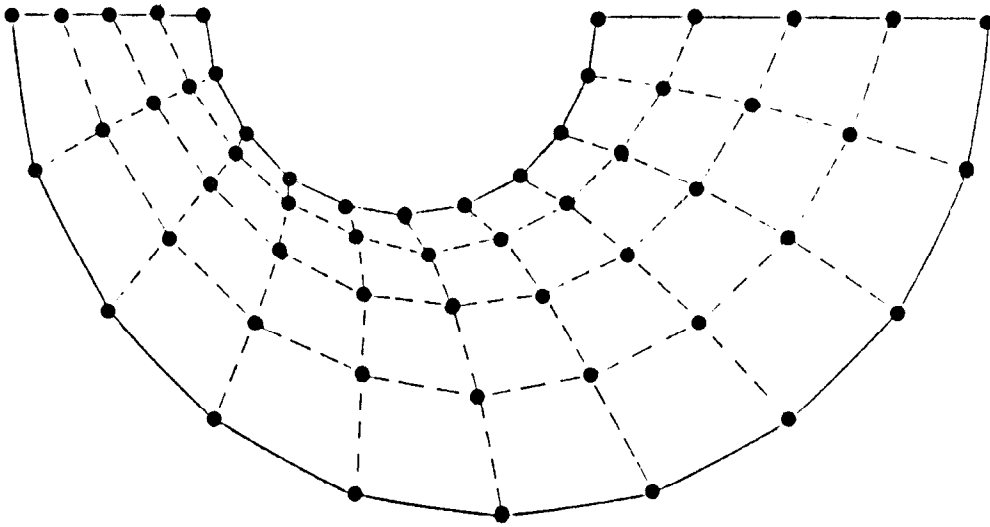


b. INTERMEDIATE GRID  $\sim w = 0.95$

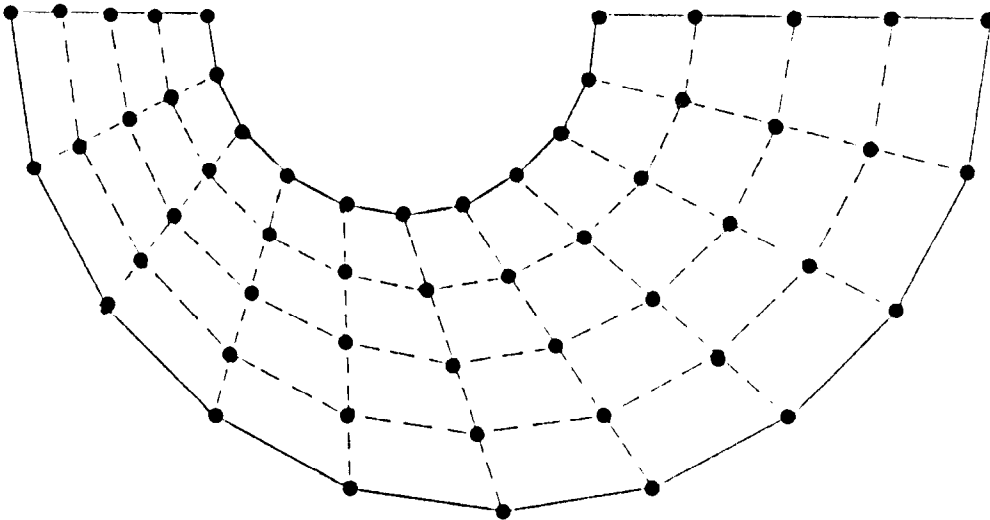


c. ISOPARAMETRIC GRID  $\sim w = 1.0$

Fig. C.5. Example to Illustrate Effect of Boundary Node Spacing



LAPLACE GRID  $\sim w = 0$



ISOPARAMETRIC GRID  $\sim w = 1.0$

Fig. C.6. Example to Illustrate Effect of Boundary Curvature



Attaining a satisfactory grid is an evolutionary process which often requires consideration of a number of alternatives before desired results are obtained. It is recommended that, initially, a rough sketch be made of the body with nodes placed at approximately their desired locations; the nodes and elements should be numbered on the sketch. A proper numbering scheme for the nodes is extremely important to the minimization of computational cost of a finite element analysis. For a given element, denote the greatest difference between the numbers of any two of the eight nodes which define the element as  $N_i$ . Denote the maximum value of  $N_i$  for the whole system as  $N_{\max}$ . To minimize computational effort, it is important that the node points be numbered so as to minimize the value of  $N_{\max}$  (the numbering used in Fig. C.7 gives  $N_{\max} = 13$ ; if the numbering had instead proceeded from left to right a value of  $N_{\max} = 19$  would have been obtained).

The sketch of the proposed grid is used to determine how the available generation procedures can best be applied to assist in preparation of the input data.

A stepwise description of the procedure is given in the following paragraphs.

1. The program has two available generation procedures to assist the user in describing the location of the node points. The use of these options can, for instance, permit one to describe the location of all the nodes for an arbitrarily large grid by as few as five cards.

2. The "circular arc (or straight line) coordinate generation option" may be used whenever several sequential points (either interior or exterior points) lie along a circular arc or straight line. For such points it is only necessary to enter the coordinates for the end points (denoted as  $N$  and  $N'$ ) of the sequence and the required generation information, INCR, INCR2, D and XC, YC. The generation information is entered on the second of this pair of cards, i.e., on the data card for  $N'$ . (The card for  $N'$  could also serve as the beginning card for a second segment  $N'-N''$ ; the generation data for

this segment would be contained on the card for N", etc.). INCR is the difference between the numbers of any two successive corner nodes in the sequence, and D is the ratio of the distances between successive pairs of corner points. For circular arcs XC, YC are the coordinates of some intermediate point on the arc, and INCR2 is the difference between N and the node number of the adjacent mid-point (to be used only if the elements along this arc are to have curved sides). If  $INCR \neq 0$  then intermediate points are generated along a straight line ( $XC = YC = 0$ ) or a circular arc ( $XC \neq 0$  and/or  $YC \neq 0$ ) between N' and the point described on the previous node card (N). That is, corner points  $N + INCR, N + 2 INCR, \dots, N' - INCR$  are generated. If the segment is a circular arc, it is defined as passing through the end points N and N' and some intermediate point (not necessarily one of the nodes) whose coordinates are (XC, YC). If  $INCR2 \neq 0$  for a circular arc, then the midpoints  $N + INCR2, N + INCR + INCR2, \dots$ , are also located on the arc; otherwise they are located on straight lines connecting the corner points.

The ends of the segment may be entered in any order, i.e., the segments shown in Fig. C.8 may be defined by specifying the end points in order  $7 \rightarrow 22$  or  $22 \rightarrow 7$ . The spacing of the intermediate corner node points is controlled by the value of the spacing ratio D. D is equal to the ratio of the lengths of the successive segments defined by the intermediate corner node points. A value of  $D = 1.0$  gives equally spaced corner points (if D is left blank, it defaults to 1.0). The locations of the intermediate corner points 12 and 17 (see Fig. C.8) could be generated by either specifying points  $7 \rightarrow 22$  and  $D = 2.0$  (Note:  $D = 2.0/1.0 = 4.0/2.0$ ), or  $22 \rightarrow 7$  and  $D = 0.5$  (Note:  $D = 2.0/4.0 = 1.0/2.0$ ); the value of INCR would be 5. For the circular arc of Fig. C.8a, if the element sides are to be curved and the segment is generated in the order  $7 \rightarrow 22$ , then  $INCR2 = 2$ ; if it is generated in the opposite way,  $22 \rightarrow 7$ , then  $INCR2 = -3$ . If  $INCR2 = 0$ , for a circular arc the element sides connecting the corner points will be straight.

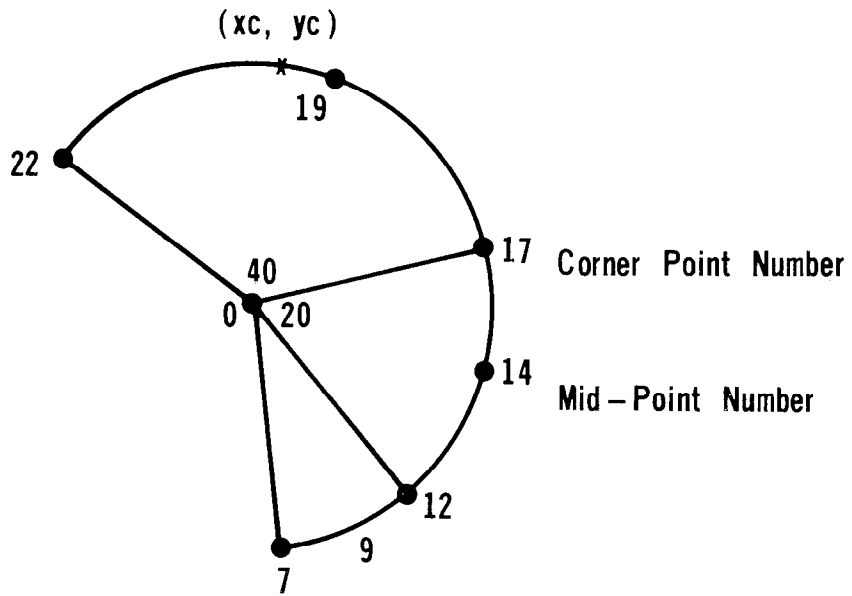


Fig. C.8a. Node Points Lying on a Curved Line

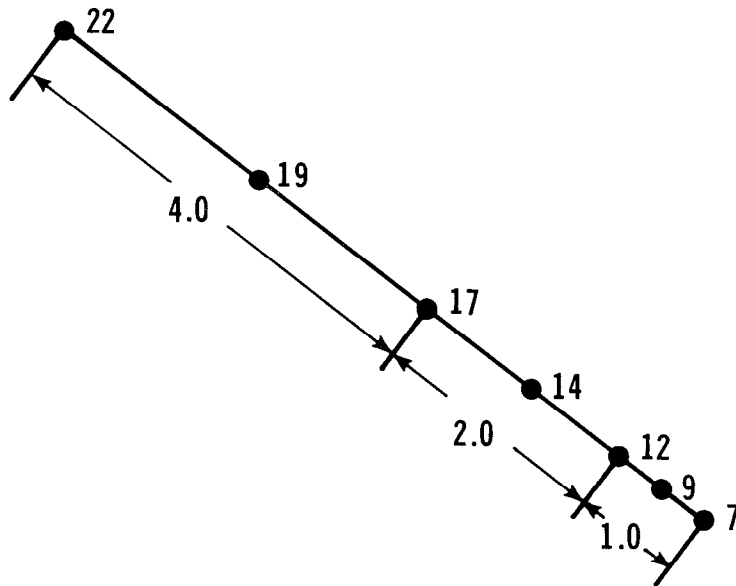


Fig. C.8b. Node Points Lying on a Straight Line

For the grid shown in Fig. C.7, the line segment generation procedure could be used to locate exterior points 1 → 56, 56 → 58, 58 → 62, 62 → 51, 51 → 7, 7 → 1. In addition, if desired, it could be used to locate interior points 12 → 18, etc.

Sometimes when using this generation procedure, it is necessary to enter a card for a point whose coordinates have already been specified or generated; e.g., one might generate 51 → 7 (Fig. C.7) then wish to generate 18 → 12. In such cases one need not enter the coordinates for the point a second time, instead the number of the point is entered with a minus sign and XP, YP are left blank.

3. The "interior node point generation option" locates all corner nodes interior to the body whose coordinates have not been explicitly specified by the user (either by direct input of the coordinates or by use of the line segment generation option). A family of generation schemes is available to the user; this family is dependent upon a parameter (supplied by the user) WTLMAX with a range of 0 → 1.0. A detailed description of this generation procedure is given in the section entitled "Theory." The parameter  $w$  used in that section is related to WTLMAX by the equation  $WTLMAX = 1.0 - w$ . This definition of WTLMAX yields an isoparametric grid for WTLMAX = 0.0 and a Laplacian grid for WTLMAX = 1.0; thus if WTLMAX is left blank, it defaults to the isoparametric grid.

It must be remembered that all corner nodes on the boundaries of the body must be either directly specified or generated by means of the line or arc segment generation scheme. In certain situations it may be desirable or even necessary to locate individually (or by means of the line generation option) certain interior points. The direct location of some interior points may be required to describe an interface between flows of varying densities or to improve the shape of the generated grid. Finally, the coordinates of all midpoint nodes, except those specified to lie on circular arcs, are generated so that the straight lines connecting the two adjacent corner points are divided into equal parts.

4. Once coordinates of the nodes have been specified or generated, the final task is to develop nodal connections (i.e., the numbers of the eight nodes defining the element) for all the elements, NOD(NELEM,8). Two alternatives are provided. One is to enter the information element by element, and the other is to generate it internally within the program. Internal element data generation is again dependent on specific grid numbering patterns, namely repeating nodal increments.

To utilize the "element data generation option," it must be possible to divide the grid into layers. A layer of elements is defined as a series of elements for which six of the eight node numbers of adjacent elements differ by two and the other two by one; e.g., the node numbers for elements 1 and 2 of Fig. C.7 are:

1	8	12	13	14	9	3	2
3	9	14	15	16	10	5	4

Thus elements  $1 \rightarrow 3, 4 \rightarrow 6$ , etc., of Fig. C.7 each constitute a layer. Let the number of elements in each layer be  $NMIS + 1$ . If the grid is regular then the corresponding node numbers of elements in adjacent layers will differ by a constant; denote this numbering increment by  $INCRP$  and the total number of layers by  $NMISP + 1$ . Thus the element information for the grid shown in Fig. C.7 can be completely described with one card containing the eight node numbers of element 1 and  $NMIS = 2, NMISP = 4$ , and  $INCRP = 11$ . The element numbers are assigned by the generation procedure beginning with the elements of the first layer and then proceeding to the second, etc.

5. The program output consists of a scaled plot of the grid, with node and element numbers being indicated at the discretion of the user. In addition, geometrical information (node numbers and their coordinates) and element nodal connections are printed. If the program data contains some inconsistencies which result in a non-positive area for a given element, an error message is printed, together with node numbers attributed to this element. The nonpositive

area is normally a result of a data error; e.g., (1) the nodes describing the element were entered in a clockwise manner instead of counterclockwise; (2) one of the node numbers describing the element was entered incorrectly; or (3) the coordinates for one of the nodes describing the element were entered incorrectly.

6. A set of options which deal with the format of the output plot are provided. These options include the following: PAPS - paper size (i.e., plot size in the limiting direction, width of the paper, is PAPS - 3.0); ENS - element number size in inches (it is recommended that element number size be twice the node number size); and codes IOPT(1) and IOPT(2), which determine whether the element and node numbers will be provided with the plot.

GRIDR is capable of generating elements whose sides are circular arc segments. In such a case, a non-zero value for INCR2 is entered and an actual arc is plotted on the output grid. There are provisions for up to 20 such arcs for each grid. If a larger quantity is desired, the arrays XI, YI, RI, THO, THF, and IFL will have to be redimensioned.

All the plotting instructions given in the program and manual apply specifically to the UCD PLOT PACKAGE library program. The plots are executed on a CAL COMP Digital Incremental Plotter Model 563, which is an off-line system. If the program is executed on another system, the following statements may require modification.

<u>Line #</u>	<u>Statement</u>	<u>Purpose</u>
1330	CALL PLOT	Open plot file.
3190	CALL SCALE	Scale Y and obtain maximum
3200		and minimum values for X and Y.
3210	CALL PLOT	Offset plot origin.
3480	CALL LINE	Draw line(s) between
		specified array of points.
3580	CALL NUMBER	Write a number at specified
3770		coordinates.
3630	CALL SYMBOL	Plot a special symbol or
		write an EBDIC string.

3710	CALL CIRCLE	Plot a circle or its segment.
3780	CALL PREXIT	Close plot file.

Lines 1000-1050 are Burroughs 6700/7700 system commands and should be suitably modified for other systems.

As the program is now dimensioned, the value of  $N_{\max}$  may not exceed 55, the maximum node number  $NPT$  may not exceed 700, and the number of elements  $NELEM$  may not exceed 600. These limitations may be modified by changing the dimensions of the program. If any one of these restrictions is violated, an error message is printed and the program proceeds to the consideration of the next problem.

When changing the dimensions of the program two areas must be considered:

- a. Dimension statements
- b. The dimension checks at the end of the program.

The dimensions in the program which are related to the size of the problem are indicated below:

$$X(N_1), Y(N_1), NOD(N_2, 8), S(N_1, 4)$$

where

- $N_1$  = maximum node number  
 $N_2$  = maximum number of elements.

## User's Manual

The input data required for the program is entered by means of the following set of cards.

- (1) Title Card (12A6)
- |         |      |       |   |  |
|---------|------|-------|---|--|
| Columns | 1-72 | TITLE | Any information that is to be printed as a title for the problem. |  |
|---------|------|-------|---|--|
- (2) Option Card (2F10.3,2I5,F10.3) 5\*
- |         |       |         |  |   |
|---------|-------|---------|--|---|
| Columns | 1-10  | PAPS    | Plotting paper size (12 or 30 inches for Cal Comp Plotter Model 563).  | 6 |
|         | 11-20 | ENS     | Element number size in inches.   |   |
|         | 21-25 | IOPT(1) | Specifies whether to plot the element numbers. When set to 1 numbers will not be plotted, otherwise leave blank. |   |
|         | 26-30 | IOPT(2) | Specifies whether to plot the node numbers. When set to 1 numbers will not be plotted, otherwise leave blank.    |   |
|         | 31-40 | WTLMAX  | Grid generation parameter.   | 3 |
- (3) Node Point Data Identification Card (1I)
- Punch 1 in column 1 -- indicates that node point data follows.
- (4) Node Point Information Array (1I,14,2F10.3,2It,3F10.3) 1
- |        |       |      |                           |  |
|--------|-------|------|---------------------------|--|
| Column | 1     | NSEC | Leave blank.              |  |
|        | 2- 5  | N    | Node point number.        |  |
|        | 6-15  | XP   | x-coordinate of the node. |  |
|        | 16-25 | YP   | y-coordinate of the node. |  |

---

\* Reference to paragraph numbers in section entitled "Data Preparation."

26-30	INCR	Numbering increment.	} Quantities associated with curved or straight line generation option	2
31-35	INCR2	Numbering increment between corner node and midpoint on a circular arc.		
36-45	D	Spacing ratio.		
46-55	XC	Coordinates of a point interior to circular arc; leave blank for straight line.		
56-65	YC			

Use as many cards as are necessary to specify or generate the locations of all exterior corner nodes. 3

(5) Element Data Identification Card (I1)

Punch 2 in Column 1 -- indicates that element data follows.

(6) Element Information Array (I1,I4,I0I5)

Column	1	NSEC	Leave blank.	
	2- 5		The numbers of the eight node points which describe the element. Enter the nodes in sequence, reading <u>counterclockwise</u> around the element. The first entry must be a corner node.	
	6-10			
	11-15			
	16-20	NODP(8)		
	21-25			
	26-30			
	31-35			
	36-40			
	41-45	NMIS	The number of additional elements in the layer.	4
	46-50	NMISP	Number of additional layers.	
	51-55	INCRP	Numbering increment for the layers.	

As many cards as are necessary to define all the elements in the system. The order of the element cards need bear no relationship to the locations of the elements in the body.

(7) End Card

Punch 3 in Column 1 -- indicates end of data.

## Example Problems

To enhance user's comprehension of the program, a number of examples are provided. They are presented in order of increasing complexity with detailed explanations appended.

### Example problem #1

The simplest finite element network to generate is a rectangular grid.

The solution domain in this case is a 60 x 40 node rectangle. A preliminary grid is sketched in Fig. C.9 and two possible numbering schemes are presented. The choice of the numbering scheme is dependent upon the value of  $N_{\max}$  (see "Data Preparation" section), which in turn influences the computational cost of the problem. The lowest cost is obtained whenever  $N_{\max}$  is minimized. On the basis of this criterion, the grid pattern shown in Fig. C.9a ( $N_{\max} = 17 - 1 = 16$ ) is adopted, since for Fig. C.9b  $N_{\max}$  is  $23 - 1 = 22$ .

Upon inspection of the grid, it is evident that the node numbers do form an incremental sequence along the boundaries of the body. Since these boundaries are straight lines, the "straight line node generation option" is used. Nodes are generated along lines:  $1 \rightarrow 9$ ,  $\text{INCR} = 2$ ;  $9 \rightarrow 93$ ,  $\text{INCR} = 14$ ;  $93 \rightarrow 85$ ,  $\text{INCR} = -2$ ; and  $85 \rightarrow 1$ ,  $\text{INCR} = -14$ . The input format for these data is illustrated in Fig. C.10. Only the coordinates are specified for the first entry (node #1), and the generation option data is entered on the subsequent node card (node #9). The next statement generates nodes from #9 to #93 (coordinates for node #9 have already been specified on the previous card).  $D$  is set to 1.0 (recall that the default value is 1.0) since the grid is equally spaced, and  $\text{INCR2}$  is zero because circular arc generation is not performed. Once the boundary nodes are established, the program generates the interior node coordinates.

The element nodal connections must now be established. The grid shown in Fig. C.9a lends itself nicely to division into element layers. The first such layer is composed of elements 1, 2, 3, and 4. In this case nodal connections for element 1 are entered, starting with a

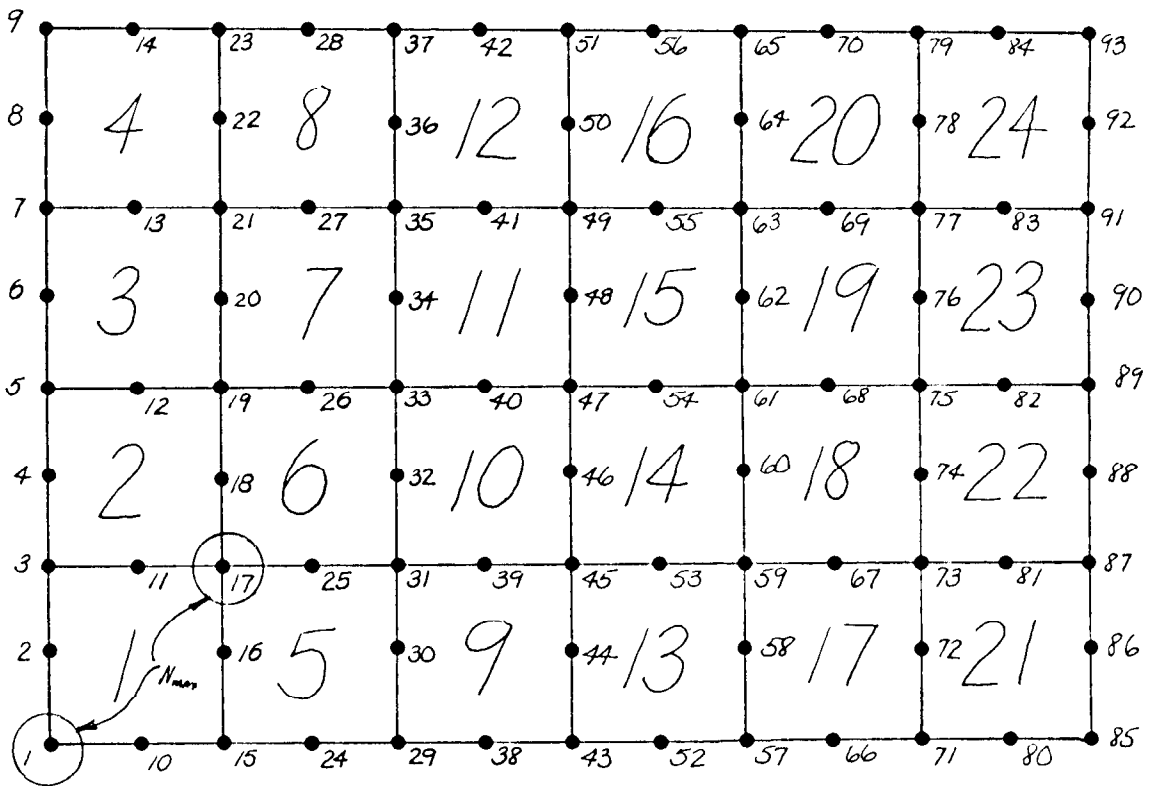


Fig. C.9a. Grid Sketch, Example Problem #1,  $N_{\max} = 16$

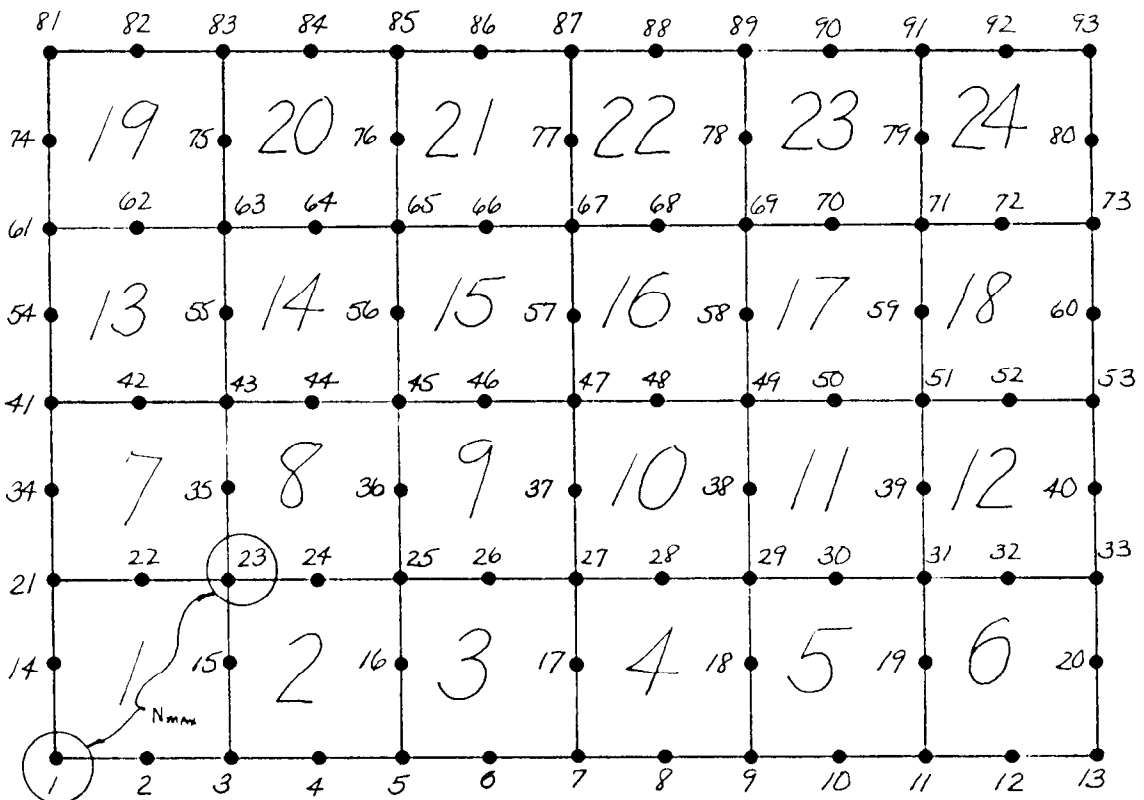


Fig. C.9b. Grid Sketch, Example Problem #1,  $N_{\max} = 22$



corner node (#1) and proceeding counterclockwise around the element (nodes #10, 15, 16, 17, 11, 3, 2). There are 3 more elements in the layer which possess the same nodal increment, i.e.,  $NMIS = 3$ . There are 5 more layers such as the one described above. Therefore,  $NMISP$  is set to 5 and  $INCRP = 14$  (see Table C.1 for additional details). The resulting output consists of nodal coordinates along with element information and the grid plot shown in Fig. C.11.

#### Example problem #2

In this case a square body consisting of two different materials whose interface is a circular arc is presented in Fig. C.12. Since the dimensions of the body are equal in both directions, and the elements are equally spaced,  $N_{max}$  will be the same regardless of numbering pattern ( $N_{max} = 26 - 1 = 25$ ). Due to the node numbering system, again it is possible to use the "node generation options". The generation sequence of boundary and interface points is as follows: 70 → 162,  $INCR = 23$ ; 162 → 170,  $INCR = 2$ ; 170 → 176,  $INCR = 2$ ; 176 → 15,  $INCR = -23$ ; 15 → 1,  $INCR = -2$ ; 1 → 70,  $INCR = 23$ ; 70 → 78,  $INCR = 2$ ,  $INCR2 = 1$  ( $XC = 25.0$ ,  $YC = 15.8$ ); 78 → 170,  $INCR = 23$ ,  $INCR2 = 11$  ( $XC = 15.8$ ,  $YC = 25.0$ ). Elements with curved sides are used along the circular interface; thus values for  $XC$ ,  $YC$ , and  $INCR2$  must be entered. Each circular arc is uniquely defined by specifying a third point ( $XC$ ,  $YC$ ) on the arc (see Fig. C.13). Whenever nodes #70 and 170 are used again they are entered with a negative sign and  $XP$  together with  $YP$  are left blank. The boundary nodes are equally spaced; therefore  $D$  is set to 1.0 by default.

Development of nodal connections for this example is somewhat more difficult; nevertheless, three distinct element layers can be identified. The first layer contains elements 1, 2, 3, 4, 5, 6, and 7; the second layer, elements 22, 23, and 24; and the third, elements 34, 35, 36, and 37. Each of these layers is associated with a similar set of elemental layers. For example, the layer containing elements #34, 35, 36, and 37 has three layers above it which are similar. Therefore, node numbers for element 34 are entered counterclockwise, starting with corner node #70 along with  $NMIS = 3$ ,  $NMISP = 3$ , and



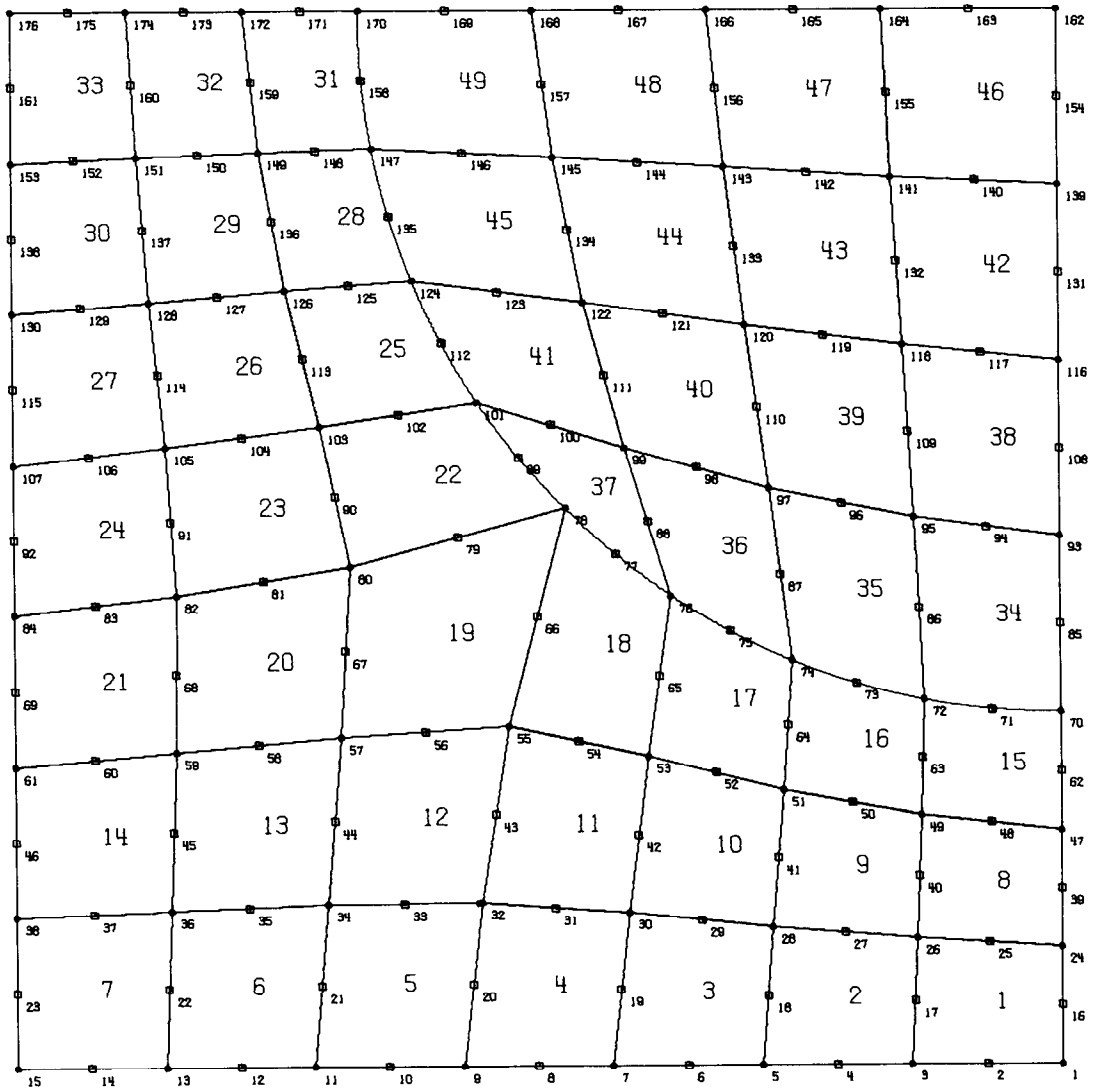


Fig. C.12. Example Problem #2, Grid Sketch

		FORTRAN STATEMENT													
1	STMT. CONT. NUMBER	5	6	10	15	20	25	30	35	40	45	50	55	60	65
1	GRID	GENERATOR	OR	EX	AMPLE	PROBLEM	#	2							
	12.0		0.14					1.0							
1															
	70	37.5		12.5											
	162	37.5		37.5		23									
	170	12.5		37.5		2									
	176	0.0		37.5		2									
	15	0.0		0.0		-23									
	-70					-23									
	78	19.82		19.82		2		1				25.0		15.8	
	-170					23		11				15.8		25.0	
2															
	1	16	24	25	26	17		3		2	6	2	23		
	78	89	101	102	103	90		80		79	2	3	33		
	70	85	93	94	95	86		72		71	3		23		
3															

Fig. C.13 Data Input, Example Problem #2.

INCRP = 23. The plotted results are shown in Fig. C.14. If INCR2 is not specified for a circular arc, then elements with straight sides are produced.

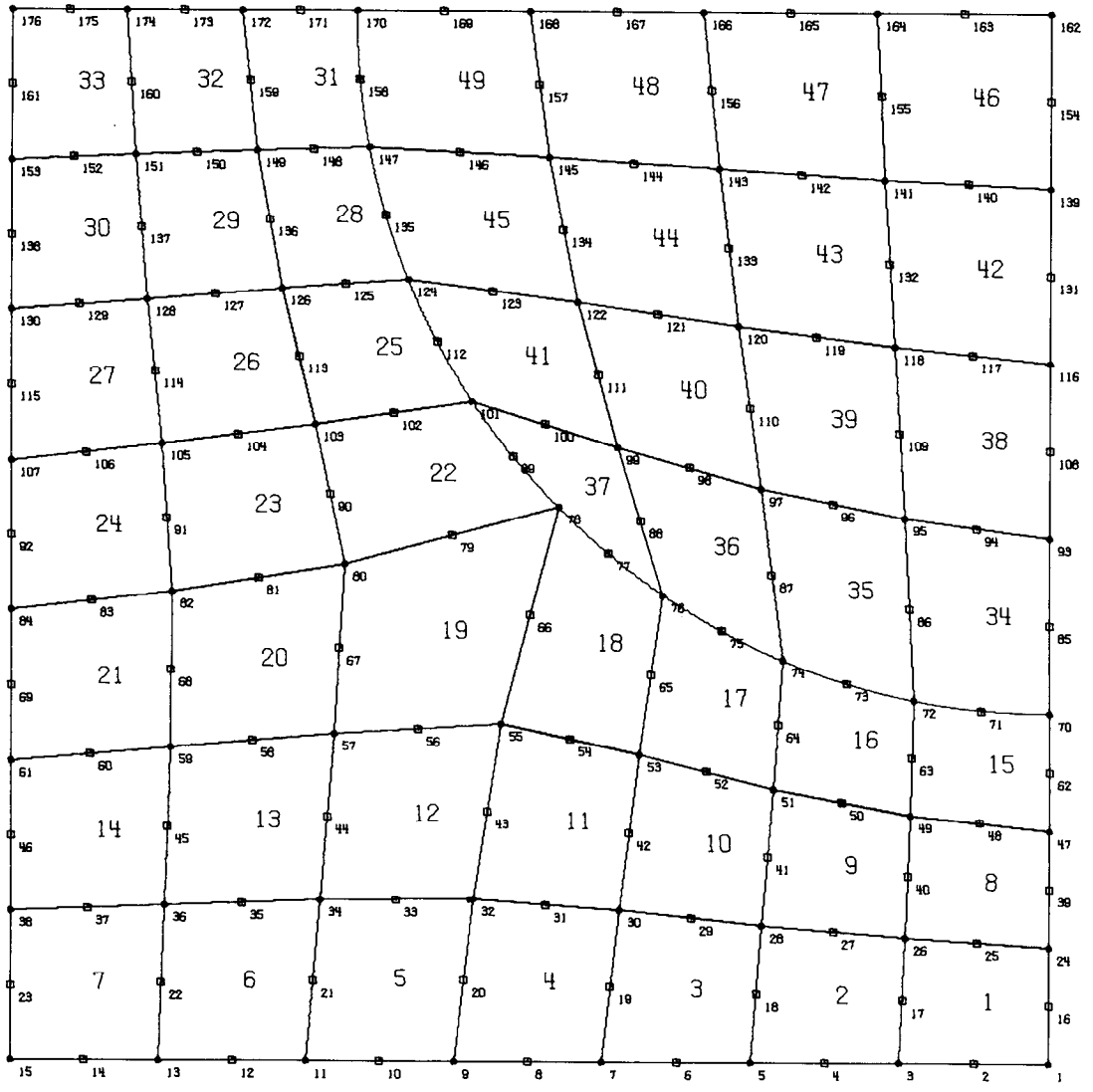


Fig. C.14. Plotted Output for the Example Problem #2

Graphical output is invaluable in visualizing simulations which would otherwise require the processing and plotting of thousands of numbers. A contour plotting routine that can plot contours from data points at the corners of arbitrary quadrilaterals is presented here.

### Interpolating Using Shape Functions

Since the finite element grids used in this and in many other studies are composed of interconnected quadrilateral elements, it is necessary to interpolate from values available at the corners and midside nodes of quadrilaterals. Most contour plotting programs use data on a rectangular grid and plot the contours by interpolating linearly on the boundary of each cell. Each contour would then be composed of a number of line segments connected at cell boundaries.

Using the shape functions themselves in making the interpolations has these main advantages:

- a. Quadrilateral elements present no problem since the isoparametric transformation to a square can be made with ease.
- b. Since the approximation contains quadratic terms, it will yield a better approximation to the function than a linear approximation.
- c. More detail can be obtained by using sub-elements within each element.
- d. Such a plot made from the results of a finite element program would actually give the exact values of the function within the element that the solution predicts since the same shape functions are used in the minimization and the plotting routine.
- e. Easy programming and relatively low cost.

Consider a four-noded quadrilateral element. The values of the function to be plotted will be known at the corners of the quadrilateral. If the global coordinate system is  $(x, y)$  and the local coordinate system  $(\xi, \eta)$  then, as in Appendix A, shape functions  $N_i$   $(\xi, \eta)$  may be defined so that

$$x = N_i x_i \quad (D.1)$$

$$y = N_i y_i \quad (D.2)$$

$$f = N_i f_i \quad (D.3)$$

where  $(x, y)$  are the coordinates of some point within the element and  $f$  the function value at that point. The quadrilateral is transformed to a square so that all elements will be the same square in the  $(\xi, \eta)$  plane for easy subdivision.

An example of the mapping of the approximation  $N_i f_i$  to the function within an element is shown in Fig. D.1. The contour of value  $n$  is the projection on the base of the intersection of the plane parallel to the base and  $n$  units above it and the function surface. Such a projection is shown in Fig. D.2, together with the straight line obtained by joining the interpolated points on the boundary, which is the method used by many contour plotting routines in existence.

There are two possible methods of obtaining this intersection curve, i.e., contour. The first is to determine the  $\xi$  and  $\eta$  coordinates of a number of points within the element which satisfy

$$f_n = N_i f_i \quad (D.4)$$

then, determine the corresponding  $(x, y)$  values of these points from the relationships in equations D.1 and D.2, and plot the contour of value  $f$ . However, where the contour doubles up on itself multiple values of the coordinates result, leading to difficulties in determining which points to join. The second method is to subdivide the element into a series of sub-elements and determine the function value at the corners of each sub-element using equation D.3. Linear interpolation is then used to obtain the line segments which form the contour within the element.

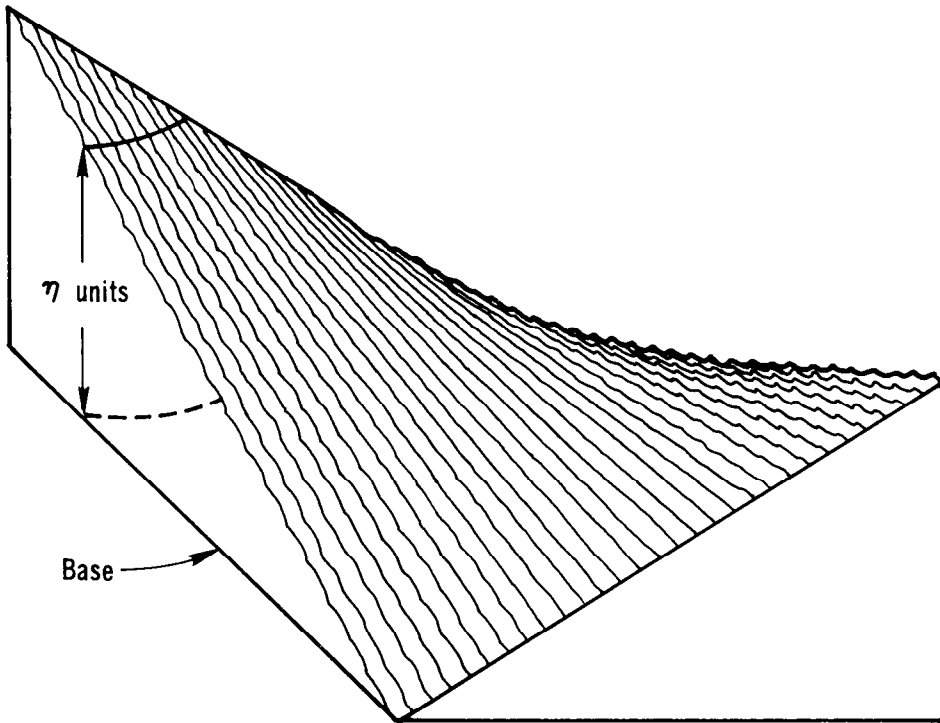


Fig. D.1. Approximation to Function Within the Element

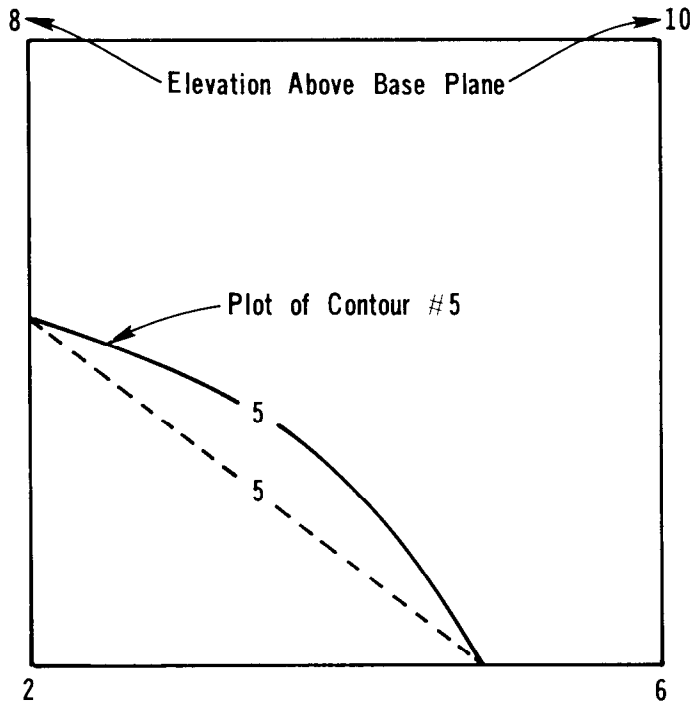


Fig. D.2. Element With Contours Using Shape Function and Linear Approximation

Higher order approximations would require intermediate nodes and can be used in exactly the same fashion, but the sub-elements would still have only four corner nodes.

Certain ambiguous cases where it is not possible to say which way the contour should be sketched are shown in Fig. D.3 for a contour of value 1.

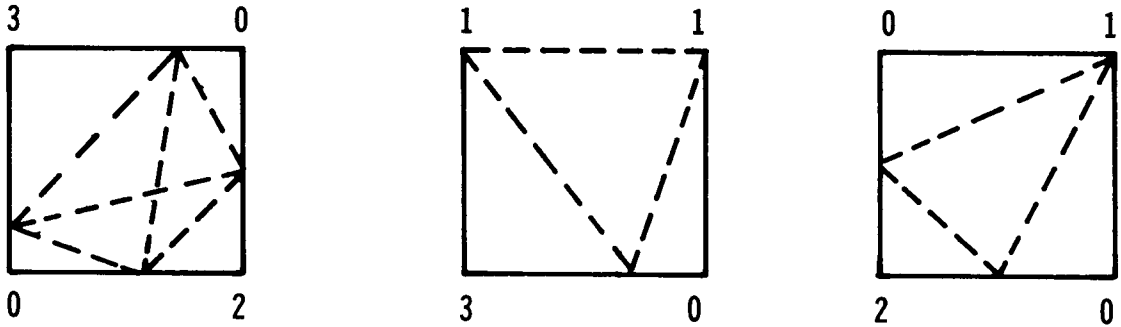


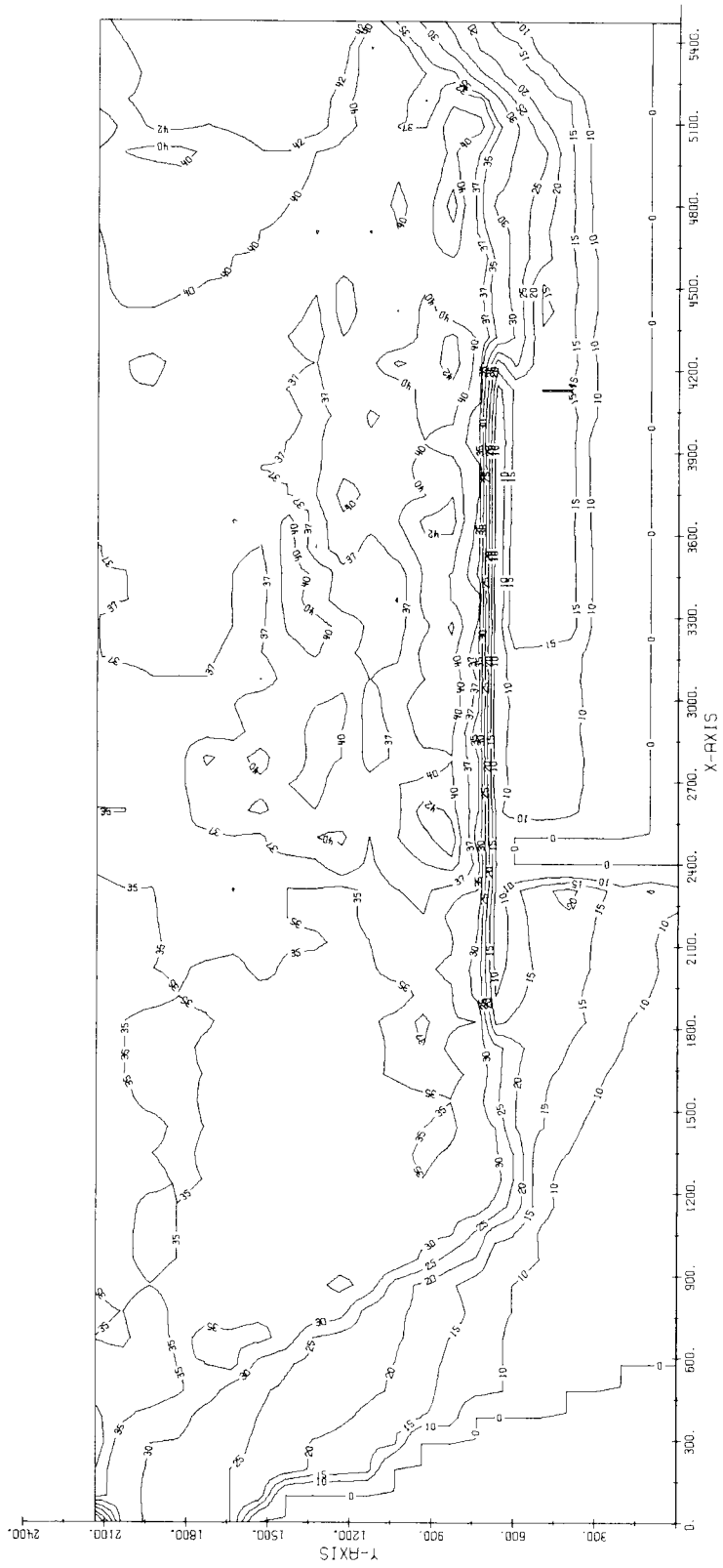
Fig. D.3. Ambiguous Cases

However, the subdivision of such an element will result in a mathematically correct contour. This is an added advantage of using shape functions for interpolation.

#### Data Preparation

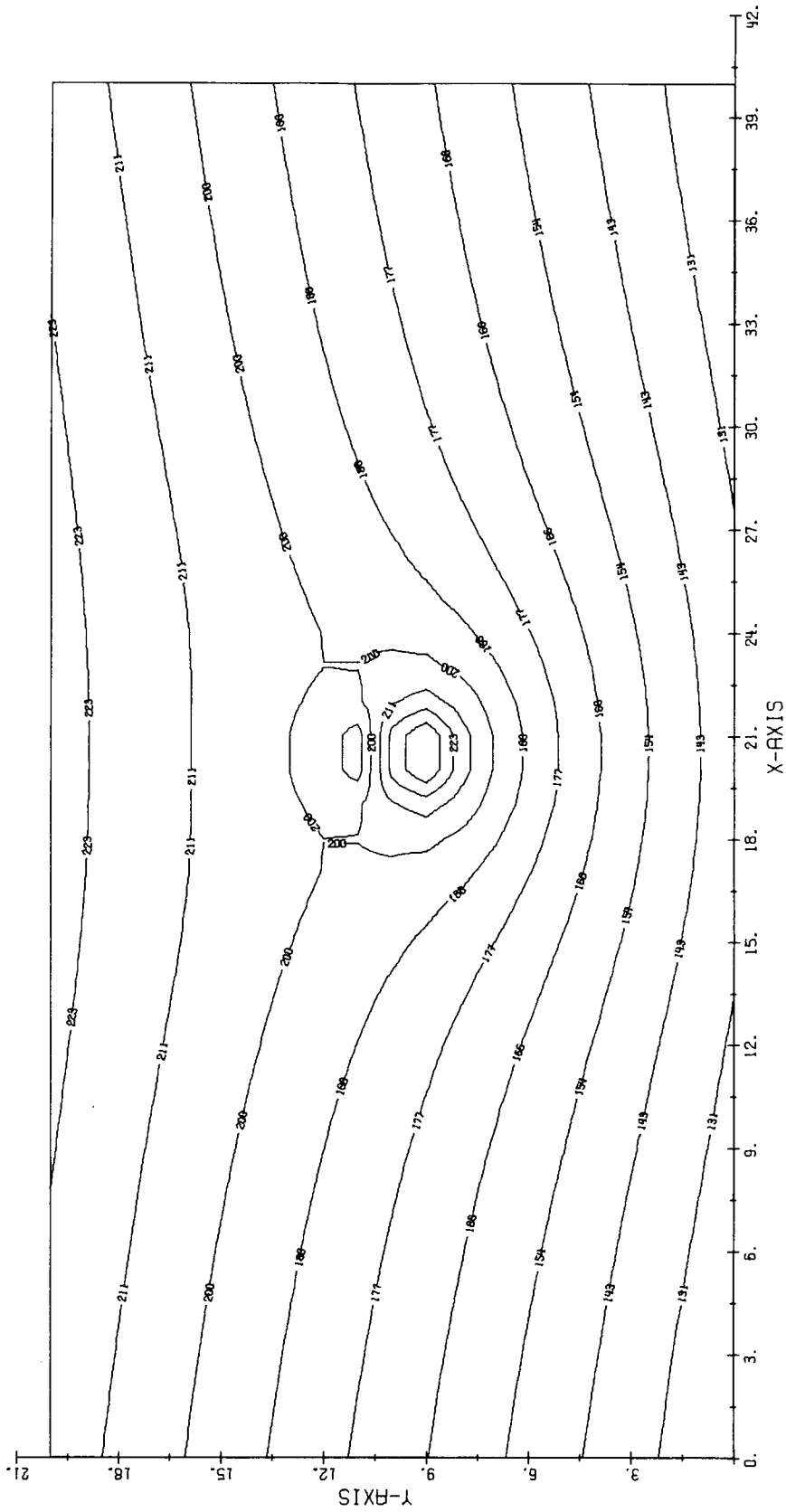
Three types of data can be used for contour plotting with the program CONTR/MK2: finite element grid, finite difference rectangular grid, and measured values on either a quadrilateral or rectangular grid. The program has a built-in rectangular grid generator which assigns node numbers and nodal connections to data which is not in the finite element form. Automatic scaling and optional determination of contour values in the range of function values are features of the program.

Contours can be labeled in ascending order of magnitude given in the legend, or the contour value itself can be written on the plot provided it is an integer between 1 and 999. The x and y axes may be plotted if desired. Examples of contour plots made by the program are shown in Figs. D.4 and D.5.



SOCIAL RICHMOND DEPTH SOUNDINGS, SHEET #36

Fig. D.4. Example Contour Plot of Depth Soundings



POTENTIAL FLOW WITH CIRCULATION

Fig. D.5. Example Contour Plot of Potential Flow

## User's Manual

The input data required for the program are entered by means of the following cards:

(1) Title Card (8A6,I2)

Columns	1-48	TITL	Any information to be printed as a title for the problem.
	49-50	NN	Number of alphanumeric characters in the title string.

(2) Option Card (2F10.5,F5.2,9I5)

Columns	1-10	PAPER	Plotting paper size (12 or 30 inches for Cal Comp Plotter Model 563).
	11-20	DY	Scaling factor in y-direction (units/inch). If $\emptyset\text{PTI}\emptyset\text{N}(4) = 0$ DY should be left blank.
	21-25	HCN	Size of the contour label number. Minimum value is 0.07 inch. If HCN is less than 0.07 or left blank, it is set to 0.07 by default.
	26-30	$\emptyset\text{PTI}\emptyset\text{N}(1) =$	0 Finite element or quadrilateral grid type data. 1 Finite difference or rectangular grid type data. Grid generated through RGRID subroutine.
	31-35	$\emptyset\text{PTI}\emptyset\text{N}(2) =$	0 Contour values computed automatically by (FMAX-FMIN)/NC. 1 Contour values read in by the user.
	36-40	$\emptyset\text{PTI}\emptyset\text{N}(3) =$	0 Labeled "X" and "Y" axes will be plotted. 1 Axes suppressed (not plotted).
	41-45	$\emptyset\text{PTI}\emptyset\text{N}(4) =$	0 Scaling factor DY (units/inch) is computed automatically to first significant digit. 1 DY and NDP read in by the user.

46-50	ØPTIØN(5) = 0	Split number (NS) is set to 5 by default. N Split number (NS) equals N.
51-55	ØPTIØN(6) = 0	Contour label numbers written. 1 Contour values written (limited to integers from 1-99).
56-60	NC	Number of contours to be plotted.
61-65	INCR	Plotter increment count between two contour value labels (usually $\approx 30$ ).
66-70	NDP	Number of digits past the decimal point for the axis labels. To be left blank if ØPTIØN(4) = 0.

(3) Contour Value Card (8F10.5)

Columns	1-80	FC(I)	Contour values to be read in using F10.5 format. If ØPTIØN(2) = 0, skip this card.
---------	------	-------	--

(4) Finite Element Information Card\* (3I5)

Columns	1- 5	NP	Number of node points.
	6-10	NE	Number of elements.
	10-15	NBDR	Number of boundary nodes.

\*NOTE: If ØPTIØN(1)  $\neq$  0, skip this card.

(5) Node Point Information Array\* (2(I10,3F10.5))

Columns	1-10	J	Node point number.
	11-20	XC(J)	X-coordinate of the J-th node point.
	21-30	YC(J)	Y-coordinate of the J-th node point.
	31-40	U(J)	Function value @ J-th node point.
	41-80	Repeat as above	

\*NOTE: If ØPTIØN(1)  $\neq$  0, skip this card.

(6) Element Information Array\* (3(5I5))

Columns	1- 5	J	Element number.
---------	------	---	-----------------

6-10		The numbers of four
11-15		consecutive node points which
16-20	NØP(J,K)	describe the element. They
21-25		should be entered in sequence
		<u>counterclockwise</u> around the
		element.

26-75 Repeat as above twice

\*NOTE: If ØPTIØN(1) ≠ 0, skip this card.

Use as many cards as are necessary to define all elements in the system.

(7) Boundary Node Information Array\* (16I5)

Columns	1-80	NB	Consecutive boundary node point numbers entered in I5 format.
---------	------	----	---

\*NOTE: If ØPTIØN(1) ≠ 0, skip this card.

Use as many cards as are necessary to define all essential boundary node points.

(8) Rectangular Grid Generator Information Card\* (2I5,4F10.5,  
I10,2F10.5)

Columns	1- 5	NX	Number of panels (cell segments) in X-direction.
	6-10	NY	Number of panels (cell segments) in Y-direction.
	11-20	XL	Total length in X-direction.
	21-30	YL	Total length in Y-direction.
	31-40	XR	X-direction spacing ratio. If equally spaced XR = 1.0. If Geometric spacing can be obtained by entering a desired spacing ratio.
	41-50	YR	Y-direction spacing ratio. Same components apply as above.
	51-60	KCØD	0 No odd panels (segments) are to be read in. (All equal or geometrically spaced.) 1 Odd panels will be read in by the user.
	61-70	DX	Length of a regular panel in X-direction. Can be left blank if KCØD = 0.

71-80 DY Length of a regular panel in Y-direction. Same comments apply as above.

\*NOTE: If  $\emptyset\text{PTION}(1) \neq 0$ , skip this card.

(9) Odd Panels Information Card\* (2I10)

Columns 1-10 NDX Number of odd panels in X-direction.

11-20 NDY Number of odd panels in Y-direction.

\*NOTE: If  $\text{KC}\emptyset\text{D} = 0$  or  $\emptyset\text{PTION}(1) = 0$ , skip this card.

(10) Odd Panels Information Array, X-Direction\* (I10,F10.5)

Columns 1-10 N Panel number, X-direction.

11-20 DXX(N) N-th panel size, X-direction.

\*NOTE: If  $\text{KC}\emptyset\text{D} = 0$  or  $\emptyset\text{PTION}(1) = 0$  or  $\text{NDX} = 0$ , skip this card.

As many cards as are necessary to enter all odd X-direction panels.

(11) Odd Panel Information Array, Y-Direction\* (I10,F10.5)

Columns 1-10 N Panel number, Y-direction.

11-20 DYY(N) N-th panel size, Y-direction.

\*NOTE: If  $\text{KC}\emptyset\text{D} = 0$  or  $\emptyset\text{PTION}(1) = 0$  or  $\text{NDX} = 0$ , skip this card.

As many cards as are necessary to enter all odd Y-direction panels.

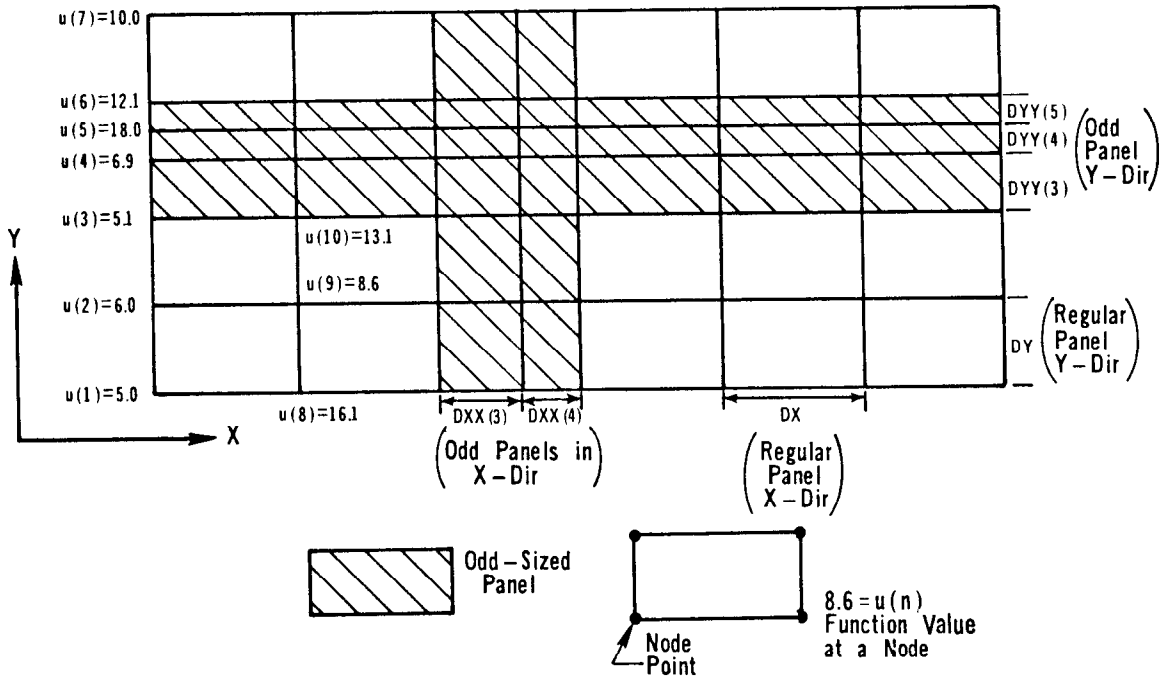
(12) Function Array Information\* (8F10.5)

Columns 1-80 U(I) Function values at each corner point, specified consecutively along a row or column in either X or Y-direction (usually Y).

\*NOTE: If  $\emptyset\text{PTION}(1) = 0$ , skip this card.

Use as many cards as necessary to specify: 1) all function values associated with a corner point along a particular row, and 2) all such rows for the whole system.

General Comments

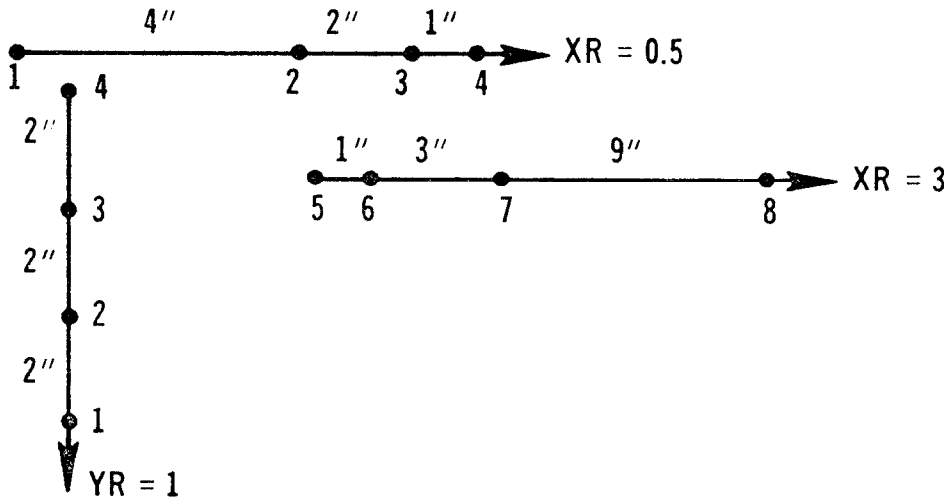


For the above problem:

NX = 7	DX = 5.0	N = 4, DYY(4) = 1.0
NY = 6	DY = 3.0	N = 5, DYY(5) = 1.0
XL = 30.0	NDX = 2	U(1) = 5.0, U(2) = 6.0
YL = 13.0	NDY = 3	U(3) = 5.1, etc.
XR = 1.0	N = 3, DXX(3) = 3.0	U(i) must start on
YR = 1.0	N = 4, DXX(4) = 2.0	a new card in
KCØD = 1	N = 3, DYY(3) = 2.0	columns 1-10.

Rectangular grid input

- (1) Maximum allowable DY is computed in the following way  
 $(YMAX - YMIN)/(PAPER-4.0)$ . Automatic scaling routine  
 computes DY to maximum one significant figure number.
- (2) Spacing ratio (XR, YR) is a ratio between lengths of two  
 consecutive cell segments.



- (3) In the interest of program efficiency, data should be  
 entered consecutively into both Node Point Array and Element  
 Array.
- (4) If there are more function values along a given row than 8,  
 continue on the next card(s) until all the information for  
 that particular row is entered. First function value for  
 each row must be entered on a new card in cols. 1-10.
- (5) At present CØNTR/MK3 has the following dimensions:
  - a. Maximum number of nodes - 1500; U(1500), XC(1500),  
 YC(1500).
  - b. Maximum number of contours - 20; FC(20).
  - c. Maximum number of boundary nodes - 500; NB(500), NBDR.
  - d. Maximum split number - 100; NS, XX(100), YY(100),  
 SI(100), ET(100).

Due to the volume and complexity of the input data needed to make a full-scale simulation, it would often be easier to change the format of the read statements in the program than to change the form of the data. A description of the input routines is given in this section following general comments on data preparation.

### Data Preparation

Although a concerted effort was made to quantify parameters that would aid in the selection of optimal grid and time spacing, only qualitative descriptions may be inferred from Part V of the main text. The choice of grid and time step size is critical, and the user can depend on experience, if there is any available, or use the classical method of subdivision, i.e., an initial grid and time step are first used to simulate a few time steps of the problem, the grid is then subdivided and the run made again. The difference between the results of the two runs at common nodes is a measure of the error in the numerical solution. If the error estimate is higher than acceptable, the grid may be further subdivided. The same process can be applied to the time step size. The cost and time spent in so selecting the proper discretizing parameters will be returned many times over when the full simulation is made.

### Input

The program has a built-in rectangular grid generator to facilitate the use of the velocity profiles generated from finite difference programs or measured on rectangular meshes.

Nodal connections, initial concentrations, and initial bed profile are read in subroutine INPUT1. This subroutine is only called once at the beginning of each execution. When the grid-generating program is used, the node point coordinates and nodal connections must

be stored and then read into the main program. New flow field and/or boundary conditions are read by subroutine INPUT for appropriate time steps.

User's Manual for Sediment II (Vertical Model)

CARD 1

Columns 1-72 TITLE

CARD 2 (8I10)

Columns	1-10	NOPT	Problem option. 1 Steady state concentration problem. 2 Unsteady concentration problem. 3 Sediment problem (transient).
	11-20	NP	Number of node points.
	21-30	NE	Number of elements.
	31-40	NPX	Number of corner nodes.
	41-50	NDCOD	No initial bed profile if 0, otherwise 1.
	51-60	NTTS	Number of time steps.
	61-70	NGRID	Generate rectangular grid if equal to 1, otherwise 0.

For transient problems (i.e., NTSS > 1), include this card.

CARD 3 (3F10.5)

Columns	1-10	TETA	Crank-Nicolson weighting function.
	11-20	DT	Time increment.
	21-30	TIM(1)	Initial time.

SET 4 (80I1) from 1 → NP

NFIX(J)	1 if concentration specified at this node or 0. Use as many cards as necessary.
---------	---

For NGRID = 1: rectangular grid is generated.

CARD 1 (2I10,4F10.5)

Columns	11-20	NX	Number of panels in x-direction.
	21-30	NY	Number of panels in y-direction.
	31-40	XL	Total length in x-direction.
	41-50	XY	Total length in y-direction.
	51-60	XR	Grid spacing ratio (x).
	61-70	YR	Grid spacing ratio (y).

CARD 2 This card is designed for test problems only. It sets the same values of all the parameters below for all elements and nodes. (8F10.5)

Columns	1-10	XV	x-velocity.
	11-20	YV	y-velocity.
	21-30	DIFX	x-diffusion coefficient.
	31-40	DIFY	y-diffusion coefficient.
	41-50	ELS	Element source terms.
	51-60	DEEP	Width of channel.
	61-70	CCCC	Initial concentration.
	71-80	VSS	Settling velocity.

CARD 3 (I10)

Columns	1-10	NCARDS	Number of cards on which B.C. are specified next.
---------	------	--------	---

CARD 4 et seq to NCARDS (I10,F10.5)

Columns	1-10	NUM	Node point number.
	11-20	SPEC(NUM,1)	Specified concentration.

If NGRID = 0, the geometry and element properties are read in by Subroutine INPUT1.

SET 1 (10I5,2F5.2,2F10.5) 1 → NE

Columns	1- 5	J	Element number.
	6-10	WBE(J)	Equals 1 if bottom element, otherwise 0.
	11-50	NOP(J,K)	Nodal connections (I5).
	51-55	DIF(J,1)	x-diffusion coefficient.
	56-60	DIF(J,2)	y-diffusion coefficient.
	61-70	VS(J)	Settling velocity.
	71-80	TAUCD(J)	Critical shear stress for deposition.

SET 2 (4(I10,F10.5)) 1 → NP

4 pairs of values on each card.

(I10),K	Node point number.
(F10.5),CØNC(K)	Initial concentration at node K.

Initial bed profile read if (NCOD ≠ 0).

SET 3 (2I5,14F5.2)

Only for bottom elements.

Columns	1- 5	J	Element number.
	6-10	NLAY(J)	Number of layers on bottom, maximum 7.
	11-45	THICK(J,K)	Thickness of each of the 7 layers, enter 0 for non-existent layers (F10.5).
	46-80	SST(J,K)	Shear strength of the 7 layers.

Transient problem input.

CARD 1 et seq (16I5)

IFF(J,1)	Input code for each time step; 0 for first time step. 0 No input at this time step. 1 New velocity field to be read in. 2 New boundary conditions only. 3 New velocities <u>and</u> boundary conditions read.
----------	---

CARD 2 et seq (16I5)

IFF(J,2)	Output code for each time step. 0 No output. 1 Bed profile and erosion/deposition rate. 2 Concentrations only. 3 Both.
----------	--

Subroutine INPUT is called whenever  $IFF(J,1) \neq 0$ .

a) If  $IFF(J,1) = 1$  (Velocity field only).

SET 1 (I10,4F10.5) 1 → NP

Columns	1-10	J	Node point number.
	11-20	CORD(J,1)	x-coordinate.
	21-30	CORD(J,2)	y-coordinate.
	31-40	SVEL(J,1)	x-velocity.
	41-50	SVEL(J,2)	y-velocity.

SET 2 (I10) (New Diffusion Coefficients & Settling Velocities)

Columns	1-10	NCAR	Number of cards to follow.
---------	------	------	----------------------------

SET 3 (I10,3F10.5) 1 → NCAR

Columns	1-10	N	Element number.
	11-20	DIF(N,1)	x-diffusion coefficient.
	21-30	DIF(N,2)	y-diffusion coefficient.
	31-40	VS(N)	Settling velocity.

b) If IFF(J,1) = 2 (Boundary conditions only)

CARD 1 (I10)

Columns	1-10	NCARDS	Number of cards to follow.
---------	------	--------	----------------------------

SET 2 (4(I10,F10.5)) 1 → NCARDS

4 pairs on each card.

	J	Node point number (I10).
	SPEC(J,1)	Specified concentration (F10.5).

c) If IFF(J,1) = 3

Read set (b) first then (a).

User's Manual for Sediment II (Horizontal Model)

CARD 1

Columns	1-72	TITLE
---------	------	-------

CARD 2 (F10.5)

Columns	11-20	TETA	Crank-Nicolson weighting function (leave as 0 if steady problem).
---------	-------	------	---

CARD 3 (8I10)

Columns	1-10	NOPT	Problem option. 1 Steady state concentration problem. 2 Unsteady concentration problem. 3 Sediment problem (transient).
	21-30	NP	Number of node points.
	31-40	NE	Number of elements.
	41-50	NPX	Number of corner nodes.
	51-60	NDCOD	No initial bed profile if 0, otherwise 1.
	61-70	NTTS	Number of time steps.

71-80 NGRID Generate rectangular grid if  
equal to 1, otherwise 0.

For NGRID = 1: rectangular grid is generated.

CARD 1 (2I10,4F10.5)

Columns 11-20	NX	Number of panels in x-direction.
21-30	NY	Number of panels in y-direction.
31-40	XL	Total length in x-direction.
41-50	XY	Total length in y-direction.
51-60	XR	Grid spacing ratio (x).
61-70	YR	Grid spacing ratio (y).

CARD 2 (BF10.5)

(This card is used for test problems where uniform  
velocities, depths, and diffusion coefficients are used.)

Columns 1-10	XV	x-velocity, cm/sec.
11-20	YU	y-velocity, cm/sec.
21-30	DIFX	x-diffusion coefficient, cm <sup>2</sup> /sec.
31-40	DIFY	y-diffusion coefficient, cm <sup>2</sup> /sec.
41-50	ELS	Element source, gm/cm <sup>3</sup> /sec.
51-60	DEEP	Depth of flow, cm.
61-70	CCCC	Initial concentration, gm/cm <sup>3</sup> .

CARD 2 (I10)

Columns 1-10	NCARDS	Number of cards on which B.C. are specified next.
--------------	--------	--

CARD 3 et seq to NCARDS (I10,F10.5)

Columns 1-10	NUM	Node point number.
11-20	SPEC(NUM,1)	Specified concentration.

If NGRID = 0, the geometry and element properties are read  
in by Subroutine INPUT1.

SET 1 1 → NPX (I10,2F10.5)

Columns 1-10	J	Corner node number.
11-20	CORD(J,1)	x-coordinate of node point J.
21-30	CORD(J,2)	y-coordinate of node point J.

SET 2 1 → NE (TI5,5X,2F10.5)

Columns	1- 5	J	Element number.
	6-45	NOP(J,K)	The eight nodes (counter-clockwise) that define the element (I5).
	51-60	DIF(J,1)	x-diffusion coefficient.
	61-70	DIF(J,2)	y-diffusion coefficient.

SET 3 1 → NP (2I5,7F10.5)

Columns	1- 5	J	Node point number.
	6-10	NFIX(J)	Set = 1 if concentration boundary condition specified, otherwise 0.
	11-20	XVEL(J,1)	x-velocity.
	21-30	XVEL(J,2)	y-velocity.
	31-40	DEP(J)	Depth of flow.
	41-50	ELEV(J)	Initial bed elevations.
	51-60	SPEC(J,1)	Specified boundary condition, if any.
	61-70	CONC(J)	Initial concentration.
	71-80	R2(J)	Node point source.

The following cards for transient problems only, i.e., NTSS > 1.

CARD 1 (I10)

Columns	1-10	NCARDS	Number of cards that follow.
---------	------	--------	------------------------------

CARD 2 et seq (2(3I5,F15.5))

Columns	1- 5	J	Time step number (begin with 1).
	6-10	IFF(J,1)	Input code for each time step; 0 for first time step. 0 No input at this time step. 1 New velocity field to be read in. 2 New boundary conditions only. 3 New velocities <u>and</u> boundary conditions read.
	11-15	IFF(J,2)	Output code for each time step. 0 No output. 1 Bed profile and erosion/deposition rate.

2 Concentrations only.

3 Both.

16-30 TIM(J)

Total time (sec.) at this time  
step (repeat 1 more set on  
same card).

Subroutine INPUT is called whenever IFF(J,1)  $\neq$  0.

a) If IFF(J,1) = 1 (Velocity field only).

SET 1 (I10,3F10.5) 1  $\rightarrow$  NP

Columns 1-10 J Node point number.

11-20 XVEL(J,1) x-velocity.

21-30 XVEL(J,2) y-velocity.

31-40 DEP(J) Depth of flow.

b) If IFF(J,1) = 2 (Boundary conditions only).

CARD 1 (I10)

Columns 1-10 NCARDS Number of cards to follow.

11-20 SPEC(J,1) Specified concentration.

21-30 R2(J) Specified point source.

c) If IFF(J,1) = 3 (Both B.C. and new velocities).

Read set (b) first then set (a).

APPENDIX F: NOTATION

a	some reference elevation at which the concentration $C_a$ is known; lateral width (p. B-2)
A	area of element for horizontal model; (length of base x width) for vertical model
b	the width of base for vertical model
c'	concentration fluctuations
C	suspended sediment concentration (i.e., mass of sediment/volume of solution)
$\hat{C}$	an approximation to the concentration within an element
$C_b$	concentration of suspended sediment near the bed
$C_i$	numerical solution (p. 39)
$C_o$	initial concentration
$C_w$	mass of water/volume of suspension
$C_z$	concentration of uniform suspended particles at elevation z above the bed
$C_{ex}$	exact solution (p. 39)
d	depth of flow
$(dm/dt)_e$	mass rate of erosion per unit area
D	entire domain; physical diffusion coefficient (p. 42)
$D_m$	net mass deposited per unit width of bed
$D_{ne}$	element subdomain
$D_x, D_z, D_y$	turbulent diffusion coefficients
$e_x$	turbulent diffusion coefficient
E	a capture coefficient
$\vec{f}$	diffusive flux
G	local velocity gradient
h	the measured height of the deposit surface above the rigid bottom; the step size or spacing (p. 38); linear heat transfer coefficient for the surface (p. 37)
$h_\infty$	the final consolidated height
H	frequency of collision due to differential settling velocities of different size particles; represents the weight coefficients (p. A-7)
I	frequency of collision, on one particle by others

J	frequency of collision on a suspended spherical particle
k	Boltzmann's constant; von Karman's constant
K	coefficient involving the derivatives of the dependent variable; empirical constant (p. 13)
[K]	steady state system coefficient matrix
$K_x$	a dispersion coefficient
$K_2$	empirical constant
$K_3$	constant describing aggregate properties
$\ell$	boundary of element
L	differential operator
m	empirical exponent; the order of convergence (p. 38)
M	erodibility constant; molecular diffusivity (p. 21); quadratic shape functions (p. A-7); dry mass (p. 33)
n	number concentration of suspended particles
$n_i$	number concentration of particles of type i
$n_x, n_z$	the components of the outward normal to the element subdomain $D_{ne}$
N	two-dimensional shape functions (p. A-8)
$N_i$	shape functions
$N_k$	shape function (p. A-1)
$N/m^2$	shear strength (p. 54)
NE	number of elements
NL	number of internal and external boundaries $\ell_i$
$N_{Pe}$	the Peclet number (ratio of convective transport to diffusive transport)
$N_1$	maximum node number
$N_2$	maximum number of elements
P	probability of particles sticking to the bed; fluid pressure (p. B-2)
$\hat{q}$	approximate fluxes
$q_i$	represents the node point values of the flux for the three nodes that are on the side of the element being integrated
$q^S$	the flux source term
$q_i^S$	flux from source on the boundary i
$q_i^+$	outward normal flux from one element

$\bar{q}_i$	flux from adjacent element
$Q$	equals $(\partial c/\partial t) - \alpha_2$
$Q_I$	the observed inflow to the test reach, cfs
$Q_O$	the observed outflow from the test reach, cfs
$R$	a correction factor to be applied to the observed velocities at stations 109 + 667 and 125 + 500 to achieve an exact system water balance. If all the observations are consistent, $R = 1.0$ ; over-relaxation factor (p. C-3)
$R_{ij}$	collision radius
$s$	local contour coordinate
$S$	source/sink term to account for addition or removal of sediment
SAR	sodium adsorption ratio
$t$	the time of consolidation at which $h$ is measured; elapsed time (p. 20)
$t'$	a characteristic time
$T$	absolute temperature; thickness of deposit (p. 33)
$[T]$	consistent mass matrix; coefficient array
$u'$	temporal velocity fluctuations
$u, v, w$	components of the fluid velocity
$u, w$	velocity components in X and Z directions
$U_*$	shear velocity
$V$	relative velocity between particles (p. 9); volume of suspension in the element (p. 32)
$V_p$	settling velocity of individual aggregates in a dilute suspension
$V_s$	settling velocity of sediment
$\vec{V}_1$	velocity of water
$\vec{V}_2$	velocity of sediment
$w$	weighting coefficient (p. C-1)
$\oint$	contour integral over the boundary $\ell$ (p. 30)
$\beta_n$	positive roots of $\beta \cot \beta + hL = 0$
$\Delta m$	mass eroded per unit bed area
$\Delta S$	source term
$\Delta t$	time interval; a characteristic time in which erosion occurs

$\Delta v/\Delta t$	the observed rate of volume change in the reach, cfs
$\epsilon$	an estimate of the maximum absolute truncation error
$\epsilon_{xx}, \epsilon_{xz}, \epsilon_{zx}, \epsilon_{zz}$	turbulent exchange coefficients
$\zeta$	exponent = $V_s/kU_*$
$\eta$	$Dx/ux$ (p. 37)
$\theta$	implicitness factor ( $\theta = 1$ , fully implicit)
$\mu$	viscosity of the water
$\xi$	variable length along the boundary; boundary contour
$\rho$	fluid density
$\rho_s$	density of clay particle
$\rho_w$	density of water
$\rho_B$	bulk density of layer
$\tau_b$	bed shear stress
$\tau_b^n$	the bed shear at time step n, etc.
$\tau_{cd}$	critical shear stress for deposition
$\tau_{ce}$	critical shear stress for erosion
$\phi$	volume concentration of suspended aggregates (p. 13)

In accordance with letter from DAEN-RDC, DAEN-ASI dated 22 July 1977, Subject: Facsimile Catalog Cards for Laboratory Technical Publications, a facsimile catalog card in Library of Congress MARC format is reproduced below.

Ariathurai, Ranjan

Mathematical model of estuarial sediment transport / by Ranjan Ariathurai, Robert C. MacArthur, Ray B. Krone, Department of Civil Engineering, University of California, Davis, Davis, California. Vicksburg, Miss. : U. S. Waterways Experiment Station ; Springfield, Va. : available from National Technical Information Service, 1977.

ix, 70, 79 p. : ill. ; 27 cm. (Technical report - U. S. Army Engineer Waterways Experiment Station ; D-77-12)

Prepared for Office, Chief of Engineers, U. S. Army, Washington, D. C., under Contract No. DACW39-75-C-0080 (DMRP Work Unit No. 1B05)

References: p. 68-70.

1. Deposition. 2. Erosion. 3. Estuaries. 4. Finite element method. 5. Mathematical models. 6. Savannah Estuary.

(Continued on next card)

Ariathurai, Ranjan

Mathematical model of estuarial sediment transport ...  
1977. (Card 2)

7. Sediment transport. 8. Sedimentation. 9. Suspended load. I. Krone, Ray Beyers, joint author. II. MacArthur, Robert C., joint author. III. California. University, Davis. Dept. of Civil Engineering. IV. United States. Army. Corps of Engineers. V. Series: United States. Waterways Experiment Station, Vicksburg, Miss. Technical report ; D-77-12.

TA7.W34 no.D-77-12